The Astrophysical Journal Supplement Series, 243:22 (41pp), 2019 August https://doi.org/10.3847/1538-4365/ab23f2

The CANDELS/SHARDS Multiwavelength Catalog in GOODS-N: Photometry, Photometric Redshifts, Stellar Masses, Emission-line Fluxes, and Star Formation Rates

Guillermo Barro[1,2], Pablo G. Pérez-González[3,4], Antonio Cava[5], Gabriel Brammer[6], Viraj Pandya[7], Carmen Eliche Moral[8], Pilar Esquej[9], Helena Domínguez-Sánchez[10], Belen Alcalde Pampliega[4], Yicheng Guo[11], Anton M. Koekemoer[6], Jonathan R. Trump[12], Matthew L. N. Ashby[13], Nicolas Cardiel[4], Marco Castellano[14], Christopher J. Conselice[15], Mark E. Dickinson[16], Timothy Dolch[17], Jennifer L. Donley[18], Néstor Espino Briones[4], Sandra M. Faber[7], Giovanni G. Fazio[13], Henry Ferguson[6], Steve Finkelstein[19], Adriano Fontana[14], Audrey Galametz[20], Jonathan P. Gardner[21], Eric Gawiser[22], Mauro Giavalisco[23], Andrea Grazian[14], Norman A. Grogin[6], Nimish P. Hathi[6], Shoubaneh Hemmati[24], Antonio Hernán-Caballero[4], Dale Kocevski[25], David C. Koo[7], Dritan Kodra[26], Kyoung-Soo Lee[27], Lihwai Lin[28], Ray A. Lucas[6], Bahram Mobasher[29], Elizabeth J. McGrath[25], Kirpal Nandra[20], Hooshang Nayyeri[30], Jeffrey A. Newman[26], Janine Pforr[31], Michael Peth[6], Marc Rafelski[6], Lucia Rodríguez-Munoz[32], Mara Salvato[20], Mauro Stefanon[33], Arjen van der Wel[34], Steven P. Willner[13], Tommy Wiklind[35], and Stijn Wuyts[36]

[1] University of the Pacific, Stockton, CA 90340, USA
[2] Department of Astronomy, University of California at Berkeley, Berkeley, CA 94720-3411, USA
[3] Centro de Astrobiología (CAB, CSIC-INTA), Carretera deAjalvir km 4, E-28850 Torrejón de Ardoz, Madrid, Spain
[4] Universidad Complutense de Madrid, F. CC. Físicas, E-28040 Madrid, Spain
[5] Department of Astronomy, University of Geneva, 51 Ch. des Maillettes, 1290, Versoix, Switzerland
[6] Space Telescope Science Institute, 3700 San Martin Drive, Baltimore, MD 21218, USA
[7] UCO/Lick Observatory, Department of Astronomy and Astrophysics, University of California, Santa Cruz, CA 95064, USA
[8] Instituto de Astrofísica de Canarias, E-38200 La Laguna, Tenerife, Spain
[9] European Space Astronomy Centre, Villanueva de la Canada E-28692 Madrid, Spain
[10] Department of Physics and Astronomy, University of Pennsylvania, Philadelphia, PA 19104, USA
[11] Department of Physics and Astronomy, University of Missouri, Columbia, MO 65211, USA
[12] Department of Physics, University of Connecticut, 2152 Hillside Road, U-3046 Storrs, CT 06269, USA
[13] Center for Astrophysics, Harvard & Smithsonian, 60 Garden Street, MS-66, Cambridge, MA 02138-1516, USA
[14] INAF—Osservatorio Astronomico di Roma, via Frascati 33, I-00040 Monte Porzio Catone (RM), Italy
[15] School of Physics and Astronomy, University of Nottingham, Nottingham, UK
[16] National Optical Astronomy Observatories, 950 North Cherry Avenue, Tucson, AZ 85719, USA
[17] Department of Physics, Hillsdale College, 33 E. College Street, Hillsdale, MI 49242, USA
[18] Los Alamos National Laboratory, Los Alamos, NM 87544, USA
[19] Department of Astronomy, The University of Texas at Austin, Austin, TX 78712, USA
[20] Max-Planck-Institut für extraterrestrische Physik, Postfach 1312, Giessenbachstr., D-85741 Garching, Germany
[21] NASA Goddard Space Flight Center, Greenbelt, MD 20771, USA
[22] Department of Physics and Astronomy, Rutgers, The State University of New Jersey, 136 Frelinghuysen Road, Piscataway, NJ 08854, USA
[23] Department of Astronomy, University of Massachusetts, 710 North Pleasant Street, Amherst, MA 01003, USA
[24] California Institute of Technology, MS 100-22, Pasadena, CA 91125, USA
[25] Department of Physics and Astronomy, Colby College, Waterville, ME 04901, USA
[26] Department of Physics and Astronomy and PITT PACC, University of Pittsburgh, Pittsburgh, PA 15260, USA
[27] Department of Physics, Purdue University, 525 Northwestern Avenue, West Lafayette, USA
[28] Institute of Astronomy & Astrophysics, Academia Sinica, Taipei 10617, Taiwan
[29] Department of Physics and Astronomy, University of California, Riverside, CA, USA
[30] Department of Physics and Astronomy, University of California, Irvine, CA 92697, USA
[31] European Space Research and Technology Centre, Keplerlaan 1, 2201 AZ Noordwijk, Netherlands
[32] Dipartimento di Fisica e Astronomia, Universita degli Studi di Padova, Vicolo dell Osservatorio 3, Italy
[33] Leiden Observatory, Leiden University, NL-2300 RA Leiden, Netherlands
[34] Max-Planck-Institut für Astronomie, Königstuhl 17, D-69117 Heidelberg, Germany
[35] Catholic University of America, Department of Physics, 620 Michigan Avenue NE, Washington, DC 20064, USA
[36] Department of Physics, University of Bath, Claverton Down, Bath, BA2 7AY, UK
Received 2018 October 19; revised 2019 April 30; accepted 2019 May 16; published 2019 July 25

Abstract

We present a WFC3 F160W (*H*-band) selected catalog in the CANDELS/GOODS-N field containing photometry from the ultraviolet (UV) to the far-infrared (IR), photometric redshifts, and stellar parameters derived from the analysis of the multiwavelength data. The catalog contains 35,445 sources over the 171 arcmin^2 of the CANDELS F160W mosaic. The 5σ detection limits (within an aperture of radius 0.″17) of the mosaic range between $H = 27.8$, 28.2, and 28.7 in the wide, intermediate, and deep regions, which span approximately 50%, 15%, and 35% of the total area. The multiwavelength photometry includes broadband data from the UV (*U* band from KPNO and LBC), optical (*HST*/ACS F435W, F606W, F775W, F814W, and F850LP), near-to-mid IR (*HST*/WFC3 F105W, F125W, F140W, and F160W; Subaru/MOIRCS *Ks*; CFHT/Megacam K; and *Spitzer*/IRAC 3.6, 4.5, 5.8, and 8.0 μm), and far-IR (*Spitzer*/MIPS 24 μm, *HERSCHEL*/PACS 100 and 160 μm, SPIRE 250, 350 and 500 μm) observations. In addition, the catalog also includes optical medium-band data ($R \sim 50$) in 25 consecutive bands, $\lambda = 500$–950 nm, from the SHARDS survey and WFC3 IR spectroscopic observations with the G102 and G141 grisms ($R \sim 210$ and 130). The use of higher spectral resolution data to estimate photometric redshifts provides very high, and nearly uniform, precision from $z = 0$–2.5. The comparison to 1485 good-quality spectroscopic redshifts up to

$z \sim 3$ yields $\Delta z/(1 + z_{spec}) = 0.0032$ and an outlier fraction of $\eta = 4.3\%$. In addition to the multiband photometry, we release value-added catalogs with emission-line fluxes, stellar masses, dust attenuations, UV- and IR-based star formation rates, and rest-frame colors.

Key words: galaxies: high-redshift – galaxies: photometry

1. Introduction

Large multiwavelength photometric surveys have made it possible to study galaxy populations over most of cosmic history. Near-infrared-selected samples have been used to trace the evolution of the stellar-mass function (e.g., Pérez-González et al. 2008; Marchesini et al. 2009; Muzzin et al. 2013), the star formation–mass relation (e.g., Whitaker et al. 2012), and the structural evolution of galaxies (e.g., Franx et al. 2008; Bell et al. 2012; van der Wel et al. 2012; Wuyts et al. 2012). Until recently, most of these surveys relied on deep, wide-field imaging from ground-based telescopes (e.g., Williams et al. 2009; Muzzin et al. 2013). The WFC3 camera on the *Hubble Space Telescope* (*HST*) has opened up the possibility to select and study galaxies at near-infrared wavelengths with excellent sensitivity and spatial resolution.

The Cosmic Assembly Near-infrared Deep Extragalactic Legacy Survey (CANDELS; Grogin et al. 2011; Koekemoer et al. 2011) is a 902 orbit legacy program designed to study galaxy formation and evolution over a wide redshift range using the near-infrared *HST*/WFC3 camera to obtain deep imaging of faint and distant objects. So far, CANDELS has imaged over 250,000 distant galaxies within five strategic regions: GOODS-S, GOODS-N, UDS, EGS, and COSMOS over a combined area of $\sim$0.22 deg^2. The extremely deep, high spatial resolution observations have enabled a broad array of science, such as the characterization of the UV luminosity functions up to $z = 10$ (e.g., Finkelstein et al. 2015; Bouwens et al. 2016), the stellar-mass functions and the star formation rate (SFR) sequence at $z = 4$–6 (Duncan et al. 2014; Grazian et al. 2015; Mortlock et al. 2015; Salmon et al. 2015), or detailed studies of the structural and stellar-mass growth in star-forming and quiescent galaxies since cosmic noon, $z \sim 2$ (e.g., Wuyts et al. 2013; Barro et al. 2014; van der Wel et al. 2014; Guo et al. 2015; Papovich et al. 2015).

The CANDELS multiwavelength photometric catalogs for the GOODS-S, UDS, COSMOS, and EGS fields have been presented in Guo et al. (2013), Galametz et al. (2013), Nayyeri et al. (2017), and Stefanon et al. (2017), respectively; photometric redshifts and stellar population parameters for the first two fields are presented separately in Dahlen et al. (2013) and Santini et al. (2015). This paper presents the multiwavelength catalog in GOODS-N, based on a CANDELS WFC3/F160W detection and making use of all the available ancillary data spanning from the UV to FIR wavelengths. Most notably, this catalog includes photometry in 25 medium bands from the SHARDS survey (Pérez-González et al. 2013), which follows an observational strategy similar to previous optical surveys, such as COMBO17 (Wolf et al. 2001, 2003) and the COSMOS medium-band survey (Ilbert et al. 2009), but provides higher spectral resolution ($R \sim 50$) and deeper photometry (4σ, $H \sim 27$ mag) with an average subarcsecond seeing.

Furthermore, we expand the high spectral resolution coverage to the NIR by combining new WFC3 G102 grism observations with the publicly released G141 data from the 3D-HST survey (Momcheva et al. 2016), which yields a nearly continuous coverage from $\lambda = 0.8$ to 1.7 μm with a resolution better than $R = 130$. Lastly, we complement the optical and NIR photometry with a compilation of all the available FIR data from *Spitzer* and *Herschel*, spanning from $\lambda = 24$ to 500 μm.

This paper is organized as follows: Section 2 briefly summarizes the photometry data sets included in our catalog. Section 3 discusses the detection process in the CANDELS F160W image and photometry measurements on the *HST* and mid-to-low spatial resolution images. Section 4 presents several tests to evaluate the quality of the multiband photometry. Section 5 presents the value-added properties estimated from the fitting of the UV-to-FIR spectral energy distributions (SEDs) to stellar population and dust emission templates. The summary is given in Section 6. The appendices describe the contents of the photometric and value-added catalogs, released together with this paper, as well as the methodology to estimate self-consistent SFRs.

The CANDELS GOODS-N multiwavelength catalog and its associated files are made publicly available on the Mikulski Archive for Space Telescopes (MAST).[37] They are also available in the Rainbow Database (Pérez-González et al. 2008; Barro et al. 2011), either through Slicer,[38] which allows a direct download of images and catalogs, or through Navigator,[39] which features a query menu that allows users to search for individual galaxies, create subsets of the complete sample based on different criteria, and inspect cutouts of the galaxies in any of the available bands.

All magnitudes in the paper are on the AB scale (Oke 1974) unless otherwise noted. We adopt a flat ΛCDM cosmology with $\Omega_m = 0.3$, $\Omega_\Lambda = 0.7$, and use the Hubble constant in terms of $h \equiv H_0/100\,\mathrm{km\,s^{-1}\,Mpc^{-1}} = 0.70$.

2. Imaging Data Sets

The GOODS-N field (Giavalisco et al. 2004), centered around the Hubble Deep Field North (HDFN; Williams et al. 1996) at α(J2000) = $12^h36^m55^s$ and δ(J2000) = $+62°14^m11^s$, is a sky region of about 171 arcmin^2, which has been targeted for some of the deepest observations ever taken by NASA's Great Observatories, *HST*, *Spitzer*, and *Chandra*, as well as by other world-class telescopes (see Figure 1).

The multiwavelength coverage of GOODS-N spans the X-ray, UV, to far-IR and radio data: UV data from the *Galaxy Evolution Explorer* (PI: C. Martin), ground-based optical data from the U to z bands taken by the Kitt Peak 4 m telescope and from Suprime-Cam on the Subaru 8.2 m as part of the Hawaii Hubble Deep Field North project (Capak et al. 2004), 25 medium bands from the GTC SHARDS (Pérez-González et al. 2013) survey, near-infrared (NIR) J, H, and Ks imaging from the Subaru MOIRCS deep survey (Kajisawa et al. 2009) and CFHT/WIRCam K photometry (Hsu et al. 2019); IRAC maps from *Spitzer* GOODS (Dickinson et al. 2003), SEDS

[37] https://archive.stsci.edu/prepds/candels/ and Faber (2011).

[38] US: http://arcoiris.ucolick.org/Rainbow_slicer_public/, and Europe: http://rainbowx.fis.ucm.es/Rainbow_slicer_public/.

[39] US: http://arcoiris.ucolick.org/Rainbow_navigator_public, and Europe: http://rainbowx.fis.ucm.es/Rainbow_navigator_public/.

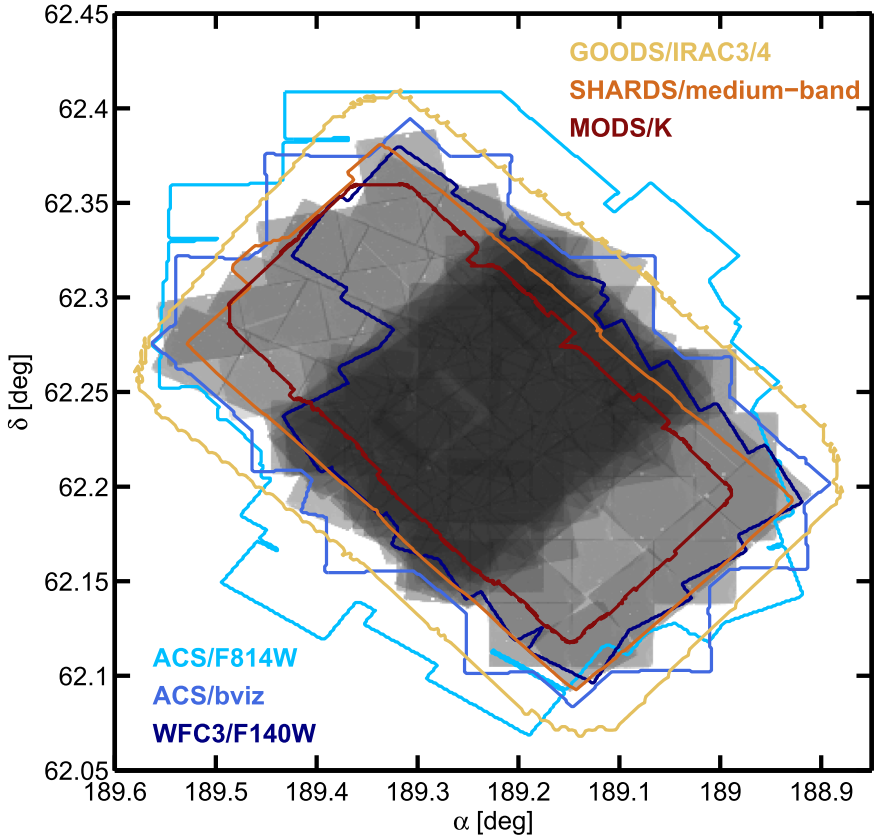

Figure 1. Sky coverage of the multiwavelength data sets used in the GOODS-N F160W catalog. The gray-scale image shows the exposure time of the F160W mosaic, which includes the CANDELS wide and deep region. The coverage of ancillary data from UV to MIR is also shown: GOODS *HST*/ACS (blue), MOIRCS/MODS *Ks* (red), GTC/SHARDS optical medium bands (orange), and GOODS *Spitzer*/IRAC (yellow). The entire field is covered by both SEDS *Spitzer*/IRAC and CFHT/K.

Table 1
Image Sources

Filters	Telescope/Instrument	Survey	References
U	KPNO 4 m/Mosaic	Hawaii HDFN	Capak et al. (2004)
U′	LBT/ LBC	⋯	Grazian et al. (2017)
25 medium-band optical	GTC/OSIRIS	SHARDS	Pérez-González et al. (2013)
F435W, F606W, F775W, F850LP	*HST*/ACS	GOODS	Giavalisco et al. (2004)
F814W	*HST*/ACS	CANDELS	Grogin et al. (2011), Koekemoer et al. (2011)
F105W, F125W, F160W	*HST*/WFC3	CANDELS	Grogin et al. (2011), Koekemoer et al. (2011)
F140W	*HST*/WFC3	AGHAST	GO: 11600 (PI: B. Weiner)
K_s	Subaru/MOIRCS	MODS	Kajisawa et al. (2011)
K	CFHT/Megacam	⋯	Hsu et al. (2019)
3.6, 4.5 μm	*Spitzer*/IRAC	SEDS, S-CANDELS	Ashby et al. (2013, 2015)
5.8, 8 μm	*Spitzer*/IRAC	GOODS	Dickinson et al. (2003)
24, 70 μm	*Spitzer*/MIPS	GOODS/FIDEL	Dickinson et al. (2003)
100, 160 μm	*Herschel*/PACS	PEP	Berta et al. (2011), Lutz et al. (2011)
250, 350, 500 μm	*Herschel*/SPIRE	GOODS/*Herschel*, HerMES	Oliver et al. (2012), Magnelli et al. (2013)

(Ashby et al. 2013), and S-CANDELS (Ashby et al. 2015); MIPS data from GOODS-FIDEL (PI: M. Dickinson); and *Herschel* data from the GOODS-*Herschel* (Elbaz et al. 2011) and PEP (Magnelli et al. 2013) surveys.

In the following, we provide more details about the data sets included in the multiband catalog. The telescope/instrument as well as the reference for the survey is given in Table 1. Table 2 lists the central wavelength of the filters, dust attenuation from Galactic extinction, image zero point, and the average FWHM for each of the mosaics. Transmission curves for all filters are plotted in Figure 2.

2.1. HST

2.1.1. ACS Optical Imaging

The *HST*/ACS F435W, F606W, F775W, and F850LP images used in our catalog are version v3.0 of the mosaicked images from the GOODS *HST*/ACS Treasury Program. They consist of data acquired prior to the *HST* Servicing Mission 4, including mainly data of the original GOODS *HST*/ACS program in *HST* Cycle 11 (GO 9425 and 9583; see Giavalisco et al. 2004) and additional data acquired in *HST*/ACS F606W and F814W as part of the CANDELS survey and during the

Table 2
GOODS-N Optical-to-NIR Imaging

Band	$\lambda_{central}$ (μm)	A_λ (mag)	Zero Point (AB)	FWHM (arcsec)	ZP-corr (flux)	5σ Depth[a] (mag)
U	0.35929	0.052	31.369	1.26	0.88	26.7
U′	0.36332	0.052	26.321	1.10	1.07	28.2
F435W	0.43179	0.044	25.689	0.10	1.03	27.1
SHARDS[b]	0.50–0.94	…	…	…	…	…
F606W	0.59194	0.030	26.511	0.10	0.97	27.7
F775W	0.76933	0.020	25.671	0.11	0.98	27.2
F814W	0.76933	0.020	25.671	0.11	0.97	28.1
F850LP	0.90364	0.015	24.871	0.11	1.02	26.9
F105W	1.24710	0.009	26.230	0.18	1.03	26.4
F125W	1.24710	0.009	26.230	0.18	1.01	27.5
F140W	1.39240	0.007	26.452	0.18	1.04	26.9
F160W	1.53960	0.006	25.946	0.19	1.03	27.3
K	2.13470	0.004	26.000	0.60	0.92	24.4
Ks	2.15770	0.004	26.000	0.60	0.96	24.7
IRAC1	3.55690	0.000	21.581	1.7	0.93	24.5
IRAC2	4.50200	0.000	21.581	1.7	0.90	24.6
IRAC3	5.74500	0.000	20.603	1.9	0.87	22.8
IRAC4	7.91580	0.000	21.781	2.0	0.80	22.7

Notes.
[a] Based on aperture photometry with radius equal to the FWHM of the PSF in each band.
[b] 25 medium bands; see Table 6 in Appendix A and Pérez-González et al. (2013) for more details.

search for high-redshift Type Ia supernovae carried out during Cycles 12 and 13 (program ID 9727, P.I. Saul Perlmutter, and 9728, 10339, 10340, P.I. Adam Riess; see, e.g., Riess et al. 2007).

2.1.2. WFC3 IR Imaging

The CANDELS survey observed the GOODS-N field in three *HST*/WFC3 IR filters F105W, F125W, and F160W following a "wedding-cake" observing strategy similar to that in the CANDELS/GOODS-S field but with only two layers, deep and wide (i.e., there is no ultra-deep region). The deep region consists of a rectangular grid of 3 × 5 pointings that covers the central one-third of the mosaic (see Figure 1) with an approximate area of ∼55 arcmin^2 (∼35% of the mosaic). The observations were done over 10 epochs at 6–8 orbit depth in F125W and F160W. The wide region covers the northern and southern two-thirds of the field (∼50% of the mosaic) with 2 × 4 pointings in both filters and has approximately two-orbit exposures. The distributions of the exposure time and limiting magnitude of the F160W mosaic are shown in Figure 3. An intermediate-depth region (between ∼4 and 9 ks) is defined by the overlapping area between the wide and deep regions. The CANDELS F105W observations consist only of the deep and wide regions with an exposure gap in the intermediate region. See Grogin et al. (2011) and Koekemoer et al. (2011) for more details of CANDELS *HST*/WFC3 observations and data reduction. We also include in our catalog the two-orbit-depth F140W images taken as part of the G141 AGHAST survey GO: 11600 (PI: B. Weiner; see next section) and GO:12461 COLFAX (PI: Riess).

The WFC3 mosaics used in this paper have been reduced following the same data reduction strategy described in the previous CANDELS data release papers for the other fields. The images in all bands are drizzled to 0.″06 pixel^{-1} to match the default CANDELS pixel scale (see Koekemoer et al. 2011 for details).

2.1.3. WFC3 G102 and G141 Grism Spectroscopy

The GOODS-N field was observed in the *HST*/G141 grism at a two-orbit-depth as part of the AGHAST program (GO:11600; PI: Weiner). The 28 pointings of the program were reduced, analyzed, and incorporated into the 3D-HST survey (Brammer et al. 2012; Momcheva et al. 2016), which uses a similar observing strategy over the other four CANDELS fields. Each pointing was observed for two orbits, with ∼800 s of direct imaging in the F140W filter and 4511–5111 s with the G141 grism per orbit. The observations were arranged in a 4 × 6 grid. There is no imaging or grism spectra in the northwestern edge of the field (dark blue line in Figure 1). In this paper, we make use of the 3D-HST spectra released in their v4.1.5 data products described in Momcheva et al. (2016).

Furthermore, we present complementary *HST*/G102 observations (GO:13179; PI: Barro) that were designed to follow the same tiling strategy of the AGHAST program in order to maximize the number of galaxies with simultaneous grism coverage. The observations consist of 28 two-orbit-depth pointings with 400 s of direct imaging in the F105W filter and ∼5000 s with the G102 grism per orbit following the same four-point dither pattern of the 3D-HST survey. The observations were processed using the 3D-HST data reduction pipeline described in Momcheva et al. (2016). The pipeline combines the individual G102 exposures into mosaics using AstroDrizzle (Gonzaga 2012). These individual exposures are aligned using `tweakreg` and grism sky backgrounds are subtracted using master sky images as described by Brammer et al. (2015). Each exposure is then interlaced to a final image with a pixel size of ∼0.″06. Before sky subtraction and interlacing, each individual exposure was checked and corrected for elevated backgrounds,

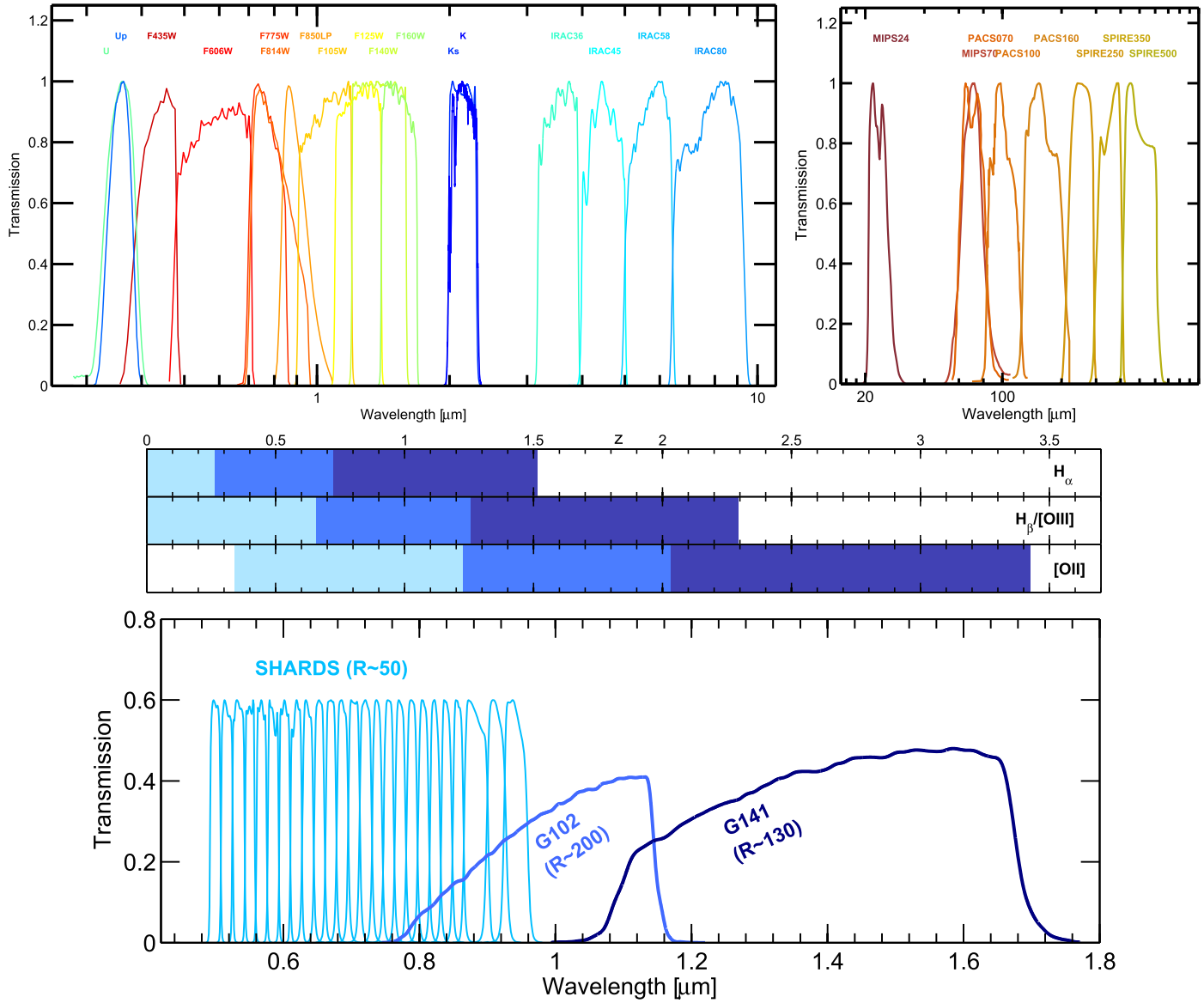

Figure 2. Top: transmission curves of all the broadband filters used in the CANDELS GOODS-N multiwavelength catalog, from the UV, optical, and NIR (left) to the FIR (right). Bottom: transmission curves of the higher spectral resolution data—the optical medium-band survey SHARDS ($R \sim 50$) and the two *HST*/WFC3 grisms, G102 ($R \sim 200$) and G141 ($R \sim 130$). The panel above shows the redshift ranges in which the most prominent emission lines (Hα, [O III], Hβ, and [O II]) can be detected in each of these higher resolution data set.

due to the He Earth glow using the script[40] described by Brammer et al. (2014).

From the final G102 mosaics, the spectra of each individual object are extracted by predicting the position and extent of each two-dimensional spectrum based on the `SExtractor` (Bertin & Arnouts 1996) segmentation of the CANDELS F160W image. As this is done for every single object, the contamination, i.e., the dispersed light from neighboring objects in the direct image field of view (FOV) is estimated and accounted for. We also carried out visual inspections of the individual 2D and 1D extractions for a magnitude-limited subset of the data (F105W < 23 mag) in order to flag catastrophic failures. The automated redshift determination and the emission-line measurements based on the G102 and G141 data sets are presented in Section 5.2.

2.2. Ground-based Imaging

2.2.1. Ultraviolet

The *U*-band image was taken with the Mosaic camera on the Kitt Peak 4 m telescope by the Hawaii Hubble Deep Field North project (Capak et al. 2004).[41]

In addition to the Kitt Peak imaging, an LBT Strategic Program (PI: A. Grazian) was approved on 2012B, with the aim of obtaining ultra-deep imaging in the *U* band of the CANDELS/GOODS-N field using the LBC instrument at the prime focus of the LBT telescope (Giallongo et al. 2008; Rothberg et al. 2016). The program consisted of approximately 25 hr on a single pointing of the LBC camera. The LBC FOV is larger than the whole CANDELS/GOODS-N field, and it covers approximately 600 arcmin^2 with homogeneous coverage/depth.

[40] https://github.com/gbrammer/wfc3/blob/master/reprocess_wfc3.py

[41] http://www.astro.caltech.edu/~capak/hdf/index.html

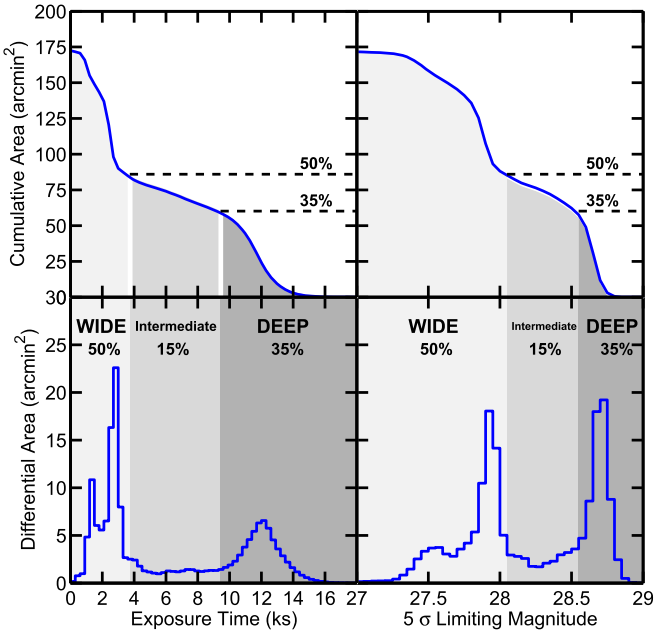

Figure 3. Distributions of the exposure time and limiting magnitude of the F160W mosaic used as the detection image of our catalog. The left column shows the cumulative (upper panel) and differential (lower) distributions of the exposure time, while the right column shows the same distributions of the 5σ limiting magnitude of the image.

The same area has also been observed by other LBT partners (AZ, OSURC, and LBTO), for a total exposure time of 33 hr in the U band (seeing $1\farcs1$). The detailed description of these data is provided in a dedicated paper (Grazian et al. 2017) summarizing all of the LBC deep observations available in the CANDELS fields. The relatively long exposure time and the good seeing allowed a magnitude limit in the U band of 30.2 AB at signal-to-noise ratio $(S/N) = 1$ to be reached, resulting in one of the deepest UV images ever obtained.

2.2.2. SHARDS Optical Medium-band Survey

The Survey for High-z Absorption Red and Dead Sources (SHARDS; Pérez-González et al. 2013), an ESO/GTC Large Program, targeted the GOODS-N field with GTC/OSIRIS in 2012–2015 and obtained 220 hr of ultra-deep imaging data through 25 medium-band optical filters. The wavelengths covered a range from 500 to 950 nm with a spectral resolution of $R \sim 50$. The depth is 26.5 mag at the 4σ level (at least), and the seeing was always below $1''$ for every single filter. SHARDS used two OSIRIS (FOV $7\farcm8 \times 7\farcm8$) pointings to cover most of the CANDELS region (110 arcmin^2). The SHARDS optical imaging data has a particular characteristic that has to be taken into account to obtain accurate SEDs: the passband of the filter seen by different parts of the detector changes, getting bluer as we move away from the optical axis, which is located about $1'$ to the left of the FOV. Therefore, every galaxy detected by SHARDS counts with a unique set of SHARDS passbands, which are defined by their transmission curves (whose shapes do not change and, therefore, are the same for all galaxies) and their central wavelengths (which change and must be provided for each galaxy). We remark that this is an optical effect that affects all filters, so the final SED for each galaxy counts with the same spectral resolution, $R \sim 50$, but all filters are offset from the nominal central wavelength. In order to properly account for this effect, the SHARDS photometry of the F160W sources (see Section 3.2) is provided in a separate catalog (see Table 5) which includes the central wavelength for each galaxy and filter. Furthermore, the SHARDS science images in each of the 25 filters, which are released with this paper, are provided jointly with a map of the central wavelength for each pixel that can be used to account for the wavelength shift (see Pérez-González et al. 2013 for more details).

2.2.3. Near Infrared

Deep K_s-band images of the field were taken using the Multi-Object Infrared Camera and Spectrograph (MOIRCS) on Subaru as part of the MOIRCS Deep Survey (MODS; Kajisawa et al. 2011).[42] The data reach a 5σ total limiting magnitude for point sources of $K_s = 24.2$ over a 103 arcmin^2 mosaic consisting of four MOIRCS pointings. The central $\sim$28 arcmin^2 of the mosaic contains a deeper region where the data reach $K_s = 25.1$. In this work, we make use of the publicly available "convolved" mosaic in which each of the four pointings have been homogenized to match the field with the worst seeing (FWHM $\sim 0\farcs6$).

In addition to the MOIRCS data, we also make use of a deep broadband K_s mosaic based on observations with the CFHT WIRCam instrument (Hsu et al. 2019). The final mosaic used in this paper covers $\sim$0.4 deg^2 around the GOODS-N field. It has a 50% completeness limit for point sources between $K_s = 24.6$–24.8 mag. The astrometry was calibrated using the Two Micron All Sky Survey (2MASS) catalog (Skrutskie et al. 2006) with a final internal accuracy of $\sim 0\farcs1$.

2.3. Spitzer/Herschel *Mid- to Far-IR*

2.3.1. IRAC S-CANDELS

GOODS-N was observed by *Spitzer*/IRAC (Fazio et al. 2004) during the cryogenic mission in four bands (3.6, 4.5, 5.8, and 8.0 μm) for two epochs with a separation of six months (2004 February and 2004 August) by the GOODS Spitzer Legacy project (PI: M. Dickinson). Each epoch contained two pointings, each with a total extent of approximately $10'$ on a side. The exposure time per band per sky pointing was approximately 25 hr per epoch and doubled in the overlap region. We use the 5.8 and 8.0 μm imaging from this program in our catalog.

The 3.6 and 4.5 μm photometry was measured on the mosaics from the *Spitzer*-CANDELS (S-CANDELS, PID 80216; Ashby et al. 2015) survey, which combines the original cryogenic data with those taken from the warm mission phase. The resultant 3.6 and 4.5 μm mosaics fully cover the WFC3 F160W area of the CANDELS survey to a depth of at least 50 hr. The IRAC data in all four bands were reprocessed and mosaicked using the same CANDELS *HST* tangent-plane projection and with a pixel scale of $0\farcs06$ pixel^{-1} to prepare them appropriately for further photometric analysis (see also Ashby et al. 2015).

2.3.2. MIPS GTO, PEP, and GOODS-Herschel

The GOODS-N field has been observed in the mid-IR wavelengths with *Spitzer*/MIPS at 24 and 70 μm as part of the

[42] http://www.astr.tohoku.ac.jp/MODS

GTO and GOODS surveys (Dickinson et al. 2003; see also Frayer et al. 2006). Here we use the photometric catalogs in both bands described in Pérez-González et al. (2005, 2008), which are based on the reduced and mosaicked data. Furthermore, far-IR observations with the Photodetector Array Camera and Spectrometer (PACS; Poglitsch et al. 2010) and the Spectral and Photometric Imaging REceiver (SPIRE; Griffin et al. 2010), on board the *Herschel* Space Observatory, were obtained as part of the PACS Evolutionary Probe (PEP; Berta et al. 2011; Lutz et al. 2011), GOODS-*Herschel* (Magnelli et al. 2013), and HerMES (Oliver et al. 2012) surveys. The 5σ detection limits of the far-IR data are provided in Table 13. The mid-to-far-IR photometry probes the rest-frame wavelengths close to the peak of the dust IR emission of galaxies up to redshifts of $z \sim 3$. Therefore, it provides a very useful SFR indicator, complementary to the UV luminosity, for a large number of galaxies. See Section 3.3 and Appendix D for a more detailed description of the IR data and the photometric measurements.

2.4. Value-added Data

2.4.1. Spectroscopic Redshifts

A number of different spectroscopic observations were conducted in the GOODS-N field over the course of the last 20 yr. Here we include redshift compilations based primarily on large spectroscopic surveys using the *Keck*/DEIMOS optical spectrograph: the ACS-GOODS redshift survey (Cowie et al. 2004; Barger et al. 2008), the Team Keck Redshift Survey Wirth et al. TKRS 2004), and the DEEP3 galaxy redshift survey (Cooper et al. 2011). We also included redshifts from a number of other smaller surveys that often targeted specific types of objects or small regions defined by observations with new instruments: Lyman-Break galaxies (Reddy et al. 2006), bright-IR galaxies (Pope et al. 2008), submillimeter galaxies (Chapman et al. 2005), or the ACS-grism PEARS survey (Ferreras et al. 2009). Furthermore, we complemented these optical redshifts with results from recent NIR spectroscopic campaigns using the *Keck*/MOSFIRE spectrograph that are critical to increase the number of secure spectroscopic redshifts beyond $z \sim 1.5$: the first epoch of the MOSFIRE Deep Evolution Field (MOSDEF) survey (Kriek et al. 2015) and the TKRS2 (Wirth et al. 2015). The extensive spectroscopic campaigns in GOODS-N yield a total of ∼5000 unique redshifts within the CANDELS F160W mosaic coverage, and ∼3000 of those have a highly reliable quality flag. The counterparts to the spectroscopic sources were identified using a cross-match radius of $0\farcs8$ (if more than one object falls within the matching radius, the closest match with the highest confidence flag was adopted). All spectroscopic identifications are listed in the catalogs, but only those with reliable quality flags are used in the analysis of galaxy properties.

2.4.2. X-Ray

We used X-ray data from the *Chandra* 2 Ms source catalog by Alexander et al. (2003), covering the entire surveyed region of the F160W mosaic in GOODS-N, to select candidates that harbor an active galactic nucleus (AGN) within our sample. The most likely X-ray counterparts to the CANDELS sources were identified using a cross-matching radius of $2\farcs5$ between the CANDELS F160W catalog and the X-ray catalog of Alexander et al. (2003). We identify a total of 316 X-ray sources with a reliable F160W counterpart. This finds ∼3% of all the sources in the F160W catalog down to $H < 24.5$.

Table 3
SExtractor Parameters in Cold and Hot Modes

	Cold Mode	Hot Mode
DETECT_MINAREA	5.0	10.0
DETECT_THRESH	0.75	0.7
ANALYSIS_THRESH	5.0	0.8
FILTER_NAME	tophat_9.0	Gauss_4.0
DEBLEND_NTHRESH	16	64
DEBLEND_MINCONT	0.0001	0.001
BACK_SIZE	256	128
BACK_FILTERSIZE	9	5
BACKPHOTO_THICK	100	48
MEMORY_OBJSTACK	4000	4000
MEMORY_PIXSTACK	400000	400000
MEMORY_BUFSIZE	5000	5000

3. Photometry

This section discusses the methods used to assemble the UV-to-FIR multiwavelength photometric catalog. The following subsections describe the procedures to identify and characterize all of the sources detected in the WFC3/F160W image and to obtain self-consistent photometric measurements in the high-, intermediate-, and low-resolution photometric data sets.

3.1. High-resolution HST Data

3.1.1. WFC3 F160W Detection and Photometry

We follow an approach similar to that in the four previous CANDELS data papers (Galametz et al. 2013; Guo et al. 2013; Nayyeri et al. 2017; Stefanon et al. 2017). We identify sources using the reddest NIR band, WFC3/F160W, mosaic. Both source detection and photometry were performed using a slightly modified version of `SExtractor` v2.8.6 (Bertin & Arnouts 1996) that fixes some known issues that often cause the inclusion of false detections in the final catalog merged with real sources and a sky oversubtraction that could affect faint extended sources (see Galametz et al. 2013).

The source detection is based on the two-step "cold" plus "hot" strategy described in more detail in the CANDELS UDS (Galametz et al. 2013) and GOODS-S (Guo et al. 2013) papers. Briefly, we ran `SExtractor` twice using two different parameter configurations (see Table 3) aimed at detecting bright/large sources without over-deblending them (cold mode) or pushing the detection limit to recover faint sources close to the limiting depth of the mosaic (hot mode). Then, we merge the cold and hot catalogs following a similar approach to the `GALAPAGOS` code (see Barden et al. 2012 for more details). All cold-mode-detected sources are included in the merged catalog, but only those hot-mode sources whose segmentation map does not overlap with the photometric (Kron 1980) ellipse of a cold-mode source are included, i.e., hot-mode sources that are clearly overlapping with a cold-mode detection or the result of excessive shredding are excluded from the merged catalog. We detect 35,445 sources in the F160W mosaic. Among them, 27,293 sources are detected by the cold mode and 8152 sources by the hot mode.

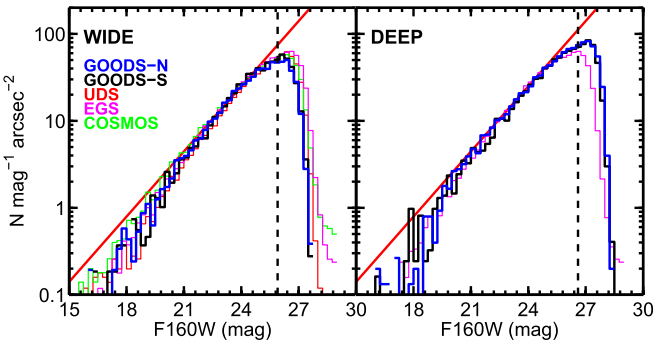

Figure 4. Differential number counts for objects detected in the GOODS-N F160W catalog on the wide (left) and deep (right) regions. The different histograms show the number counts in all five CANDELS fields for comparison. The UDS, COSMOS, and EGS fields were only observed to "wide" depth. The solid red line in each panel shows the best power-law fit to the number counts in the magnitude range where the sample is complete.

Figure 4 shows the distribution of detected sources in the F160W mosaic as a function of magnitude (i.e., the differential number counts). The left panel depicts the number counts in the GOODS-N wide region compared to those measured in regions of similar depth in the other four CANDELS fields. All of the measurements are in good agreement up to $H \sim 24$ mag. As pointed out in Stefanon et al. (2017), the number counts in the wide region of the GOODSs and COSMOS fields are slightly below those in the UDS and EGS measurements in the $24 < H < 26.5$ range, most likely due to the slightly deeper data (0.2 mag) in EGS compared to those fields. The right panel of Figure 4 compares the number counts in the deep regions of GOODS-N and GOODS-S, which are consistent up to $H \sim 29$ mag.

As expected, the bulk of the number counts are consistent with those in the wide region (the counts in EGS are shown again as reference), while the number of detections at fainter magnitudes $H \gtrsim 26$ increases. The differential variation of the number counts in the faint end can be used to assess the completeness of the catalog. Following the approach in Guo et al. (2013), we fit the number counts in the region were the catalog is expected to be complete ($20 < H < 24$) with a power law of slope $\gamma = 0.20 \pm 0.06$. Then, we find the ∼50% completeness limit by computing the magnitude where the relative difference between the observed counts and the power law reaches a factor of 2: $H \sim 25.9$ and 26.6 mag in the wide and deep regions, respectively (dashed lines in Figure 4). These values agree with the completeness limits of the CANDELS/GOODS-S catalog at similar depths (see also Figure 3 of Duncan et al. 2014). We refer the reader to Guo et al. (2013) for a more detailed discussion on the dependence of the completeness limit with the surface brightness profiles of the galaxies in GOODS-S. Given the similar depths of the GOODS fields, those results are directly applicable to the GOODS-N catalog.

3.1.2. Photometry Flags

At this stage, we also assigned a photometry flag to every object in the catalog. The flagging system is the same as that adopted in previous CANDELS papers and discussed in detail by Galametz et al. (2013). Briefly, the flagging scheme is based on the properties of the F160W mosaic. We use a zero for sources with reliable photometry and assigned a value of one either for bright stars or spikes associated with those stars. The radius of the star's masks range between 3″ and 5″ for ∼20 intermediate brightness stars and 10″ for the two brightest stars in the field. A photometric flag of 2 is associated with the lower exposure edges of the mosaic or defects as measured from the F160W rms maps. This is a very conservative flag assigned only to pixels with extreme (>1E5) values of the rms map.

3.1.3. Optical/NIR HST Photometry

The photometry in all other *HST* bands—ACS F435W, F606W, F775W, F814W, F850LP, and WFC3 F105W, and F125W—was measured running `SExtractor` in dual mode using the F160W mosaic as reference to ensure that the colors are measured within apertures of the same size. This means that the multiband photometry is computed only for the sources detected in the F160W mosaic. We follow the same cold+hot routine described in the previous section by running `SExtractor` twice per band. In order to take into account the variations in spatial resolution as a function of wavelength (see the typical FWHMs of the *HST* bands in Table 2), all *HST* images were previously smoothed to the lower spatial resolution of F160W (FWHM ∼ 0.″18) using the `IRAF/PSFMATCH` package with kernels that matched the multiband PSFs with that of F160W. We computed semiempirical PSFs in the WFC3 bands by combining a stack of isolated, unsaturated stars from across the mosaic with synthetic PSFs generated with TinyTim (Krist 1995). We used the central pixels from the synthetic models and the wings of stacked stars (see van der Wel et al. 2012 for more details). The ACS PSFs were based on purely empirical models computed by stacking well-detected stars, without any artifacts, in each ACS band.

The left panel of Figure 5 compares the stacked light profile of several high-S/N stars, extracted from the deep region, in all *HST* bands after running `PSFMATCH`. The central and right panels also show the curves of growth (fraction of light enclosed as a function of aperture size) in each band and the fraction of enclosed light relative to that of the F160W PSF. All profiles converge quickly to unity after a few pixels, and the relative photometric error in all *HST* bands is less than 5% for apertures larger than two pixels (0.″12), which is larger than the typical isophotal radius for the bulk of the sources (≳97%).

We computed several different photometric measurements available in the `SExtractor` configuration, namely, `FLUX_AUTO`, measured on Kron elliptical apertures; `FLUX_ISO` measured on elliptical isophotes; and `FLUX_APER` measured in a series of 11 circular apertures (see Appendix A for a description of all the measurements included in the photometric catalog). As discussed in the previous CANDELS data papers, we adopt `FLUX_AUTO` as the default "total" photometry for all sources in the F160W band, while for the other bands we determine the total flux scaling `FLUX_ISO` by the ratio `FLUX_AUTO/FLUX_ISO` in each band. This ratio is used to convert their isophotal fluxes and uncertainties into the total fluxes and uncertainties. The isophotal correction ensures that the flux is measured within the same isophotal area in all bands (defined by the F160W segmentation map) and maximizes the S/N for faint sources. This method provides an accurate estimate of colors and fluxes subject to the prior assumption that the PSF-convolved profile is the same in all bands. We verify the quality of the multiband SEDs in Section 4 by performing both internal and external checks, comparing to another catalog.

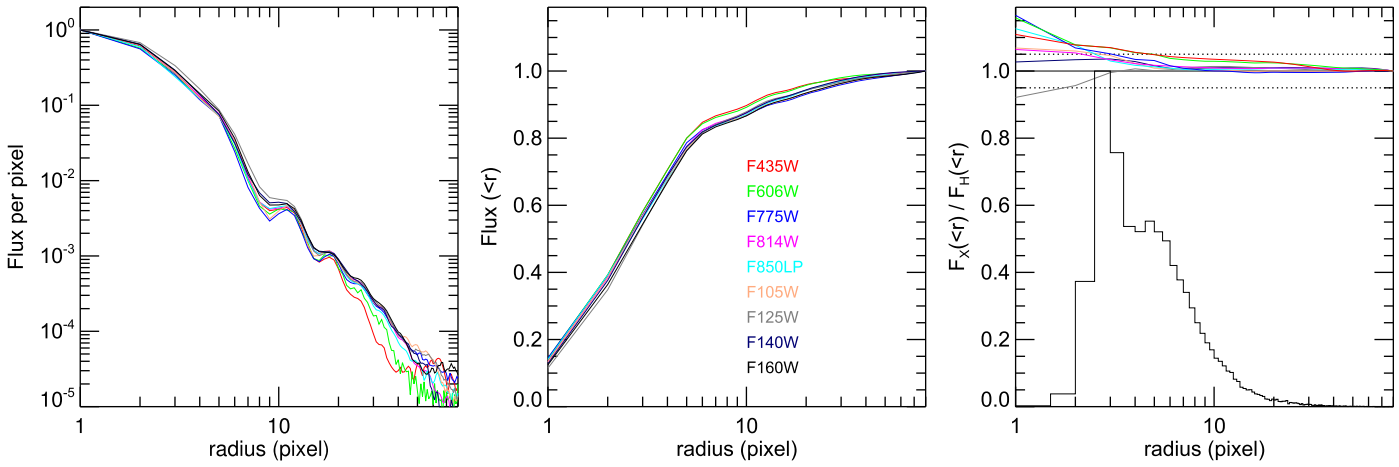

Figure 5. Accuracy of PSF matching between other *HST* bands and F160W. Left: the light profile of matched PSFs for each band. Middle: the curve of growth of each matched PSF. Right: the curve of growth of each matched PSF normalized by the curve of growth of the F160W PSF. In this panel, curves with values greater than unity are undersmoothed, and vice versa. All curves are color-coded as the labels in the middle panel show. Dotted lines in the right panel show the 5% relative error. The solid histogram in the right panel shows the distribution of the isophotal radii of all objects in our catalog.

3.2. Intermediate-resolution Ground- and Space-based Data: TFIT

We computed multiwavelength photometry in all the ancillary ground-based data and in the *Spitzer*/IRAC bands using the TFIT code (Laidler et al. 2007) and following the same methodology described in the previous CANDELS data papers. TFIT is a template-fitting software conceived to overcome the issues related with obtaining consistent photometry across large data sets that exhibit significant differences in spatial resolution. The code uses accurate positional information of the sources in the highest resolution band (in this case *HST*/F160W) to create PSF-matched models ("templates") of the sources in the intermediate-resolution bands (e.g., ground-based *K* band or IRAC). These "templates" are computed on an object-by-object basis by smoothing the high-resolution cutouts to low resolution using a convolution kernel (see, e.g., Galametz et al. 2013). Then, the code fits iteratively for the photometry by comparing the real to the modeled images in those bands. With the simultaneous fitting approach, the code can take into account the flux contamination for each source, due to their neighboring objects. The details of the software are described in detail in Laidler et al. (2007), Papovich et al. (2001), and Lee et al. (2012), which include a set of simulations to validate the photometric measurements and quantify its uncertainties. See also Merlin et al. (2015, 2016) for further tests and improvements on the code, branched as T-PHOT. For this paper, we chose to use the original TFIT for consistency with all previous CANDELS catalogs and also with early internal releases of the GOODS-N catalog.

In the following, we briefly summarize the main steps involved in the TFIT photometric measurements. Before running the fitting code, we perform an additional background subtraction step of the intermediate-resolution images to ensure that there are no inhomogeneous regions that could potentially bias the photometry. The iterative background fitting script is based on an IRAF script "acall" originally developed for GOODS (M. Dickinson 2013, private communication; see Guo et al. 2013 for more details). Then, the images are resampled to a pixel scale that is a multiple of the F160W pixel scale (e.g., $\sim 10\times$ for *Spitzer*/IRAC) using SWARP (Bertin 2010). Lastly,

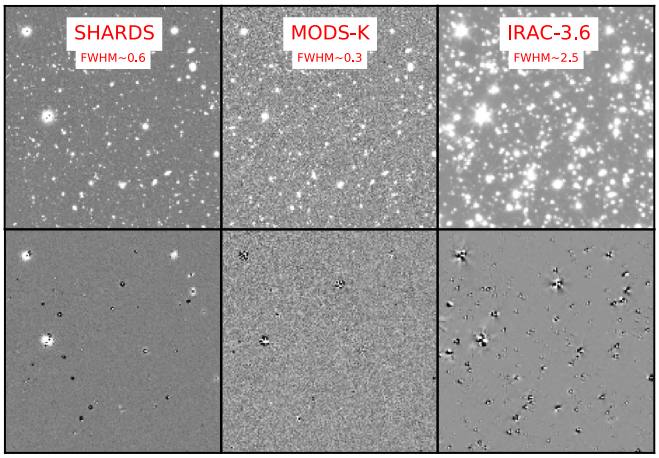

Figure 6. Example of the original image (top) and the residual image after the TFIT procedure (bottom) of several low-resolution bands as indicated in the upper panels in a representative sky region. Positive residuals in SHARDS and IRAC images are due to saturation around bright sources.

we identify and stack several bright, isolated stars in each band to determine its average PSF and to compute the transformation kernel required to match the PSF of the high-resolution F160W band. The fitting "templates" for each galaxy are computed by convolving their F160W segmentation maps with such kernels. As discussed in the previous CANDELS data papers, we apply a small "dilation" correction to the F160W segmentation map to avoid an artificial truncation of the light profiles of the sources. The dilation factor was determined following the empirical relation in Equation (3) of Galametz et al. (2013).

We run TFIT separately in all ground-based and *Spitzer*/IRAC images. As mentioned above, the flux for each object is determined by fitting its template, and those of the neighboring objects, to the intermediate-resolution image, thus obtaining a direct estimate of the possible flux contamination, due to blending. The code runs the fitting step twice, and the second iteration allows for small shifts in the PSF-matched kernels to improve lower quality fits caused by small image distortions in the intermediate-resolution images. Figure 6 shows examples

of the TFIT residual map, i.e., the result of subtracting the best-fit object templates from the original image, in three bands with different spatial resolutions, demonstrating that the fitting procedure was successful.

With the "dilation" correction, included to avoid flux loss in the outskirts of fainter objects, and assuming that the morphology of the segmentation map is not strongly dependent on the wavelength, we can consider the fluxes measured with TFIT to be analogous to the "total" fluxes measured with SExtractor's FLUX_AUTO (see also Lee et al. 2012 and Merlin et al. 2015). Therefore, we apply no further corrections to these flux measurements. The merged photometric catalog combines the *HST* fluxes measured with SExtractor and the TFIT fluxes for the intermediate-resolution bands. A quantitative analysis of the quality of the photometric catalog is presented in Section 4.

3.3. Low-resolution Mid- to Far-IR Data

Here we describe the procedure to assign mid-to-far-IR photometry to the F160W sources. Given the significant differences in depth and resolution between the optical/NIR and the IR imaging, this procedure consists of two steps. First, we build a self-consistent IR catalog using only *Spitzer* and *Herschel* data. This merged IR catalog combines prior-based extractions and direct detections starting from the higher resolution *Spitzer* IRAC and MIPS bands all the way up to the low-resolution SPIRE bands. Second, we assign those IR fluxes to some of the CANDELS/F160W sources by cross-matching the IR-only and F160W catalogs and identifying the most likely NIR counterparts to the IR detections based on brightness and proximity criteria. In the following, we briefly describe the main steps of the method. A more detailed description is provided in Appendix D.

We start by building merged, mid-to-far-IR photometric catalogs using the imaging data sets introduced in Section 2.3. The procedure to carry out the source detection and to measure the photometry is described in detail in Appendix D, as well as in several other previous works, Pérez-González et al. (2010, see also Rawle et al. 2016 and Rodríguez-Muñoz et al. 2019). Briefly, the method consists of three steps: (1) source identification in each of the IR bands starting from the deeper and higher resolution bands at shorter wavelengths and progressing toward redder, lower resolution bands by using a combination of priors and direct detections, (2) photometric measurements based on PSF fitting and aperture photometry, and (3) merging of the individual photometric catalogs to produce merged, multiband MIPS, PACS, and SPIRE catalogs. Overall, the merged IR catalog contains of the order of a few thousand detections at 24 μm and a few hundred in the PACS and SPIRE bands. This implies that the multiplicity of F160W detections per IR source ranges between five and 10. Thus, in order to obtain a one-to-one match of the two catalogs, it is necessary to identify the most likely counterparts on the basis of their NIR brightness and their coordinates in the high-resolution images.

To do so, we run a cross-matching procedure sequentially from high- to low-resolution bands, starting from F160W to MIPS, then MIPS to PACS, and lastly PACS to SPIRE. This method minimizes the multiplicity of each cross-match by choosing far-IR pairs with relatively small differences in resolution ($\sim$1.5$\times$). Then, we choose the most likely counterpart from those within the matching radius by prioritizing brightness and proximity to the low-resolution source. The cross-match with the largest multiplicity is F160W to MIPS, where the difference in resolution is almost 20$\times$. However, in this case, the brightness in the reddest IRAC band at 8 μm is a very effective discriminator, as it probes the rest-frame mid-IR region (at $z \lesssim 1.5$), which often exhibits a flux contribution from the dust emission in addition to the stellar continuum. Based on the sequential counterpart identification, each mid-to-far-IR source has a unique F160W counterpart in the final catalog. Nonetheless, we provide supplementary IR catalogs (see Appendix D.4), which indicate all of the secondary short-wavelength counterparts in each of the IR bands involved in the cross-matching procedure. These catalogs also indicate the crowdedness, i.e., the total number of counterparts to each long-wavelength, IR source, which can be used for further diagnostics.

4. Quality Assessment

In this section, we test the quality of the photometric catalog by (1) comparing the observed colors of stars to those estimated from stellar libraries, and (2) comparing the fluxes in our catalog to other published catalogs in GOODS-N. Furthermore, in Section 5, we also analyze several value-added properties computed from the fitting of the UV-to-FIR SEDs, which depend on the quality of the photometric measurement described in the previous section.

4.1. Star Identification and Colors

We compare the observed colors of the stars in our catalog to those estimated from a stellar library. We use the synthetic models of stars from the Bruzual–Persson–Gunn–Stryker atlas of stars (Gunn & Stryker 1983) that we convolve with the response curves of the different filters. Stars (unresolved sources) can be identified using a size–magnitude diagram, as they form a tight sequence with fairly constant small sizes as a function of magnitude. The left panel of Figure 7 shows the SExtractor FLUX_RADIUS against the total F160W magnitude for all sources in the catalog. Point sources (red circles) can be cleanly separated from extended sources down to $H \sim 25$ mag using the following criterion: FLUX_RADIUS $< -0.115H + 5.15$ (see also Skelton et al. 2014 for a similar approach). We further verify the accuracy of this selection by comparing it with two alternative methods: (1) the ratio of the fluxes measured in large (2″) and small (0.″5) apertures (central panel of Figure 7), which shows a similarly tight sequence at bright magnitudes ($H \leqslant 24$), and (2) the *BzK* color–color diagram (Daddi et al. 2004), which is often used to isolate distant galaxies at $z > 1.4$ (right panel of Figure 7), but is also very effective at isolating a clear stellar locus.

We note here that for some of the *HST*/ACS bands in our catalog, particularly in F606W and F775W, the new mosaics created for this paper include both preservice mission data (from GOODS and other smaller surveys) and new CANDELS data, which are separated in time by more than 5 yr. As a result, the photometry of stars, some of which can have significant proper motions, is affected by effects of systematics, such as (a) the stars having moved enough that they are partially falling out of the aperture defined by the F160W-band isophotes, and/or (b) that they are getting partially rejected as cosmic rays, due to the motion. These effects are likely present as well in

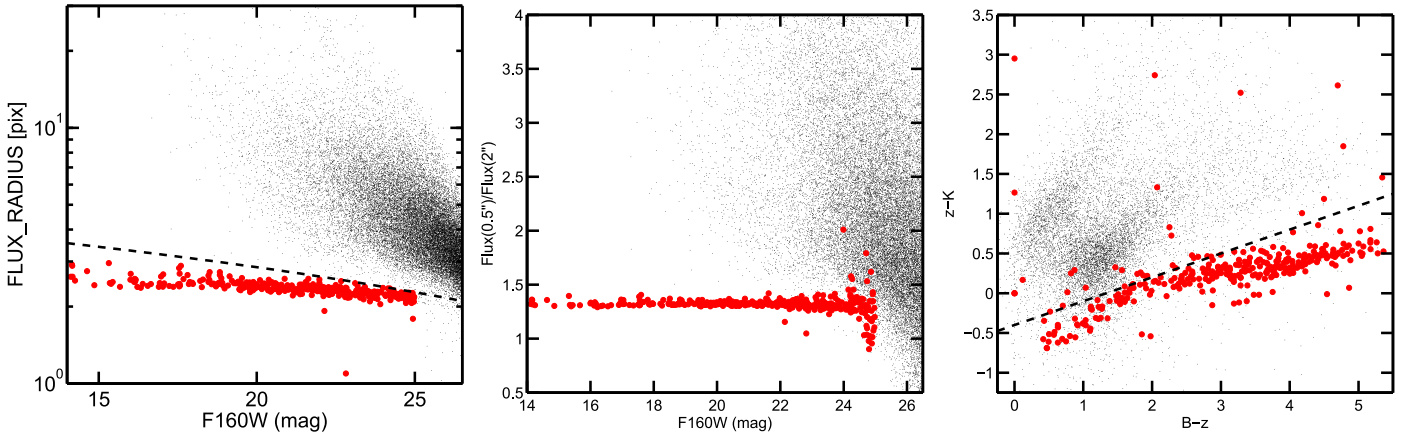

Figure 7. Left: SExtractor's FLUX_RADIUS against total F160W magnitude. Objects classified as point sources in the catalog are shown with red circles. The black dashed line indicates the selection criterion. Center: alternative selection method based on the ratio of fluxes measured in large (2.″0) and small apertures (0.″5). The stellar sequence (corresponding to the selection criterion of the left panel) at brighter magnitudes ($H < 24$ mag) is tighter with this method. However, the separation from extended sources is less clear at fainter magnitudes. Right: *BzK* color–color diagram showing another alternative method to identify stars (and galaxies; e.g., Daddi et al. 2005). The *BzK* diagram shows an excellent agreement with the other two methods for bright stars (red). However, a color-based selection (dashed black line) would also include a significant fraction of faint and less reliable sources. Note also that the *BzK* diagram relies on ground-based photometry, which is shallower than the F160W mosaic.

previous versions of the mosaics (e.g., v2), meaning that stellar photometry for those stars in either set of mosaics is suspect.

Taking this into account, we compare the colors of stars, identified with the method described above, to those of stellar models excluding colors based on either the F606W and F775W bands (see the next section for a comparison of the fluxes of nonstellar sources in these bands to the 3D-HST catalog). Figure 8 shows four of these diagrams. The observed colors of the point-like objects (blue circles) are consistent with the general distribution predicted by the stellar models showing no systematic biases. This further confirms the accuracy of the photometry, specifically for the brighter sources.

4.2. Comparison to Other Photometric Catalogs

We compare our photometry with that of the 3D-HST multiwavelength catalogs in GOODS-N (Skelton et al. 2014). The 3D-HST catalog includes 22 different photometric bands. The main difference between the latter and the CANDELS catalog in the optical-to-NIR bands is that CANDELS includes photometry in 25 optical medium bands from the SHARDS survey while the bulk of the optical ground-based data in the 3D-HST catalog is based on the broadband photometry from the Hawaii Subaru survey (Capak et al. 2004). There is, however, direct overlap between the two catalogs in the *HST* optical and NIR bands as well as in the *Spitzer*/IRAC photometry and the *U*- and *K*-band data from the Hawaii Subaru survey and the NIR MODS (Kajisawa et al. 2009), respectively.

The photometry of the 3D-HST catalog was performed following a similar methodology to ours (see Skelton et al. 2014 for a full description). Briefly, the photometry in the *HST* bands was computed using SExtractor in dual-image mode. The fluxes were measured in circular apertures and then corrected to total magnitudes based on a factor derived from the curve of growth of the F160W PSF. The photometry in the lower resolution bands was derived using a similar software to TFIT (MOPHONGO; Labbé et al. 2005, 2006, 2013). In addition to the aperture correction for the *HST* bands, two additional corrections were applied to account for Galactic extinction and small variations of the photometric zero points. These two

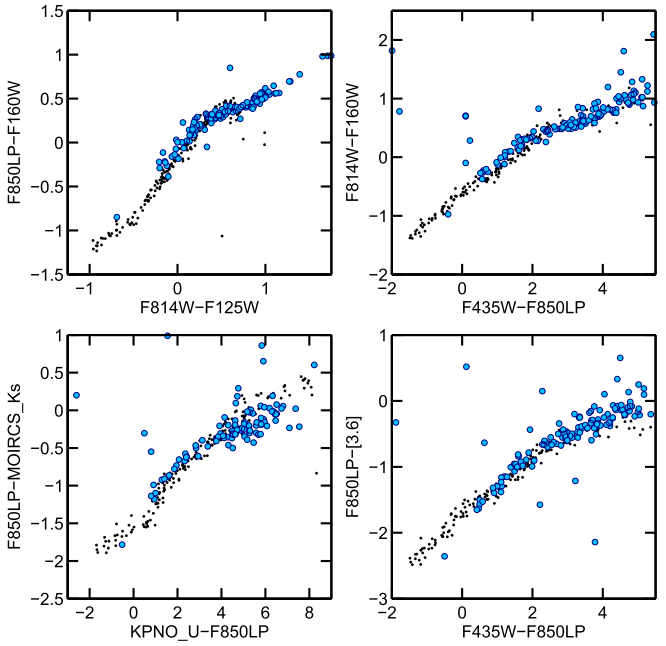

Figure 8. Color–color diagrams comparing the CANDELS GOODS-N photometry of unresolved sources classified as stars, in blue (see Section 4.1), and model stars, in black, from the Gunn & Stryker (1983) atlas of stars. The model colors of stars are computed in each filter by integrating the model SED of stars from the library over the filter transmission curves.

corrections are removed from the 3D-HST photometry before the comparisons described below.

We identify common sources between the CANDELS and 3D-HST catalogs by cross-matching the source coordinates with a maximum matching radius of 0.″3. We only include in the comparison cleanly detected sources (i.e., sources with good-quality use-flag in both catalogs). The top panels of Figure 9 show the magnitude difference between the CANDELS and 3D-HST photometric catalogs for all bands in common between the two catalogs as a function of the magnitude in each band. For each band, we only consider objects with $S/N > 3$ in both catalogs. Overall, the agreement

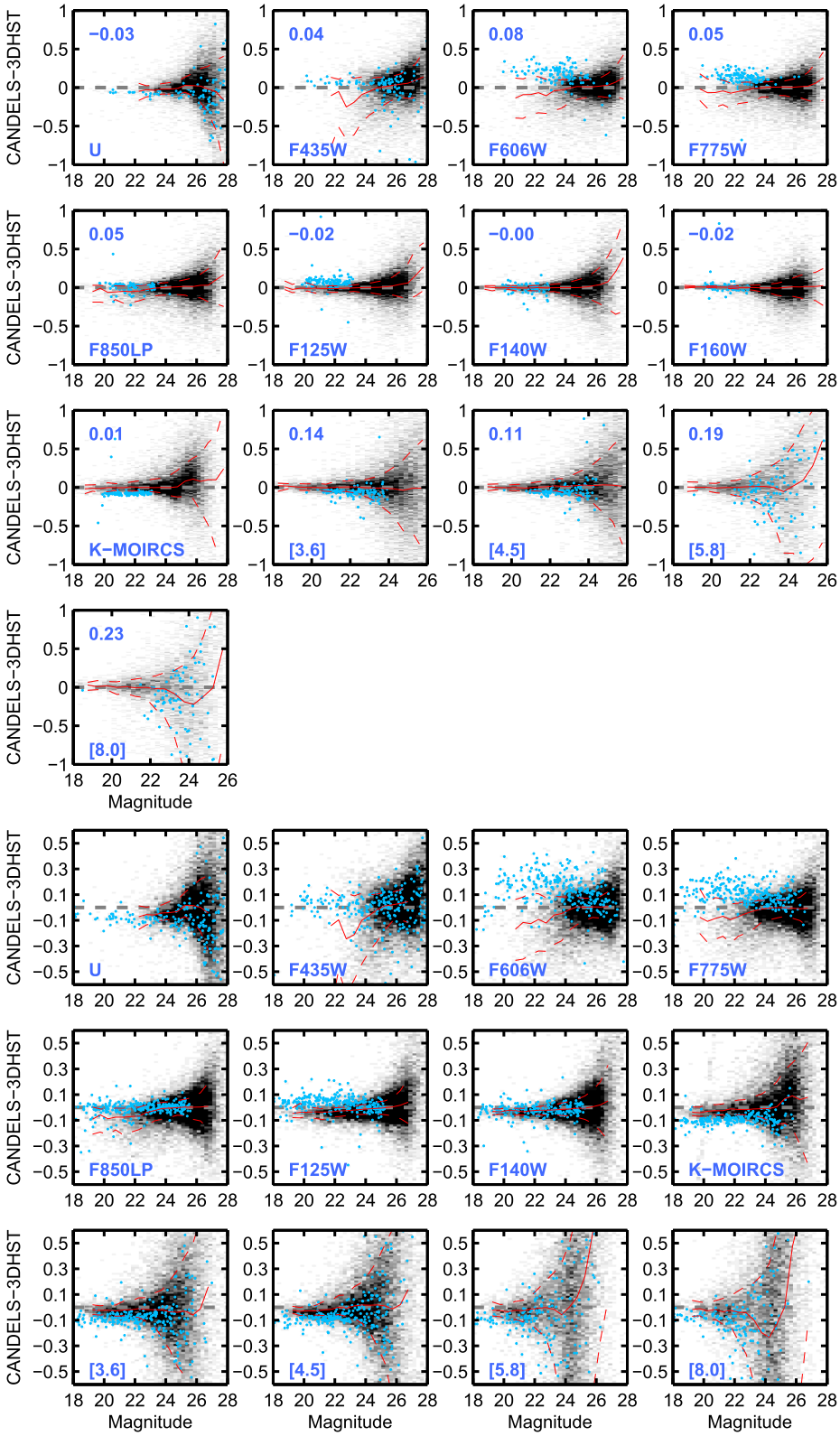

Figure 9. Photometric comparison between the CANDELS and 3D-HST multiwavelength photometry in the GOODS-N field. Top: magnitude difference (CANDELS – 3D-HST) vs. CANDELS magnitude in all bands in common between the two catalogs. For each band, we only use sources with S/N > 3 in both catalogs for comparison. The name of the bands is indicated in the bottom-left corner. The median of the magnitude difference computed in the bright magnitude range (m = 20–24 mag) is shown in the top-left corner. The gray-scale density map shows all sources, and the cyan points show stars. Both sets are corrected for the median magnitude difference to center the distributions around zero. The red solid line shows the running median (after a 3σ clipping) of the magnitude difference as a function of magnitude. The upper and lower red dashed lines show the 1σ confidence level. Bottom: color difference in band – F160W (CANDELS – 3D-HST) vs. CANDELS magnitude (e.g., top-left panel is $(U - \mathrm{F160W})_{\mathrm{CANDELS}} - (U - \mathrm{F160W})_{\mathrm{3D\text{-}\mathit{HST}}}$ vs. U_{CANDELS}). The markers, lines, and labels indicate the same as in the upper panel.

is good, and the systematic offsets (corrected and indicated in the upper-left corner) over the high-S/N magnitude range in most bands is of the order of a few hundredths of a magnitude. The small differences likely stem from the various systematic corrections that the 3D-HST catalog has applied. The largest offsets of the order of $\Delta m \sim 0.1$–0.2 mag are found in the IRAC bands. These offsets are consistent with those found in similar comparisons between the CANDELS and 3D-HST catalogs presented in previous CANDELS papers (Guo et al. 2013; Galametz et al. 2013; Nayyeri et al. 2017; Stefanon et al. 2017). Note that, as indicated in the previous section, the stellar loci for the *HST*/ACS bands F606W and F775W exhibit systematic deviations (cyan circles) because the positions of some stars in the merged multiepoch mosaic have changed due to proper motions.

To further verify the accuracy of the photometry, we also analyze the difference in the colors as a function of magnitude between the two catalogs, where the color is defined as the magnitude difference in a given band minus F160W. In principle, a color comparison is more straightforward as it should naturally factor out any dependence on the aperture correction. This comparison is shown in the bottom panels of Figure 9, and, again, we find an excellent agreement. Overall, these tests indicate that the flux measurements in both catalogs have been performed in a robust and self-consistent manner.

5. Value-added Properties

In this section, we present the value-added properties for the galaxies in the CANDELS GOODS-N catalog computed from the fitting of their UV-to-FIR SEDs to stellar population synthesis models and dust emission templates. We also present emission-line measurements derived from the WFC3 G102 and G141 grism spectroscopy.

5.1. Photometric Redshifts

Here we discuss the photometric redshift estimates for the galaxies in the CANDELS GOODS-N catalog computed from SED fitting. The main difference between the galaxy SEDs in GOODS-N with respect to the other four CANDELS fields is that this catalog includes photometry in 25 medium bands of the SHARDS survey ($R \sim 50$; $\lambda = 0.50$–0.95 μm) and *HST*/WFC3 grism observations in both G102 and G141, thus allowing for a continuous wavelength coverage from $0.9 \leqslant \lambda \leqslant 1.7$ μm with a resolution of $R \sim 210$ and 130, respectively. Together, all these data sets provide remarkable spectral resolution on a galaxy-by-galaxy basis that is uniquely suited to provide high-quality, SED-fitting-based properties.

The use of higher spectral resolution photometric bands, such as medium- or narrowband filters has been shown to improve the accuracy of the photometric redshifts up to the few percent level (e.g., Ilbert et al. 2010; Whitaker et al. 2011; Straatman et al. 2016). The inclusion of WFC3 grism spectroscopy provides even higher spectral resolution capable of detecting emission lines, and thus provides redshift estimates of similar quality to those from typical, ground-based spectroscopic surveys (e.g., Atek et al. 2010; Cava et al. 2015; Treu et al. 2015; Bezanson et al. 2016; Momcheva et al. 2016).

Given that the number of available spectrophotometric data sets for any given galaxy (i.e., whether they have SHARDS and/or grism data) depends on its magnitude and its location within the WFC3 mosaic, we implemented a three-tier classification for the photometric redshift estimates with increasing spectral resolution data. Tier 3 consists of photometric redshifts determined from broadband photometry only. Although these redshifts are based on lower resolution data, they can be computed for all of the galaxies in the catalog using the same set of input fluxes and therefore provide a uniform, homogeneous set of baseline redshifts. The second-tier redshifts are based on the SED fitting to both broadband and SHARDS medium-band data, and the first tier includes broad- and medium-band data plus the WFC3 grism spectra. Roughly ~80% of the galaxies in the catalog lie in the region of GOODS-N covered by the SHARDS medium-band survey, and a large fraction of those, ~60% at $H < 24$ mag, also have grism detections in either G141 or G102 (more details in Section 5.1.5). All of these galaxies have a more detailed SED coverage, and therefore, their photometric redshifts are likely to be more precise. In the following, we describe the methods used to compute photometric redshifts for the galaxies in each of the three quality tiers.

5.1.1. Tier 3: Broadband-based Photometric Redshifts

Following the same approach as in previous CANDELS papers, we computed several estimates of the photometric redshifts using a number of different codes, e.g., `EAZY` (Brammer et al. 2008), `HyperZ` (Bolzonella et al. 2000), `SpeedyMC` (Acquaviva et al. 2011), etc., based either on χ^2 and MCMC-fitting methods and using different templates and SED-modeling assumptions (see Appendix B for more details on all the different codes). As a common practice, each of the methods fine-tuned the performance of the photometric redshifts by computing small zero-point corrections to the photometric fluxes by minimizing the difference between the observed fluxes and those expected from the best-fit templates. Because these corrections are dependent on the fitting codes and template libraries, we followed the same approach as in the previous CANDELS data papers, and we did not include such adjustments in the photometric catalog. However, we report the average photometric zero-point offsets adopted by each group in Table 2.

As shown in Dahlen et al. (2013), using the median of multiple photo-z estimates provides a more accurate prediction of the true redshift, and it helps mitigate some of the most common problems, such as systematic offsets and catastrophic outliers. Here we compute the median photometric redshift based on five different codes. All of these codes used the same set of broadband photometric data for all galaxies in the sample. We adopt these median values as the tier 3 redshift estimates. Note that, while the tier 2 and 1 photometric redshift estimates presented in the following sections are significantly more accurate than the tier 3 redshifts for many galaxies, the tier 3 estimate is the only value available for those galaxies without SHARDS and/or grism coverage. Furthermore, because the improvement in the quality of the photo-z owing to the addition of high spectral resolution data is magnitude dependent, the tier 3 photo-z's will also be very similar to tier 2 and 1 values for many faint, typically high-z, galaxies.

5.1.2. Tier 2: Broad- and Medium-band Photometry Photometric Redshifts

The tier 2 photometric redshift estimates are based on the fitting of the galaxy SEDs that include both broadband photometry and the 25 medium bands of the SHARDS survey.

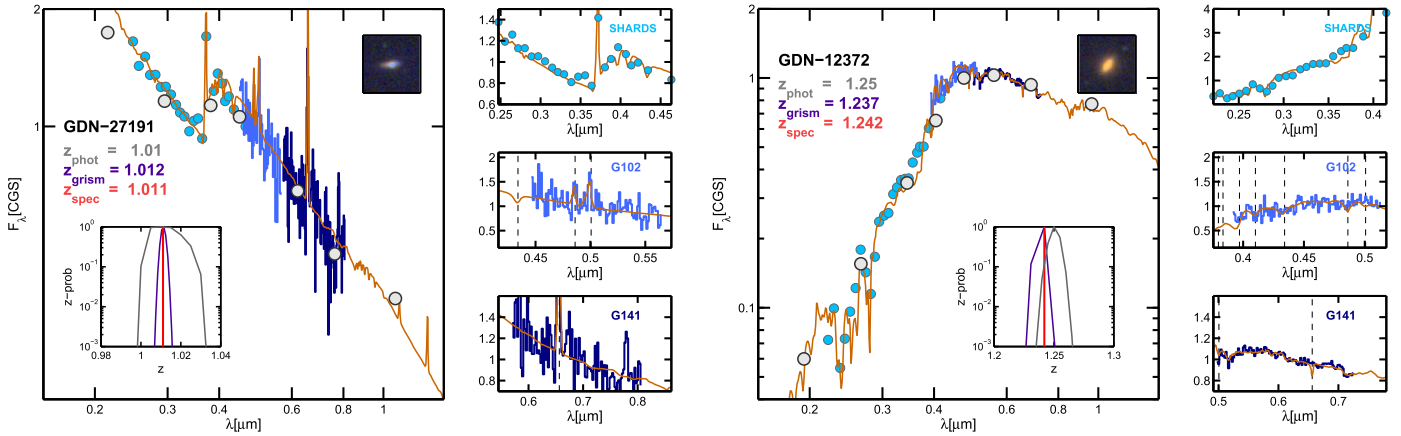

Figure 10. SEDs of a star-forming (left) and a quiescent (right) galaxy in the CANDELS/GOODS-N region. The gray circles indicate broadband photometry. The blue circles show the SHARDS medium-band data and the blue lines, from light to dark shading, the G102 and G141 grism spectroscopy. The rightmost panels in each figure show a zoom-in into the key spectral regions for each of these data sets and highlight the most prominent emission and absorption features in the spectrum. The insets show the redshift probability distributions computed from the fitting to broadband data (gray), and with the addition of SHARDS and grism data (blue). The red line indicates the spectroscopic redshift.

These redshifts are available to the nearly 80% of the galaxies that lie in the overlapping region between the CANDELS and SHARDS mosaics (see Figure 1). The photometric redshifts are computed using a slightly modified version of EAZY (Brammer et al. 2008) adapted to take into account the spatial variation in the effective wavelength of the SHARDS filters depending on the galaxy position in the SHARDS mosaics (see Section 2.2.2).

5.1.3. Tier 1: Broad- and Medium-band Photometry Plus Grism Spectroscopy Photometric Redshifts

The tier 1 photometric redshift estimates are based on the fitting of galaxy SEDs that include the broad- and medium-band photometry from tier 2 and the WFC3 grism spectroscopy. The accuracy of the grism-based photo-z's depends critically on whether any prominent emission line falls within the observed spectral range (see, e.g., Figure 2), and if such a line is detected with high S/N. Given the limited spectral range of the grism, the majority of the emission-line detections in either G141 or G102 consist of only one prominent line. However, if the S/N of that line is high enough (S/N $\gtrsim$ 5), the use of photo-z priors, such as the ones computed in tier 2 or 3, can help break the redshift degeneracies and provide a very precise redshift determination ($\Delta z \lesssim$ 1E–3; e.g., Momcheva et al. 2016).

In order to take full advantage of both broad- and medium-band photometry and the grism spectroscopy, we computed the tier 1 photometric redshifts using the SED-fitting code developed by the 3D-HST survey and discussed in detail in Brammer et al. (2012) and Momcheva et al. (2016). This code was designed to estimate redshift probability distribution functions (PDFz) based on the constraints from the broad- and medium-band photometry as well as their G141 grism spectroscopy. Here we use a slightly modified version of the code, which makes use of both G102 and G141 spectroscopy in this calculation. Briefly, the redshift determination is done iteratively in three steps, first using only the photometric SED to obtain a coarse constraint on the PDFz, then fitting the grism data alone over a finer redshift grid, and lastly fitting both together, multiplying the likelihood of all redshift distributions. The first iteration of the fitting uses the preliminary photo-z estimate from the previous section as a prior on the fit to broad- and medium-band photometry. The fit to the grism spectrum is done in 2D to take into account the impact of the spatial extent of the source in the spectral direction. This is done by using the SExtractor segmentation map of each source in the direct F105W and F140W images for G102 and G141, respectively.

An advantage of the iterative fitting method is that the resulting PDFz defaults to the tier 3 or 2 photometry-only solution in all cases where there is no significant contribution to the probability distribution from the fit to the grism data. Thus, the improvement in the accuracy of the PDFz over the photometry-only case depends on the significance of detected features on the grism spectra, e.g., strong emission lines, continuum breaks, or absorption lines (see Figure 10 for two different examples of these possible cases).

5.1.4. Quality Assessment of the Photometric Redshifts

Figure 11 compares our three-tier photometric redshift estimates versus spectroscopic redshifts for galaxies with both G102 and G141 grism spectra and good-quality spectroscopic redshifts. Each panel illustrates the gradual improvement in the overall accuracy of the photo-z with the addition of higher spectral resolution data to the SED fit, starting with the broadband-only fits (tier 3, left panel) and progressively including the SHARDS medium bands (tier 2, middle panel), and the grism spectroscopy (tier 1, right panel). The normalized median absolute deviation ($\sigma_{\rm NMAD}$) of $\Delta z = z_{\rm phot} - z_{\rm spec}$, defined as $\sigma_{\rm NMAD} = 1.48 \times {\rm median}\left(\left|\frac{\Delta z - {\rm median}(\Delta z)}{1+z_{\rm spec}}\right|\right)$, improves significantly by a factor of $\sim$10 and 12 with the use of medium bands and grism spectra, respectively. Similarly, the fraction of outliers, defined as $\eta = \Delta z/(1+z) > 0.15$, decreases from 4.2% to 3.3% and 2.7% in those cases. The bottom panels of Figure 11 show the dependence of the $\Delta z/(1+z)$ scatter with redshift for the three cases. The median value of such a scatter corrected by the median offset in $|\Delta z|$ is, by definition, $\sigma_{\rm NMAD}$. For the tier 3 redshifts, the scatter is relatively constant up to $z \sim 1.5$ and increases by a few percent at higher redshifts. The addition of SHARDS photometry significantly improves the accuracy of the tier 2 redshifts at $z < 1.5$ by almost a factor of 7. However, the impact of the medium-band data at higher redshifts ($z > 1.5$) is almost

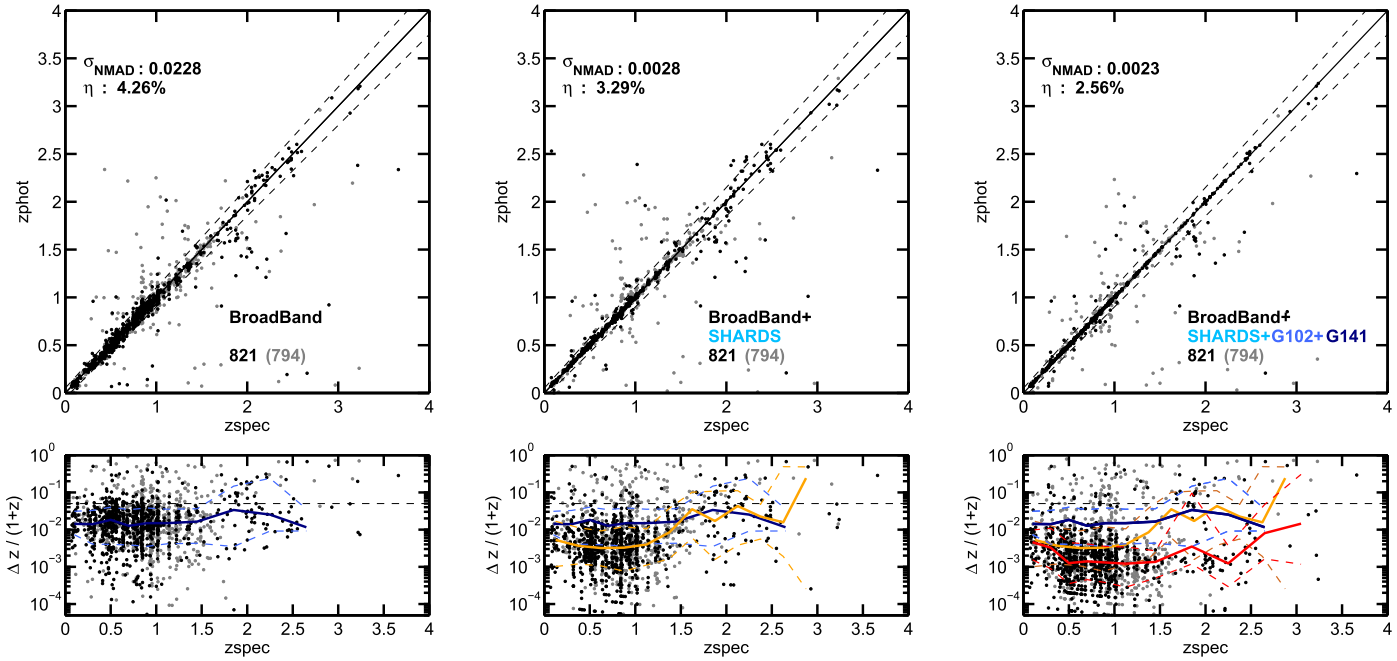

Figure 11. Comparison of our multi-tiered photometric redshifts vs. spectroscopic redshifts for galaxies with both G102 and G141 spectra and good-quality flag spectroscopic redshifts. The photometric redshifts are estimated using broadband photometry only (tier 3, left), adding the SHARDS medium bands (tier 2, center), and adding the G102 and G141 grism spectroscopy to the SED fit (tier 1, right). The black and gray circles indicate sources with high- and medium-quality spectroscopic redshift flags, respectively. The bottom panels show the overall accuracy ($\Delta z/(1+z)$) of the photometric redshift as a function of redshift. The colored solid and dashed lines show the running median and 68% confidence regions. The black dashed line indicates the outlier threshold ($\Delta z/(1+z) = 0.15$). Both the accuracy ($\sigma_{\rm NMAD}$) and the fraction of catastrophic outliers (η) improve with the addition of higher spectral resolution photometry.

negligible. This is because the most relevant spectral features (e.g., Balmer or 4000 Å break) shift out of the SHARDS spectral range around that redshift, and thus diminish the constraining effect of the medium bands. The addition of *HST* grism spectroscopy does not significantly change the overall $\sigma_{\rm NMAD}$ accuracy of the redshift with respect to the tier 2 case. Nonetheless, it consistently reduces $\Delta z/(1+z)$ to ∼0.01% for galaxies with clear emission lines in the redshift range $z = 0.4$–3. As a result, the relative improvement of the tier 3 redshifts at low-z is smaller than a factor of 3, but it can increase to almost a factor of 10 for high-z galaxies.

Figure 12 shows the comparison of our photometric redshifts versus spectroscopic redshifts (left) and versus the photometric redshifts from the 3D-HST survey (right), which also make use of G141 spectra (Momcheva et al. 2016). This comparison is limited to galaxies with G141 spectra in both catalogs and good-quality spectroscopic redshifts. The purpose of this comparison is twofold, first showing the relative impact of adding SHARDS medium-band photometry and G102 spectra versus the G141-only case of 3D-HST, and second, to verify that our redshift estimates are consistent with theirs for the galaxies in which the G141 data is the key contributor to the quality PDFz. The redshift dependence on $\Delta z/(1+z)$ shown in the bottom panels of Figure 12 indicates that our photometric redshift accuracy is slightly higher at $z \lesssim 0.7$, due to the additional constraints from SHARDS and G102, which are both more effective at picking up emission lines at low -z (see Figure 2). At higher redshifts our estimates are in excellent agreement with those from 3D-HST.

Note that Figures 11 and 12 include only spectroscopically confirmed sources with clear emission lines. Therefore, the comparisons are biased toward the best possible targets for redshift determination using the *HST* grisms. This bias consequently boosts the accuracy redshift estimates, i.e., if a galaxy has a confirmed optical emission line, it is easier for the NIR grism to pick up another line in a different spectral range, thus providing a high-precision (0.01% level) redshift estimate. Figure 13 compares photometric and spectroscopic redshifts for all galaxies with reliable spectroscopic flag regardless of their *HST* grism detectability. The number of galaxies in the figure is more than 1.5× larger than in the previous comparisons, and it includes a significant amount of galaxies from tier 2, i.e., galaxies for which the grism spectra do not contribute decisively to the PDFz. Although still biased toward galaxies with emission lines, this comparison provides a more representative estimate of the overall quality of the photometric redshifts for the whole, magnitude-limited sample. The accuracy is slightly lower than in the previous comparisons, but it is still significantly better than the ∼1% precision typical of broadband-only surveys ($\sigma_{\rm NMAD} \sim 0.3\%$ with $\eta \sim 4\%$).

5.1.5. Breakdown of the Photometric Redshift Tiers

Because the quality of the photometric redshifts depends on the data used for the SED fit, it is useful to report the relative fractions of galaxies in the sample that have observations in each of the relevant data sets or photo-z tiers discussed in the previous sections. In terms of area coverage, approximately ∼80% of the CANDELS F160W mosaic is covered by the SHARDS medium-band imaging, and an additional ∼3% of the non-SHARDS area is covered by the WFC3 G102 and/or G141 mosaics. Thus, less than ∼20% of all galaxies have tier 3 redshifts, i.e., based on broadband photometry only. Among the 80% of the sample with SHARDS observations, the relative fraction of galaxies with tier 2 and tier 1 redshifts, i.e., the fraction of galaxies with both SHARDS photometry and *HST*

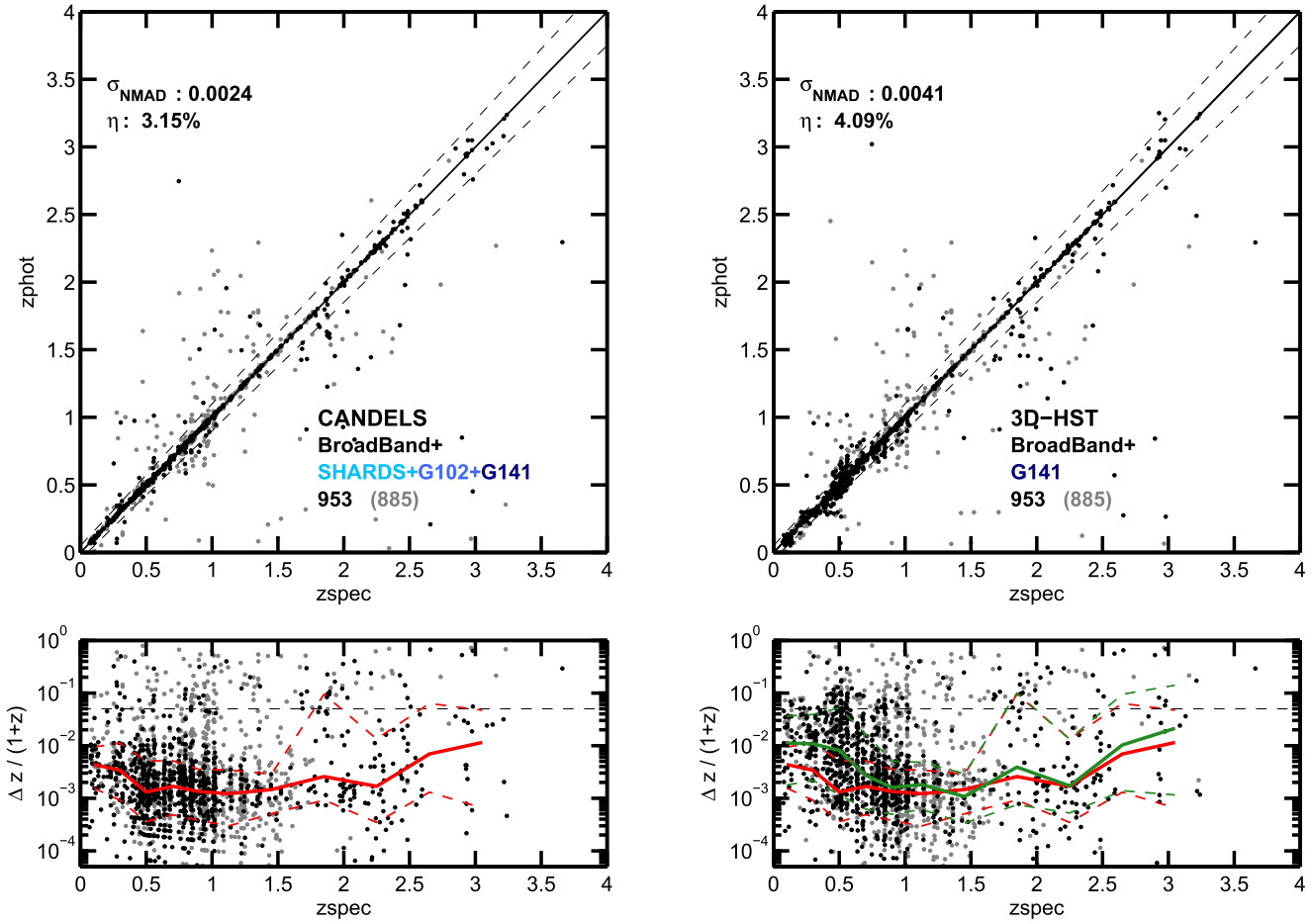

Figure 12. Comparison of our photometric redshifts vs. spectroscopic redshifts (left) and the 3D-HST photometric redshifts (right) from Momcheva et al. (2016), which are based on broadband photometry and G141 spectra. This comparison is restricted to galaxies with G141 spectra in both CANDELS and 3D-HST and having good-quality spectroscopic redshifts. The lines in the bottom panels show the redshift evolution of the median $\Delta z/(1+z)$ for the CANDELS (red) and 3D-HST (green) samples. The addition of medium bands and the blue grism improves the quality of the photometric redshifts predominantly at low z ($z \lesssim 0.7$), while both photometric redshift estimates are fully consistent at medium and high z. The colors of the points and lines have the same meaning as in Figure 11.

grism spectra is magnitude dependent. For a magnitude limit of $H < 24$ mag, the breakdown is 26% and 74% in tiers 2 and 1, and 35% and 65% for $H < 25$ mag. Relative to the whole catalog, these numbers imply that 60% and 52% of all galaxies have tier 1 redshifts at $H < 24$ and 25 mag, respectively.

For the galaxies with observations in both grisms, the SED-fitting procedure combines the G102 and G141 spectra for the redshift determinations. However, given the lower sensitivity of the G102 grism (see the next section for more details), some galaxies might only have G141 detections. For galaxies detected in at least one of the grisms and a magnitude limit of $H < 24$ mag, the breakdown between galaxies with both G141 and G102 spectra versus only G141 spectra is approximately 55% to 33%. The remaining 12% of the galaxies have only G102 observations. The latter are typically located in a region with G141 coverage; however, differences in the orientation of the G102 and G141 observations can make the G141 spectra unavailable or severely contaminated.

5.2. G102/G141 Emission-line Fits

We compute emission-line fluxes and observed-frame equivalent widths (EWs) from the G102 and G141 spectra using the same software described in the 3D-HST survey paper, Momcheva et al. (2016). Briefly, this code adopts the 2D continuum template determined from the photometric redshift fit to build a 2D model and then adds Gaussian lines with unresolved line widths of $\sigma = 100\,\mathrm{km\,s^{-1}}$. Each potential line is treated separately by means of independent line-template normalizations relative to the continuum. The code fits the observed grism data to the model using the `emcee` sampler (Foreman-Mackey et al. 2013) to determine the marginalized posterior distribution functions of the parameters for the individual line-template normalizations. These are converted directly to line fluxes and observed-frame EWs in physical units (i.e., $\mathrm{erg\,s^{-1}\,cm^{-2}}$ and Å, respectively). Only the lines that fall within the rest-frame spectral range of the grism data, as determined from the grism redshifts, are included in the model (see Table 4 of Momcheva et al. 2016 for a complete list of all the species included in the fit). The line fluxes are implicitly normalized to the total broadband photometry, as the spectra are scaled to match the photometric data. Note that the line-template normalization is not required to be positive, and therefore, it is not restricted to measure emission lines, i.e., it can also provide EW estimates for absorption lines.

The MCMC chains provide a robust estimate of the uncertainties in the fit, which are primarily determined by two effects: (1) the wavelength dependence of the grism throughput, and (2) the galaxy size (i.e., the area of the effective aperture of the 2D spectrum fit). Figure 14 illustrates these two effects separately

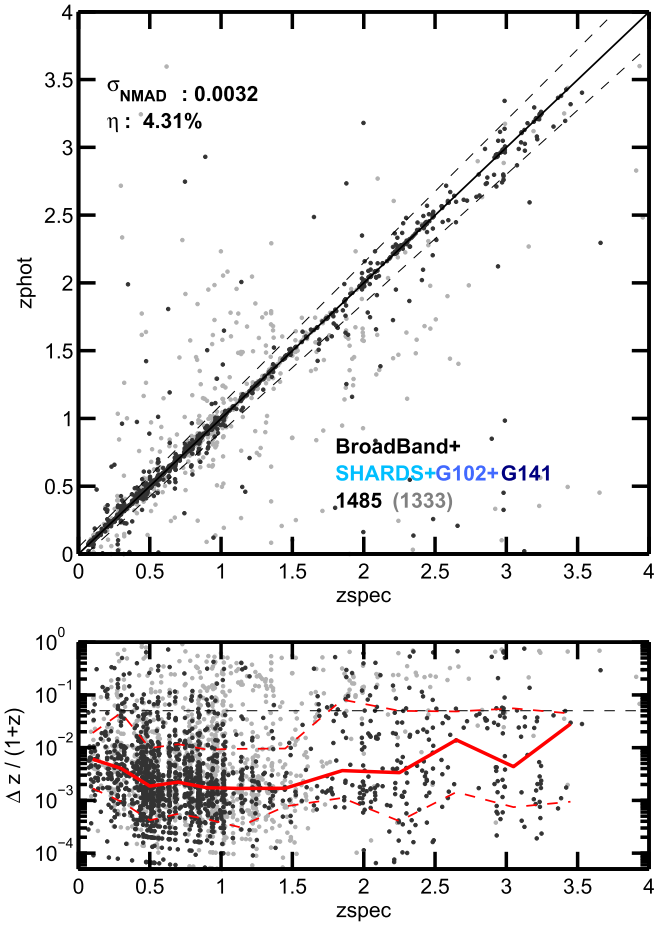

Figure 13. Comparison between our three-tier photometric redshifts vs. spectroscopic redshifts for galaxies with good-quality spectroscopic redshift flag in the GOODS-N field. The redshift tier breakdown is approximately 20%, 21%, and 59% in tiers 3, 2, and 1, respectively. The colors of points and the lines in the bottom panel have the same meaning as in Figures 11 and 12.

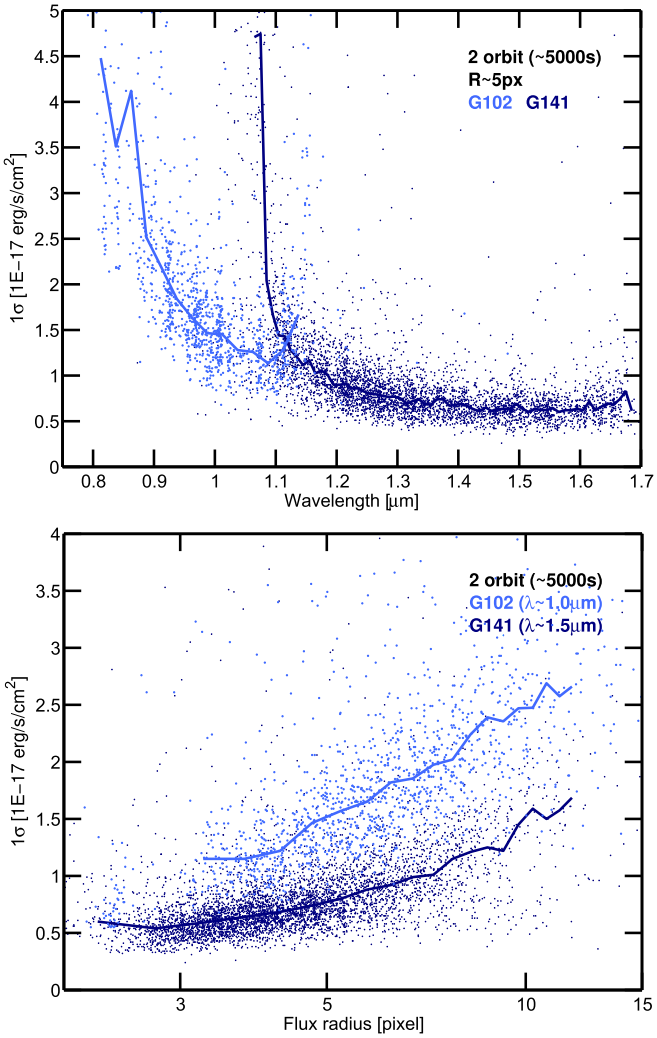

Figure 14. 1σ emission-line sensitivity in the G102 and G141 spectra as a function of the observed wavelength (upper panel) and the `SExtractor flux_radius` size of the galaxies (lower panel). In order to illustrate the effect of the two main drivers of emission-line sensitivity separately, the upper panel shows galaxies with similar sizes of $R \sim 5$ pixels, typical for resolved galaxies, while the bottom panel shows galaxies with emission lines measured around the same wavelengths, $\lambda \sim 1.0$ and 1.5 μm for G102 and G141. At those wavelengths, the average line uncertainty of the two-orbit-depth grism spectra for a resolved galaxy are 0.75 and 1.5×10^{-17} erg s^{-1} cm^{-2} in G141 and G102, respectively.

for the G102 and G141 spectra. The top panel depicts the wavelength dependence of the sensitivity for sources with `SExtractor FLUX_RADIUS` = 3–5 pixels, while the bottom panel depicts the dependence on the galaxy size at the peak sensitivity wavelength of each grism. Overall, a typical resolved galaxy exhibits a 1σ flux uncertainty of $\sim 1.5 \times 10^{-17}$ erg s^{-1} cm^{-2} in G102 and $\sim 0.8 \times 10^{-17}$ erg s^{-1} cm^{-2} in G141 for two-orbit-depth exposures. The lower sensitivity threshold of the G102 grism compared to G141 is largely due to its higher spectral resolution (i.e., the line flux spreads over more pixels and thus reaches a lower the S/N per resolution element for similar exposure times). The noise levels are in good agreement with previously published sensitivities of the *HST* NIR grisms (e.g., Atek et al. 2010; Brammer et al. 2012; Trump et al. 2013; Treu et al. 2015).

Figure 15 shows the redshift distribution and the cumulative fraction as a function of magnitude for emission-line galaxies detected in the G102 and G141 spectra. The lower sensitivity of the G102 grism results in approximately half the number of emission-line detections as in G141 at S/N $\gtrsim$ 3 or 5. Furthermore, its bluer central wavelength implies that the majority of those detections in G102 have lower median redshifts than those in G141. As indicated in Figure 2, the bluest of the most prominent emission lines, [O II], shifts out of the G102 spectral coverage at $z \sim 2$, while it can be detected in G141 up to $z \sim 3.5$. This is consistent with the distributions shown in the histograms of Figure 15. The overall brighter magnitudes of the emission-line galaxies detected in G102 imply that the majority of those galaxies are also detected in G141 for redshifts $z \gtrsim 0.6$ (i.e., when the Hα line shifts into the G141 passband). This naturally provides simultaneous detections of two relevant lines in the combined data set, for example, Hα and Hβ at $z = 0.6$–1.3, or [O III] and [O II] at $z = 1.3$–2.0. The majority (>90%) of the G102 emission-line detections with S/N $\geqslant$ 3 (5) have magnitudes $H \leqslant 23.5$ (23), while the G141 detections are about 1 mag fainter with S/N $\geqslant$ 3 (5) at $H \leqslant 24.5$ (24). Relative to the full galaxy catalog, these numbers imply that ~25% of the galaxies with $H < 24.5$ have at least one emission line detected in the G141 grism, and ~35% of the galaxies with $H < 23.5$ have two emission lines detected, one on each of the G102 and G141 grisms.

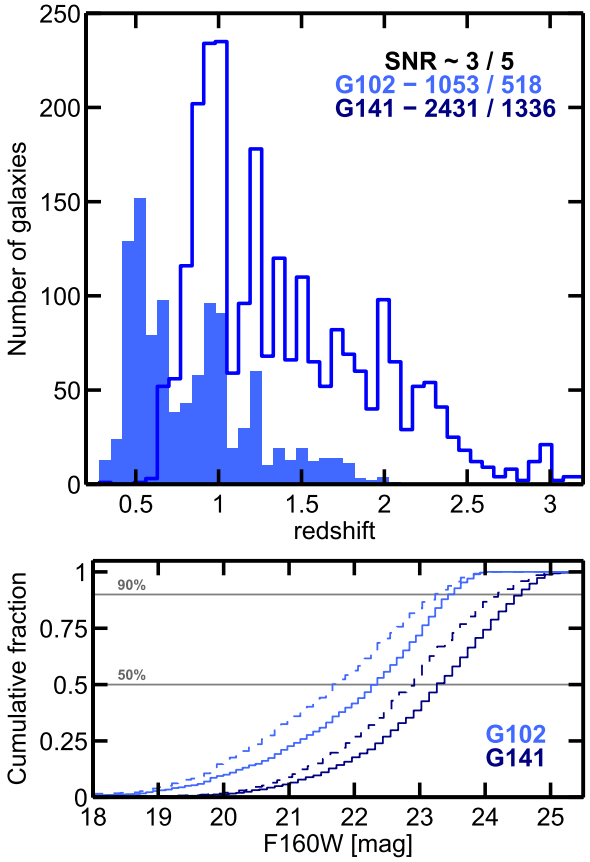

Figure 15. Top: redshift histogram for galaxies with clear emission lines (S/N $\geqslant$ 3) detected in the G102 (empty light blue) and G141 spectra (filled dark blue). Bottom: cumulative F160W magnitude distribution for the emission-line galaxies in the upper panel. The dashed and solid lines indicate the distributions down to S/N = 3 and 5, respectively.

In order to validate the quality of the emission-line extractions, we compare the line fluxes measured in the G141 grism to those released by the 3D-HST survey in Momcheva et al. (2016). Note that while we make use of the reduced G141 images released by the 3D-HST survey, the 2D extraction of the spectra, the redshift determination, and the line measurements depend on our object detection procedure and on our SEDs. Therefore, this is a useful quality check to verify that our extraction and SED-fitting procedures are accurate. This comparison is shown in the left panel of Figure 16, which illustrates that the fluxes from both catalogs are in excellent agreement even for the faintest emission lines with $f_\lambda \sim 1 \times 10^{-17}$ erg s^{-1} cm^{-2}, which have low S/N $\lesssim$ 3.

The right panel of Figure 16 extends this validation test to the emission lines detected in G102 by comparing the flux measurements for emission lines that are simultaneously detected in both G102 and G141. This is only possible for a small subsample of galaxies in narrow redshift ranges where the most prominent lines lie in the reddest and the bluest sides of the G102 and G141 wavelength ranges, respectively ($z \sim 0.7$ for Hα and $z \sim 1.3$ for [O III]/Hβ). In this case, the comparison is between fully independent measurements performed in different data sets, and we also find good agreement for all emission lines with S/N $\gtrsim$ 3. The scatter is consistent with the $\sim$1.5$\times$ dispersion reported in Momcheva et al. (2016) for the comparison between grism and ground-based spectroscopic measurements. Note also that in order to measure the same line in both grisms, the fluxes are typically measured near the edges of the spectra, around $\lambda_{\rm obs} \sim 1.1$ μm, where the sensitivities are lower (see Figure 14).

5.3. Rest-frame Colors and Stellar Population Properties

We compute stellar population properties and rest-frame luminosities by fitting the observed SEDs to galaxy templates and adopting the best photometric redshift. We used the best available SED for every galaxy including broad- and medium-band photometry, but not the grism spectroscopy. First, we estimate the stellar masses and other physical properties of the galaxies, such as stellar ages, dust extinctions, or SFRs by fitting the SEDs with the codes FAST (Kriek et al. 2009) and Synthesizer (Pérez-González et al. 2005, 2008). The redshift is fixed to the best redshift estimate, i.e., spectroscopic where available and photometric otherwise. The modeling assumptions for both codes are as follows: we use the Bruzual & Charlot (2003) stellar population synthesis models with a Chabrier (2003) IMF and solar metallicity. We assume exponentially declining star formation histories with a minimum e-folding time of $\log_{10}(\tau/{\rm yr}) = 8.5$, a minimum age of 40 Myr, $0 < A_V < 4$ mag, and the Calzetti et al. (2000) dust attenuation law. The only difference between the FAST and Synthesizer fits is that the latter uses SED templates that include emission lines. In addition to the stellar population properties, we also estimate rest-frame luminosities and colors for all galaxies using EAZY (Brammer et al. 2008). This code computes the rest-frame luminosity in a set of typical photometric filters (see Table 9), and then derives rest-frame colors as the ratio of the luminosities in two of those filters.

Figure 17 illustrates the consistency of these rest-frame colors by comparing the distribution of galaxies in the *UVJ* color–color diagrams (Williams et al. 2009) based on the CANDELS/GOODS-N catalog and the CANDELS/GOODS-S catalog of Guo et al. (2013; i.e., the deepest CANDELS fields) in three redshift bins. The color distributions are qualitatively very similar, and they are also consistent with the *UVJ* diagram for the 3D-HST sample (Figure 26 of Brammer et al. 2012). The mass distribution in the color–color diagram is also consistent with previous results, which showed that the majority of massive galaxies at $z \gtrsim 1$ tend to be intrinsically red ($U - V$), either because of dust obscuration or because they host older stellar populations (Brammer et al. 2011). The *UVJ* diagram is indeed particularly useful for making this distinction because it breaks the degeneracy between the dusty star-forming galaxies (SFGs) and quiescent galaxies with low levels of star formation. Both the old and the dusty populations have red $U - V$ colors (upper-left region), but dusty SFGs typically have redder $V - J$ colors (e.g., Whitaker et al. 2012). The black lines indicate the selection threshold that is typically used to distinguish these two populations. In the following, we adopt the *UVJ* criterion to divide the GOODS-N sample into star-forming and quiescent galaxies at all redshifts. We validate the accuracy of this selection criterion by comparing the evolution in the number densities of these two populations to the results from previous works (see below).

Figure 18 shows the comparison of the stellar masses computed with FAST and Synthesizer. The overall difference between these estimates for the whole galaxy sample is consistent with zero within the usual scatter of $\sim$0.3 dex, typical of the comparison of stellar masses derived with

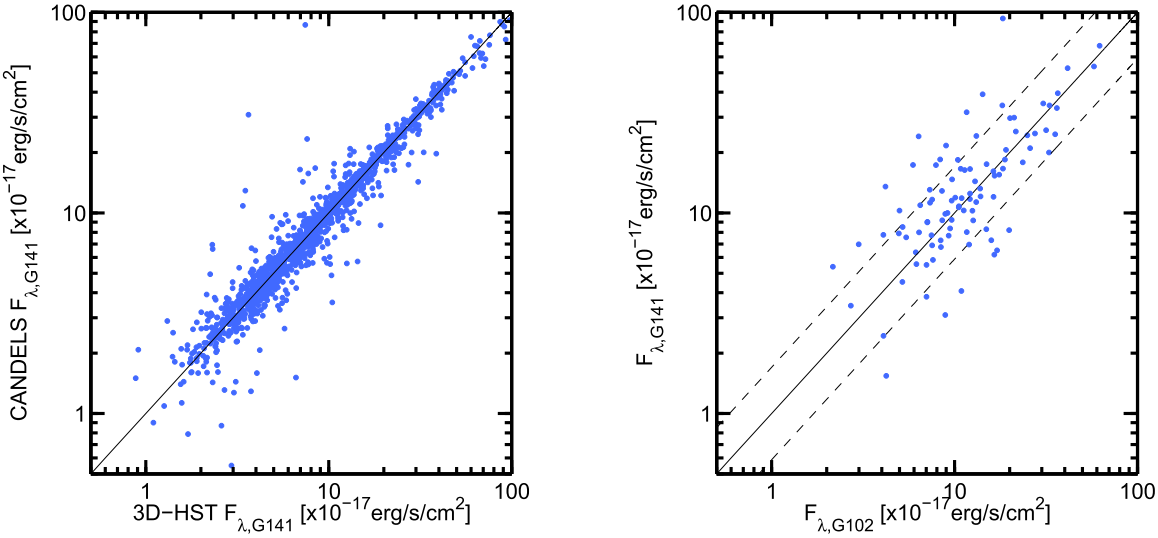

Figure 16. Left: comparison of emission-line fluxes measured in the G141 spectra by the 3D-HST survey (Momcheva et al. 2016) and our measurements in this paper. Both measurements come from the same G141 images but using different source extractions and SED fits to estimate the line redshift and fluxes. The results are in excellent agreement and demonstrate the consistency of the measurements. Right: comparison of emission-line fluxes for galaxies in which the same line (either Hα or [O III]/Hβ) can be detected simultaneously in both of our G102 and G141 measurements. This is only possible for a small fraction of the emission-line galaxies at narrow redshift ranges around $z \sim 0.7$ (for Hα) and $z \sim 1.3$ (for [O III]/Hβ).

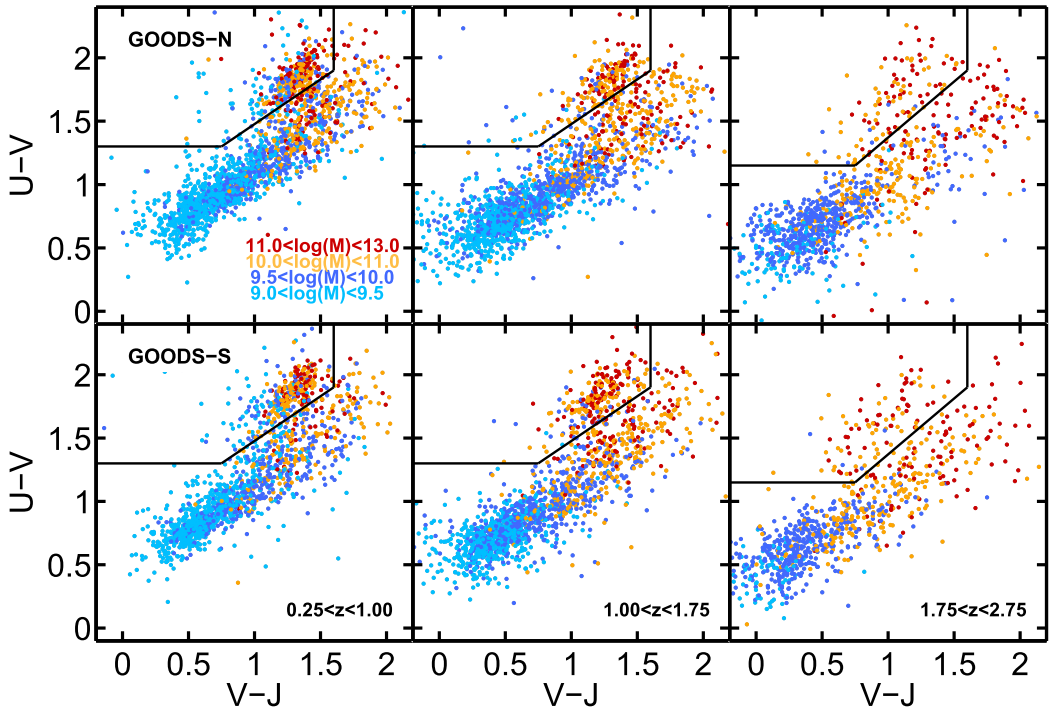

Figure 17. Rest-frame *UVJ* diagram for galaxies in the deepest CANDELS fields, GOODS-N (this paper) and GOODS-S (from Guo et al. 2013). Each column presents the rest-frame colors for galaxies in the two fields at the same redshifts, with redshift increasing from left to right. The diagram is color-coded by mass, with the lowest mass galaxies in blue and the highest mass galaxies in red, as shown by the legend in the upper-left panel. The black lines indicate the selection box used to separate quiescent from SFGs, based on Williams et al. (2009).

different codes (e.g., Mobasher et al. 2015; Nayyeri et al. 2017). Furthermore, we find no obvious systematic differences in the stellar masses of galaxies with strong, high-EW emission lines, identified in the G102 and G141 spectra (Hα or [O III]; colored circles), as a result of using galaxy templates with or without emission lines in the SED-fitting procedure. Nonetheless, we release with this paper the best-fit SEDs computed with both `FAST` and `Synthesizer` to enable further investigations in specific subsets of emission-line galaxies. Because there are no obvious advantages to using either set of stellar-mass estimates, we choose the values computed with `FAST` as our fiducial stellar masses for the remainder of this work. This choice allows a more direct comparison to the stellar masses computed by the 3D-HST survey using the same fitting code and modeling assumptions (see below).

The left panel of Figure 19 shows the stellar-mass distribution for all galaxies in our catalog as a function of redshift using a gray-color intensity scale to indicate the

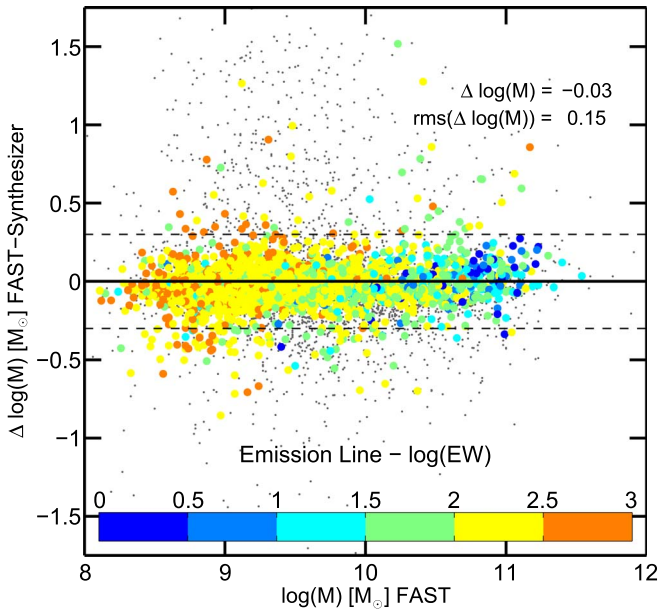

Figure 18. Comparison of the stellar masses computed using FAST and Synthesizer with the same modeling assumptions (see text). The primary difference between the galaxy models is that Synthesizer includes emission lines in the SEDs. The stellar-mass estimates are fully consistent. The overall distribution is centered around zero with a scatter of 0.15 dex. We find that no systematic affects the stellar masses of galaxies with strong emission lines, identified using the WFC3 grism spectra. The color code indicates the EW of the Hα and [O III] emission lines in those galaxies.

H-band magnitude of the galaxies. We use this diagram to study the mass completeness of the sample. The completeness of magnitude-limited samples, such as this one, decreases with redshift and is typically lower for red galaxies, either because they have intrinsically old stellar populations with larger mass-to-light ratios, or because the dust attenuation makes the galaxies fainter than unobscured SFGs of the same mass. Therefore, we characterize the mass completeness of the sample by estimating the mass threshold for the reddest galaxies with H-band magnitudes equal to the S/N $\sim$ 5 detection limit of the survey ($H \sim 26$). Red galaxies fainter than this threshold will be undetected at the depth of the survey. The orange and red lines show the mass-completeness limit for three galaxy templates of quiescent galaxies with ages ranging between 1 and 3 Gyr, i.e., the age of a recently quenched galaxy at any redshift, and the age of maximally old galaxies at $z = 2$–3. The purple line shows the detection limit for a young (250 Myr), dusty ($Av = 2$) SFG. In agreement with previous estimates of the mass completeness for the CANDELS catalogs in other fields (e.g., Tal et al. 2014; Nayyeri et al. 2017; Stefanon et al. 2017), we find that our catalog is complete to $\log(M/M_{\odot}) \gtrsim 10$ up to redshift $z \sim 3$ except perhaps for the most extreme dusty galaxies ($Av \gg 2$; see, e.g., Wang et al. 2016 for a study of dusty H-band drop outs). Interestingly, massive, recently quenched galaxies (also called post-starburst) can be reliably detected up to $z \sim 4$, as shown for example in Straatman et al. (2014).

We further verify the quality of the stellar-mass estimates by studying the comoving number density of massive ($\log(M/M_{\odot}) > 10$) star-forming and quiescent galaxies as a function of redshift. The right panel of Figure 19 shows that these number densities agree with the results from the UltraVISTA sample (Muzzin et al. 2013), which covers a larger area but to a shallower depth, at the same redshifts and follow the predicted trend at higher z. The CANDELS/GOODS-N sample is likely more susceptible to cosmic variance effects at the lowest redshift bin, but owing to its deeper limiting magnitude, it is possible to follow the evolution of both blue and red galaxies up to higher redshifts. Figure 20 shows one last quality check which compares our stellar-mass estimates versus those from 3D-HST catalog for the same galaxies. We find that the average offset and the scatter are in excellent agreement as reported in similar comparisons presented in previous CANDELS data papers for the four other fields.

5.4. UV+IR SFRs

5.4.1. The "Ladder" of SFR Indicators

In this section, we use the UV-to-FIR SEDs to provide SFR estimates for the galaxies in the sample. The depth of the optical/NIR photometry guarantees accurate measurements of the rest-frame UV emission ($\lambda \sim 1500$–2500 Å), which is an excellent tracer of the ongoing star formation, for all galaxies up to the highest redshifts. However, the ubiquitous presence of dust in SFGs, typically embedded in the same gas from which stars are formed, implies that the intrinsic UV emission of the galaxies is frequently attenuated by dust absorption. In galaxies with low-to-mid attenuations, it is possible to correct for the effect of dust absorption using different methods such as the slope of the UV emission, which is correlated with the Av (e.g., Meurer et al. 1997), or by estimating such Av from the optical-to-NIR SED fitting to stellar population models, which also provides a direct estimate of the intrinsic SFR. Nonetheless, several works have shown that the strong dust attenuations found in massive galaxies at $z \gtrsim 1.5$ can bias these corrections downwards, thus underestimating the SFRs (e.g., Daddi et al. 2007; Reddy et al. 2008, 2010; Wuyts et al. 2011a). The availability of FIR photometry provides a direct probe into the emission of the dust particles, responsible for the optical attenuation, which are being heated by the UV photons that reradiate this energy at longer wavelengths. Hence, the FIR photometry provides a useful SFR indicator for severely obscured galaxies, which make up a significant fraction of the massive galaxy population at high z. The main drawback of this method is that the shallower depth of the IR observations, compared to the optical and NIR data, limits the SFR detection threshold, which becomes increasingly higher with redshift and eventually leads to incompleteness even at the high-mass end (see, e.g., Figure 2 of Scoville et al. 2016).

A way forward to overcome the issues in both the UV- and IR-based SFR estimates is to combine the constraints coming from both methods by using a ladder of SFR indicators that can be cross-calibrated on relatively massive galaxies with intermediate dust attenuations and low IR fluxes. Here we follow such approach by using a method similar to the one described in Wuyts et al. (2011a). Briefly, the SFR ladder usually consists of three steps which differ on the amount of SFR indicators that are available for each galaxy, namely, UV, which is available for all galaxies; mid-IR, available only for a subset of massive galaxies ($\log(M/M_{\odot}) \gtrsim 10$) up to $z \sim 3$; and far-IR, available only for a subset of those mid-IR-detected galaxies.

The first step of the ladder is a UV-based SFR derived from the rest-frame UV luminosities of the galaxies. Owing to the breadth of optical and NIR photometric data, the rest-frame UV luminosity

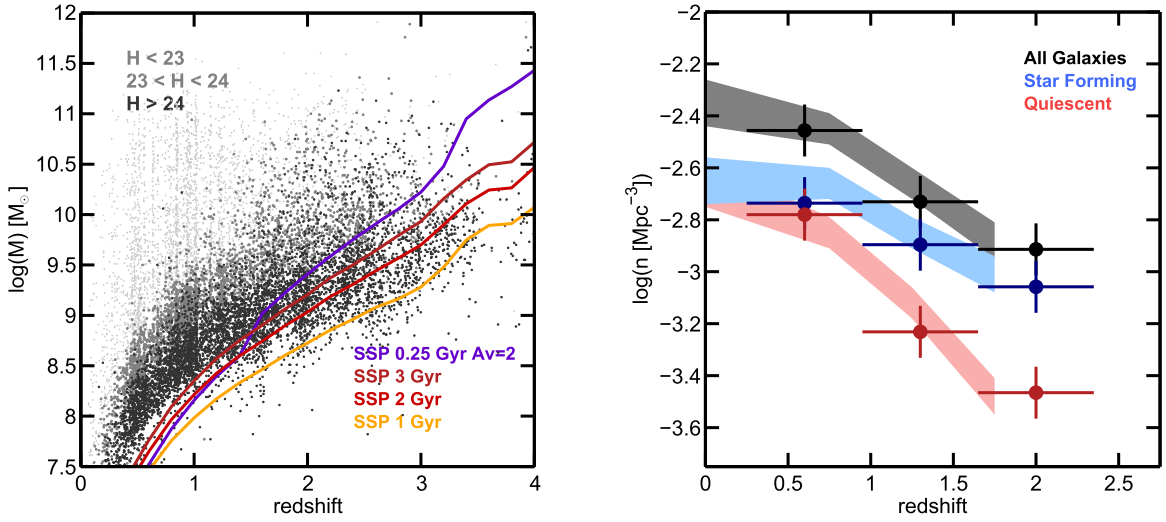

Figure 19. Left: galaxy stellar masses as a function of redshift for the CANDELS GOODS-N sample with a gray-color intensity scale for the *H*-band magnitude. We estimate the stellar-mass completeness of the sample by showing the stellar-mass threshold for a series of intrinsically red, quiescent, or dusty (orange, red, and purple lines) galaxy templates with an observed *H*-band magnitude equal to the S/N $\sim$ 5 detection limit of the catalog, $H \sim 26$. Right: comoving number density for galaxies more massive than $\log(M/M_{\odot}) > 10$ divided in three groups, star-forming (blue), quiescent (red), and both together (black), and compared to the results from the UltraVISTA COSMOS sample for the same range in stellar mass (shaded regions). The catalog provides results that are consistent with the literature (Muzzin et al. 2013), indicating that both our stellar masses and rest-frame colors are robust.

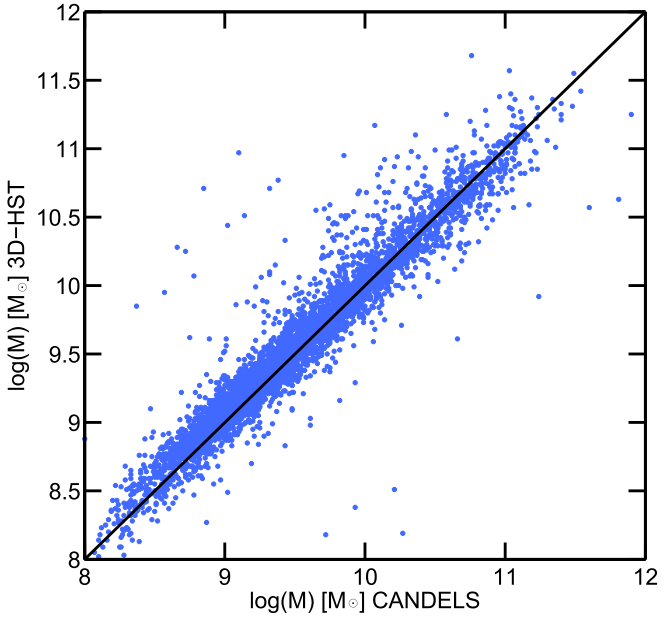

Figure 20. Stellar-mass comparison for the galaxies in the GOODS-N CANDELS and 3D-HST catalogs. Both sets of stellar masses are consistent with each other, showing almost negligible offsets, $\Delta\log(M/M_{\odot}) < 0.03$ dex, and a scatter of $\sim$0.3 dex, typical of the SED-fit-based stellar-mass estimates.

(i.e., the monochromatic luminosity at 280 nm) can be measured for galaxies at $z \gtrsim 0.3$. Thus, it provides a general, homogeneous SFR estimate for the whole sample. To compute the SFR from the UV luminosity, we use the relation of Kennicutt (1998), applying a correction for dust attenuation, $\mathrm{SFR_{TOT}}(M_{\odot}\ \mathrm{yr}^{-1}) = \mathrm{SFR_{UV}^{corr}} = 1.09 \times 10^{-10} \times 10^{0.4 * A_{\mathrm{UV}}}[3.3\, L_{\mathrm{UV}}(280)/L_{\odot}]$, where $L(280)$ and A_{UV} are the UV luminosity and dust attenuation at $\lambda = 280$ nm, respectively. The UV attenuation can be inferred directly from the the best-fit model to the overall SED, which assumes a Calzetti et al. (2000) attenuation law (i.e., $A_{\mathrm{UV}} = A(280) = 1.8Av$). However, rather than assuming these values, here we estimate A_{UV} on a galaxy-by-galaxy basis from the comparison of the slope of the UV continuum emission (β; $f_{\lambda} \propto \lambda^{\beta}$) to the ratio of UV to IR luminosities ($L(8\text{–}1000)/L_{\mathrm{UV}} \equiv$ IRX), or upper limits of the latter. The IRX–β diagram provides a useful diagnostic to characterize the dust attenuation in each galaxy (Meurer et al. 1997; Kong et al. 2004; Buat et al. 2007). This is particularly relevant to avoid overestimating the dust attenuation in blue, low-mass galaxies, undetected in the IR, for which the starburst, like the Calzetti et al. (2000) attenuation law, is not a good match. A more detailed description of this method is presented in Appendix D.

The second and third steps of the SFR ladder include only galaxies with mid-to-far-IR detections. For those galaxies, we use a hybrid estimate that combines UV and IR tracers. First, we estimate the contribution of the dust-obscured SFR by fitting the FIR SEDs with dust emission templates (see next section) and computing the integrated IR luminosity, from 8 to 1000 μm, $L(8-1000)$. Then, we obtain the total SFR by adding the contributions from the obscured (IR) and the observed, unobscured (UV) SFR, $\mathrm{SFR_{TOT}} = \mathrm{SFR_{IR}} + \mathrm{SFR_{UV}^{obs}}$ (e.g., Kennicutt 1998; Bell et al. 2005),

$$\mathrm{SFR_{TOT}} = 1.09 \times 10^{-10}[L(8-1000) + 3.3\, L_{\mathrm{UV}}(280)], \quad (1)$$

where the SFR is given in $M_{\odot}\ \mathrm{yr}^{-1}$, the luminosities are in $L_{\odot}$, and the conversion factor from luminosity to SFR assumes a Chabrier (2003) IMF.

5.4.2. Mid- and Far-IR-based SFR

For galaxies with IR detections, we distinguish between those with only mid-IR detections and those with both mid- and far-IR detections. As discussed in Section 2, our catalog includes photometry from both *Spitzer* and *Herschel*. The *Spitzer*/MIPS 24 μm photometry is deeper than *Herschel* PACS, and it has a higher spatial resolution than that of SPIRE. The downside of MIPS is that it probes shorter, mid-IR wavelengths, whereas the *Herschel* data spans a broader, FIR wavelength range from $\lambda = 100$ to 500 μm. Nonetheless, owing to its depth, a larger fraction of the sample is detected at 24 μm than in any *Herschel* band and thus provides SFR estimates for a large fraction of the massive galaxies up to

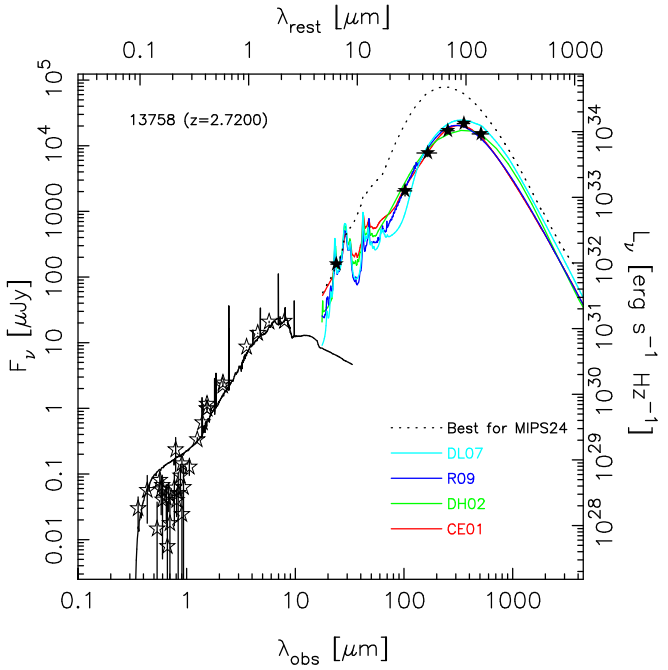

Figure 21. Example of a UV-to-FIR SED. The black line shows the best-fit BC03 stellar population model for the photometry up to 8 μm rest frame (open black stars), which provide an estimate of the stellar population properties and the dust attenuation. The filled black stars show the mid-to-far-IR data from *Spitzer* MIPS and *Herschel* PACS and SPIRE. The red, green, blue, and cyan lines show the best-fit dust emission models from the libraries of Chary & Elbaz (2001), Dale & Helou (2002), Rieke et al. (2009), and Draine & Li (2007), which provide similar results. The dashed line shows the fit to only the MIPS 24 μm data. The significant difference between this and the other templates illustrates why using an average-luminosity template, as in the Wuyts et al. (2011b) method, is a better approach for MIPS-only SEDs.

$z \sim 3$. For galaxies detected only in MIPS 24 μm, the modeling of the FIR emission with dust templates is uncertain, as it is only constrained by one point, and it is prone to overestimate the SFR at high z, due to a bias toward ULIRG templates for relatively normal galaxies (Daddi et al. 2007; Symeonidis et al. 2008; Kartaltepe et al. 2010; Barro et al. 2011; Elbaz et al. 2011). In order to avoid this problem, we use the analytic conversion from MIPS 24 μm fluxes to L(TIR) from Wuyts et al. (2008, 2011b), $\mathrm{SFR}_{\mathrm{IR}}^{\mathrm{W11}}$. This calibration uses only one template generated by averaging multiple dust emission templates and comparing to stacked *Spitzer* and *Herschel* photometry for multiple galaxies (see also Rieke et al. 2009 or Rujopakarn et al. 2013 for similar calibrations).

For galaxies with detections in multiple FIR photometric bands (e.g., galaxy SED in Figure 21), we fit the thermal IR emission (those bands redder than 5 μm in the rest frame, which are supposed to be dominated by dust emission) to the templates from the libraries of Chary & Elbaz (2001), Dale & Helou (2002), Rieke et al. (2009), and Draine & Li (2007). Then, we compute the integrated luminosity L(TIR) as the average value of the four sets. The typical differences in the predictions from the different models are roughly a factor of 2, consistent with the typical uncertainties in similar kinds of studies (Papovich et al. 2006; Daddi et al. 2007; Magnelli et al. 2009), $\mathrm{SFR}_{\mathrm{IR}}^{\mathrm{fit}}$. We also compute L(TIR) using the Wuyts et al. (2008) formula for these galaxies to have an additional estimate of the SFR that can be used to validate the accuracy of the IR SED fitting.

5.4.3. Comparison of the SFRs

Following Wuyts et al. (2011b), we cross-compare the different SFR estimates to validate their accuracy and consistency. Figure 22 shows the comparison between the total SFR based on the UV luminosity, corrected for extinction ($\mathrm{SFR}_{\mathrm{UV}}^{\mathrm{corr}}$; gray), and the total SFR determined from the fitting of all the far-IR data to dust emission templates ($\mathrm{SFR}_{\mathrm{IR}}^{\mathrm{fit}}+\mathrm{SFR}_{\mathrm{UV}}^{\mathrm{obs}}$; red) versus the total SFR based on the MIPS 24 μm fluxes and the Wuyts et al. (2011b) relation ($\mathrm{SFR}_{\mathrm{IR}}^{\mathrm{W11}} + \mathrm{SFR}_{\mathrm{UV}}^{\mathrm{obs}}$). The comparison to $\mathrm{SFR}_{\mathrm{UV}}^{\mathrm{corr}}$ is based on galaxies with relatively weak MIPS detections, $f(24\,\mu\mathrm{m}) > 20$–$150$ μJy, while the comparison to the IR SED-fitting SFRs includes all galaxies with at least one detection in a *Herschel* band. Overall, both comparisons are in qualitatively good agreement, showing that the SFR ladder method can be used to derive self-consistent SFRs across a wide range of galaxy masses and redshifts. The comparison to $\mathrm{SFR}_{\mathrm{UV}}^{\mathrm{corr}}$ shows a small offset and scatter, $\Delta\mathrm{SFR} \sim 0.03 \pm 0.32$ dex, that are consistent with the typical dispersion expected in this kind of comparison ($\sim$0.3 dex; e.g., Wuyts et al. 2011b). The comparison between the two IR-based SFRs shows a similar offset but a much smaller scatter ($\lesssim 0.02 \pm 0.17$ dex). The excellent agreement for the latter is not surprising, considering that the MIPS data are used in both SFR estimates, whereas the comparison to the UV-corrected SFRs is based on completely different tracers (UV versus IR).

We further analyze the consistency of the SFR ladder by comparing the locus of our SFR main sequence, i.e., the correlation between the SFR and stellar mass (e.g., Noeske et al. 2007; Elbaz et al. 2011; Whitaker et al. 2014), at different redshifts with previous results from the literature. Figure 23 shows how the combination of the different tiers of the SFR ladder (gray, orange, and red circles) reproduce the characteristic distribution of the SFR sequence, which exhibits a slope close to unity at lower masses and flattens toward the high-mass end (e.g., Speagle et al. 2014). The black and gray lines show the running median and 1σ scatter of the distribution for SFGs selected using the *UVJ* diagram (see Figure 17). The overall distribution exhibits a good agreement with the results of Whitaker et al. (2014; blue line) and Schreiber et al. (2015a; green line), also based on far-IR photometry, and shows a similar curvature as a function of mass. We further discuss the properties of the SFR main sequence derived from our SFR estimates in Appendix D, which also expands the analysis to include data from the five CANDELS fields.

6. Summary

In this paper, we present an *HST*/WFC3 F160W (*H*-band) selected sample in the CANDELS/GOODS-N field characterized with UV-to-FIR SEDs. The sources are selected from an F160W mosaic which combines data from the deep and wide observations of the CANDELS program over a total area of 171 arcmin^2. The photometric catalog includes the newly observed *HST* data in F105W, F125W, and F160W, taken as part of the CANDELS survey, with all the previous *HST* optical observations in ACS F435W, F606W, F775W, F814W, and F850LP from GOODS and other smaller programs. In addition to the *HST* data, we include deep photometric data in 25 optical medium-band filters from the SHARDS survey (Pérez-González et al. 2013), which constitutes one of the deepest (i-band $\sim$28 mag) and highest resolution ($R \sim 50$) medium-band surveys, surpassing the depth, spectral coverage, and resolution of similar medium-band observations in other deep fields such as COSMOS or GOODS-S. Furthermore,

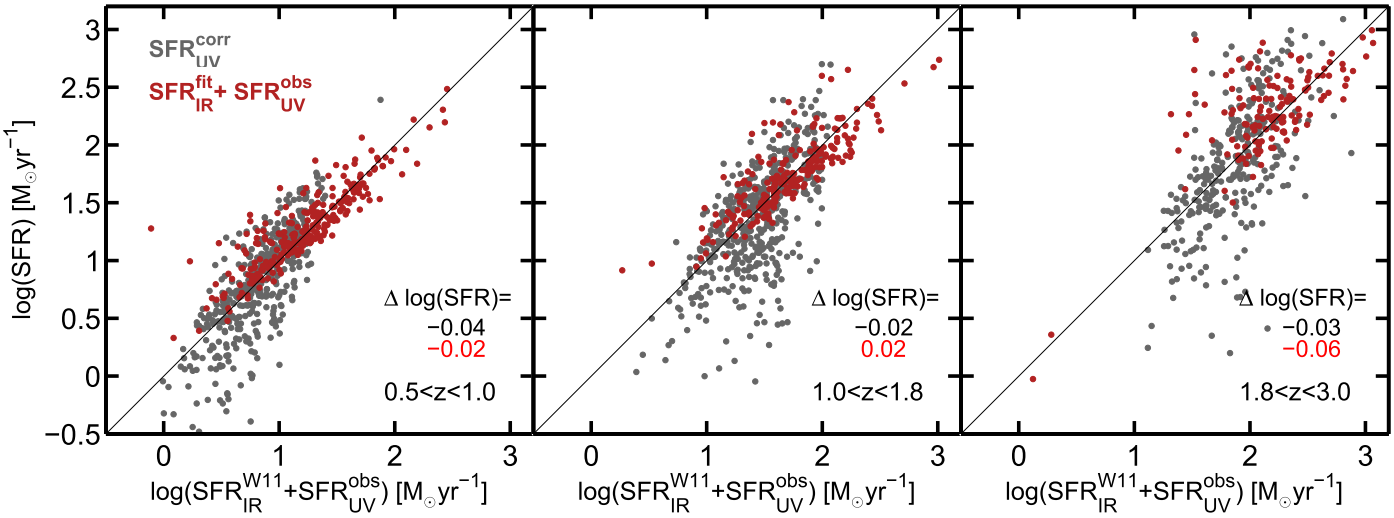

Figure 22. Comparison between different total SFR indicators at different redshifts. The *x*-axis show the SFRs derived from the combination of the observed (unobscured) UV SFR$_{UV}^{obs}$ and the IR-based SFR determined from the MIPS 24 μm flux using the prescription of Wuyts et al. (2011b), SFR$_{IR}^{W11}$. They *y*-axis shows the total SFR derived either from the UV luminosity, corrected for extinction (SFR$_{UV}^{corr}$; gray circles), or the combination of SFR$_{UV}^{obs}$ and the IR-based SFRs computed from the fit of all available FIR data to dust emission templates (red circles). The median difference between SFR estimates, Δlog SFR, is indicated for the UV-corrected (black) and IR-based (red) SFRs. Overall, the two different estimates exhibit good agreement, showing that is it possible to combine them in an SFR ladder that spans a range of more than 2 dex in SFRs.

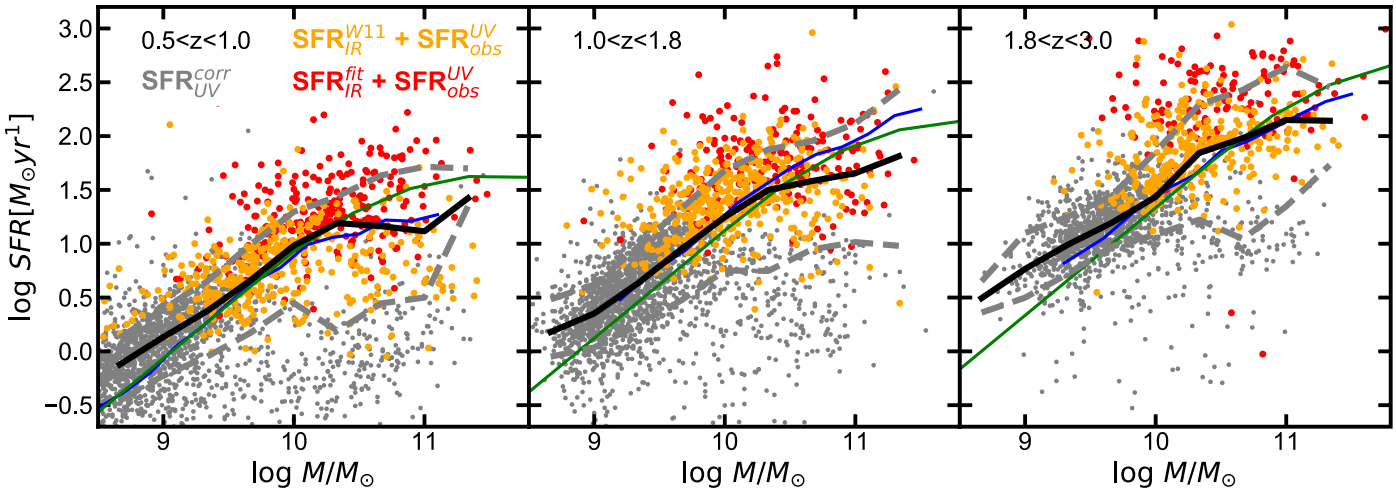

Figure 23. SFR vs. stellar-mass diagram (i.e., the SFR sequence; Noeske et al. 2007) as a function of redshift compared to results from the literature. The SFRs in the *y*-axis are computed by combining the different SFR indicators in Figure 22 (gray, orange, and red circles) to assemble the SFR ladder. The black and gray lines show the running median and 1σ scatter of the SFGs identified with the *UVJ* criterion. The blue and green lines show the SFR sequences from Whitaker et al. (2014) and Schreiber et al. (2015a), which are roughly consistent with the overall distributions at all redshifts.

we include ancillary data in the ultraviolet, LBC/*U* and KPNO/*U*′; near-IR, MOIRCS/*K*, CFHT/*K*′, and *Spitzer*/IRAC 3.6, 4.5, 5.8, and 8.0 μm; and a wealth of far-IR photometry at 24 μm, and 70 μm from *Spitzer* MIPS and at 100, 160, 250, 350, and 500 μm, from *Herschel* PACS and SPIRE. In addition, we complement and expand the broad- and medium-band photometry with WFC3/IR grism spectroscopy in G102 from new observations (GO:13179), and in G141 from AGHAST (GO:11600), as reduced by 3D-HST (Momcheva et al. 2016). The combined grism observations make GOODS-N the first among the deep cosmological fields to have similar areal coverage in the contiguous grisms, which enables a simultaneous analysis of several emission lines at different redshifts.

As in previous CANDELS papers, the source detection is based on a slightly modified version of SExtractor, which runs and combines the output of two configurations (cold and hot) to optimally detect and extract all sources ranging from the largest, most extended, and brightest ones to the faintest and smallest. Similarly, we use TFIT to measure uniform multiband photometry in the lower resolution optical-to-NIR bands. TFIT uses priors from the positions of the F160W detections to construct object templates that are PSF-matched and fitted to the low-resolution images to measure the photometry. The FIR photometry is measured independently and self-consistently on the *Spitzer* and *Herschel* images using MIPS 24 μm priors. Then, each IR source is assigned a single F160W counterpart based on coordinates and IRAC fluxes. The F160W-selected catalog contains >35,000 sources down to a 5σ limiting depth of $H = 27.4$ and 28.2 mag in the wide and deep regions of the mosaic, respectively.

We show that the overall SEDs present the level of consistency required to characterize the intrinsic stellar populations of the galaxy, and we perform a galaxy-by-galaxy fitting of

the UV-to-FIR SEDs to stellar population and dust emission models and a fit of their grism spectra for emission and absorption lines. From the best-fitting optical and IR templates, we estimate the (1) photometric redshifts, (2) stellar population properties (i.e., stellar masses, *Av*, etc.), and (3) SFRs. From the line fitting of the G102 and G141 *HST* grism data, we estimate the line fluxes and EWs. Then, we analyze the accuracy and reliability of these estimates with respect to different parameters. A summary of the most important results of this analysis follows.

1. The use of medium-band photometry and grism spectroscopy significantly improves the quality of the photometric redshifts relative to the case of SED fitting to broadband photometry only. The comparison to 1485 spectroscopic redshifts up to $z \sim 3$ yields $\sigma_{\rm NCMAD} = 0.0032$ and an outlier fraction of $\eta = 4.3\%$, nearly a factor of 7 more precise than the typical, broadband-based redshifts.
2. Owing to the deep limiting magnitude of the F160W mosaic, our catalog is nearly complete for stellar masses above $\log(M/M_{\odot}) = 10$ up to redshift $z \sim 3$, except perhaps for the most extreme dusty galaxies ($Av \gg 2$).
3. The line catalog contains nearly 2000 emission lines detected at $S/N > 3$, with 30% and 70% of them identified in the G102 and G141 spectra, respectively. The G102 detections are typically in brighter and lower redshift galaxies, $H < 23.5$ and $\bar{z} = 0.7$, while the G141 detections are in fainter and higher redshift galaxies, $H < 24.5$ and $\bar{z} = 1.5$. For magnitudes $H < 23.5$, roughly 35% of all galaxies have two emission lines detected, typically Hα(G141) and Hβ(G102) at $z = 0.6$–1.3.
4. We obtain robust SFRs for all galaxies in the catalog by using in each case the best available SFR tracer from either the rest-frame UV or the far-IR emission. The overall SFR ladder is computed self-consistently by verifying the consistency in the SFRs for galaxies with multiple indicators and showing that the resulting SFR main sequence is in good agreement with previous works at all redshifts over a range of 2 dex in stellar mass.

The multiband photometry and the value-added catalogs (see appendices) presented in this paper are further complemented with additional data products from the CANDELS survey, which allow even richer studies of the galaxy populations by adding, for example, structural properties (van der Wel et al. 2014) or visual morphologies (Huertas-Company et al. 2015), enabling a wide array of additional science in one of the premier cosmological fields.

Support for program number HST-GO-12060 was provided by NASA through a grant from the Space Telescope Science Institute, which is operated by the Association of Universities for Research in Astronomy, Inc., under NASA contract NAS5-26555. G.B., S.M.F, and D.K. acknowledge support from HST-GO-13420 and NSF grants AST-0808133 and AST-1615730. P.G.P.-G. acknowledges support from grant AYA2015-63650-P. This work has made use of the Rainbow Cosmological Surveys Database, which is operated by the Centro de Astrobiología (CAB/INTA), partnered with the University of California Observatories at Santa Cruz (UCO/Lick, UCSC). This work is based in part on observations made with the *Spitzer Space Telescope*, which is operated by the Jet Propulsion Laboratory, California Institute of Technology under a contract with NASA. Support for this work was provided by NASA.

Appendix A
Photometric Catalogs

This appendix features CANDELS GOODS-N multiband photometric catalog entries with optical observations from KPNO, LBC, *HST*/ACS, near-infrared data from *HST*/ WFC3, CFHT, and Subaru, and infrared observations from *Spitzer*/ IRAC (Table 4). This catalog also contains useful SExtractor outputs for the *HST* bands as the catalogs were released with the previous CANDELS papers.

A separate catalog containing the photometry in the 25 medium bands of the SHARDS survey is also provided (see Table 5). The medium-band photometry is shown separately to explicitly indicate the variation in the central wavelength of each passband (see Table 6), due to the location of the sources in the SHARDS mosaic (see Section 2.2.2 and Pérez-González et al. 2013 for more details).

Table 4
Description of the CANDELS GOODS-N Photometric Catalog

Column No.	Column Title	Description
1	ID	Object identifier, beginning from 1
2	IAU Name	
3, 4	R.A., decl.	Right ascension and declination (J2000.0; decimal degrees)
5	FLAGS	SExtractor F160W flag used to designate suspicious sources that fall in contaminated regions
6	CLASS_STAR	SExtractor CLASS_STAR parameter in the F160W band
7	X-ray	X-ray ID from Alexander et al. (2003)
8–41	Flux, Flux_Err	Flux and flux in each filter. Sources that are not observed have (−99.00, −99.00, 0). Filters are included in order KPNO_U, LBC_U, F435W, F606W, F775W, F814W, F850LP, F105W, F125W, F160W, MOIRCS_Ks, CFHT_Ks, 3.6 μm, 4.5 μm, 5.8 μm, and 8.0 μm
1	ID	Object identifier, beginning from 1
2–10	FLUX_MAX	in *HST* bands
11–28	FLUX_ISO, FLUXERR_ISO	Isophotal flux and flux error in nine *HST* bands
29–46	FLUX_ISOCOR, FLUXERR_ISOCOR	Isophotal flux and flux error in nine *HST* bands
47–64	FLUX_AUTO, FLUXERR_AUTO	AUTO flux and flux error in nine *HST* bands
65–82	FLUX_PETRO, FLUXERR_PETRO	PETRO flux and flux error in nine *HST* bands
83–100	FLUX_BEST, FLUXERR_BEST	BEST flux and flux error in nine *HST* bands

Table 4
(Continued)

Column No.	Column Title	Description
101–280	FLUX_APER, FLUXERR_APER	APER flux and flux error in nine *HST* bands and 10 circular apertures of radius 1.47, 2.08, 2.94, 4.17, 5.88, 8.34, 11.79, 16.66, 23.57, 33.34, 47.13
1	ID	Object identifier, beginning from 1
2	X_IMAGE	Object position along x [pixel]
3	Y_IMAGE	Object position along y [pixel]
4	XPEAK_IMAGE	x coordinate of the brightest pixel [pixel]
5	YPEAK_IMAGE	y coordinate of the brightest pixel [pixel]
6	XMIN_IMAGE	Minimum x coordinate among detected pixels [pixel]
7	YMIN_IMAGE	Minimum y coordinate among detected pixels [pixel]
8	XMAX_IMAGE	Maximum x coordinate among detected pixels [pixel]
9	YMAX_IMAGE	Maximum y coordinate among detected pixels [pixel]
10	X2_IMAGE	Variance along x [pixel**2]
11	Y2_IMAGE	Variance along y [pixel**2]
12	XY_IMAGE	Covariance between x and y [pixel**2]
13	CXX_IMAGE	Cxx object ellipse parameter [pixel**(-2)]
14	CYY_IMAGE	Cyy object ellipse parameter [pixel**(-2)]
15	CXY_IMAGE	Cxy object ellipse parameter [pixel**(-2)]
16, 17	A_IMAGE, B_IMAGE	F160W profile rms along major and minor axes (pixel)
18, 19	ERRA_IMAGE, ERRB_IMAGE	F160W profile rms along major and minor axes (pixel)
20, 21	THETA_IMAGE, ERRTHETA_IMAGE	F160W position angle (degree)
22	ISOAREAF_IMAGE	SExtractor F160W isophotal area (filtered) above detection threshold (pixel^2)
23–31	ISOAREA_IMAGE	SExtractor isophotal area (filtered) above detection threshold (pixel^2) in *HST* bands
32–40	BACKGROUND	Background at centroid position in *HST* bands
41–49	FLUX_RADIUS_1	RADIUS_1 with the 0.2 fraction of light in *HST* bands
50–58	FLUX_RADIUS_2	RADIUS_2 with the 0.5 fraction of light in *HST* bands
59–67	FLUX_RADIUS_3	RADIUS_3 with the 0.8 fraction of light in *HST* bands
68–76	FWHM_IMAGE	FWHM of the image of an object, in units of pixel (1 pixel = 0.″06) in *HST* bands
77	KRON_RADIUS	F160W band Kron radius from SExtractor (in unit of A_IMAGE or B_IMAGE)
78	PETRO_RADIUS	F160W band Petrosian radius from SExtractor (in unit of A_IMAGE or B_IMAGE)

Table 5
Description of the SHARDS Photometry for the CANDELS Catalog

Column No.	Column Title	Description
1	ID	Object identifier, beginning from 1
2–76	Flux, Flux_Err, Eff_wav	Flux, flux error, and central effective wavelength (CWL) in each of the 25 SHARDS filters. Values of Flux $>$ 0 with Flux_Err = 0 indicate upper limits for non-detected sources. Values of Flux = 0 and Flux_Err = 0 indicate that the source is not observed. The CWL is a function of the position of the object in the SHARDS mosaic (see Section 2.2.2)

Table 6
Nominal Central Wavelengths of the SHARDS Filter Set

Filter	CWL (nm)	Width (nm)
F500W17	500.0	15.0
F517W17	517.0	16.5
F534W17	534.0	17.7
F551W17	551.0	13.8
F568W17	568.0	14.4
F585W17	585.0	15.1
F602W17	602.0	15.5
F619W17	619.0	15.8
F636W17	638.4	15.4
F653W17	653.1	14.8
F670W17	668.4	15.3
F687W17	688.2	15.3
F704W17	704.5	17.1
F721W17	720.2	18.2

Table 6
(Continued)

Filter	CWL (nm)	Width (nm)
F738W17	737.8	15.0
F755W17	754.5	14.8
F772W17	770.9	15.4
F789W17	789.0	15.5
F806W17	805.6	15.6
F823W17	825.4	14.7
F840W17	840.0	15.4
F857W17	856.4	15.8
F883W35	880.3	31.7
F913W25	913.0	27.8
F941W33	941.0	33.3

Note. https://guaix.fis.ucm.es/~pgperez/SHARDS/Filters

Appendix B
Optical/NIR SED-fitting-based Catalogs: Photometric Redshifts and Stellar Properties

This appendix describes the content of the tables with the photometric redshifts and stellar properties for all of the objects in the catalog derived from the fitting of their SEDs. The redshifts given in Table 7 are the best-effort redshift estimates based either on good-quality spectroscopic redshift or on the three-tier photometric redshift method, i.e., computed either with broadband data, broadband and SHARDS medium-band data, or broad- and medium-band data plus WFC3 grism.

The redshifts given in Table 8 are the supplementary photometric redshift estimates computed by five different investigators using only broadband data. For these particular estimates, homogeneity in the input photometric data was preferred over quality of the photo-z. The latter can be improved by adding higher spectral resolution data (as in the three-tier method), but such data are only available for smaller subsets of the whole sample. The codes and assumptions used by each different investigator are the following: Finkelstein, using `EAZY` based on the standard templates with emission lines plus an additional high-z galaxy template (BX14 from Erb et al. 2010); Salvato, using `Lephare` (Arnouts & Ilbert 2011) based on BC03+Polleta AGN templates without emission lines; Fontana, using `zphot` (Fontana et al. 2000) based on BC03 templates with emission lines; Wuyts, using `EAZY` based on the standard templates with emission lines; and Wiklind, using `WikZ` from Wiklind et al. (2008) based on BC03 templates without emission lines.

Table 9 describes the content of the catalog with the stellar population properties computed with `FAST` and the rest-frame absolute magnitudes derived with `EAZY`. Table 10 describes the content of the catalog with the stellar population properties computed with `Synthesizer`.

Table 7
Description of the Photometric Redshift Catalog

Column No.	Column Name	Description
1	id	Object identifier
2	zspec	Spectroscopic redshift
3	zpecflag	Spectroscopic redshift quality flag (1—most reliable, 2—reliable, 3—unreliable)
4	zref	Original reference for the spectroscopic redshift
5	ztier	Best photometric redshift from the three-tiered estimate
6	ztier_err	Uncertainty in ztier computed from the 68% confidence region of the PDFz
7	ztier_class	Classification of ztier: 1—Broadband only, 2—Broadband and SHARDS, 3—Broadband, SHARDS, and WFC3 grism
8	zbest	Best redshift estimate from zspec, if available and with flag <3, or ztier

Table 8
Description of the Supplementary Photo-z from Different Investigators

Column No.	Column ID.
1	id
2	zphot_finkelstein
3	zphot_finkelstein_inf68
4	zphot_finkelstein_sup68
5	zphot_salvato
6	zphot_salvato_inf68
7	zphot_salvato_sup68
8	zphot_fontana
9	zphot_fontana_inf68
10	zphot_fontana_sup68
11	zphot_wuyts
12	zphot_wuyts_inf68
13	zphot_wuyts_sup68
14	zphot_wiklind
15	zphot_wiklind_inf68
16	zphot_wiklind_sup68

Table 9
Stellar Population Properties Catalog from FAST

Column No.	Column ID.	Description
1	id	Object identifier
2	z	=zbest from Table 7
3	ltau	log[tau/yr]
4	metal	metallicity (fixed to 0.020)
5	lage	log[age/yr]
6	Av	dust reddening
7	lmass	$\log[M/M_{\odot}]$
8	lsfr	$\log[\mathrm{SFR}/(M_{\odot}/\mathrm{yr})]$
9	lssfr	log[sSFR(/yr)]
10	la2t	$\log[\mathrm{age}/\tau]$
11	chi2	minimum χ^2
12	M_U	abs. magnitude in Johnson U
13	M_V	abs. magnitude in Johnson V
14	M_J	abs. magnitude in 2MASS J

Table 10
Stellar Population Properties from `Synthesizer`

Column No.	Column ID.	Description
1	id	Object identifier
2	z	=zbest from Table 7
3	ltau	log[tau/yr]
4	metal	metallicity (fixed to 0.020)
5	lage	log[age/yr]
6	Av	dust reddening
7	lmass	$\log[M/M_{\odot}]$

Table 11
Emission-line Catalog Based on the G102 and G141 Spectra

Column name	Description
id	Object identifier
z	Grism redshift used in the emission-line fit, identical to `ztier` in the redshift catalog
X_FLUX	Emission-line flux in units of 10^{-17} ergs s^{-1} cm^{-2}
X_ERR	Error in the emission-line flux in units of 10^{-17} ergs s^{-1} cm^{-2}
X_SCALE	Multiplicative scaling factor to correct the flux of the emission line to the photometry
X_EQW	Emission-line equivalent width in Å

Note. X = emission-line name, as given in the accompanying table.

Table 12
Emission Lines

Line	Catalog ID	Rest Wavelength (Å)	Ratio
Lyα	Lya	1215.400	···
C IV	C IV	1549.480	···
Mg II	Mg II	2799.117	···
Ne V	Ne V	3346.800	···
Ne VI	Ne VI	3426.850	···
[O II]	O II	3729.875	···
[Ne III]	Ne III	3869.000	···
He I	He Ib	3889.500	···
Hδ	Hd	4102.892	···
Hγ	Hg	4341.680	···
[O III]	O IIIx	4364.436	···
He II	He II	4687.500	···
Hβ	Hb	4862.680	···
[O III]	O III	5008.240, 4960.295	2.98:1
He I	He I	5877.200	···
[O I]	O I	6302.046	···
Hα	Ha	6564.610	···
[S II]	S II	6718.290, 6732.670	1:1
S III	S III	9068.600, 9530.600	1:2.44

Appendix C
WFC3 Grism Spectroscopy: Line Catalogs

This appendix describes the content of the WFC3 grism line catalogs derived from the G102 and G141 spectra. As discussed in Section 5.2, the line fluxes and EWs presented in Table 11 are measured using the same code introduced by the 3D-HST survey (Momcheva et al. 2016). This code fits the spectra to Gaussian line templates, normalized to the total broadband photometry, using an MCMC method. The names and nominal wavelengths of the lines are given in Table 12 (also Table 4 from Momcheva et al. 2016).

Appendix D
Self-consistent Far-IR Photometry and SFRs for Galaxies in the Five CANDELS Catalogs

The first section of this appendix describes in detail the method to measure mid-to-far-IR photometry and how to assign those fluxes to the most likely counterparts in the F160W-selected CANDELS catalogs in five fields, namely UDS (Galametz et al. 2013), GOODS-S (Guo et al. 2013), EGS (Stefanon et al. 2017), COSMOS (Nayyeri et al. 2017), and GOODS-N (this paper). Then, we review the procedure to compute self-consistent SFRs for all galaxies in the catalog using the SFR ladder method, which is based on a combination of UV and IR SFR tracers. This method is also described in Section 5.4. Here we provide additional details on the procedure to estimate the UV dust attenuation from the slope of the UV SED (β) and the ratio between the observed UV and IR luminosities (IRX). Next, we assess the quality of the IR photometry and SFRs by comparing our estimates to those from other works in the literature. Lastly, we describe the content of the tables presenting the IR fluxes, dust attenuations and SFRs for all galaxies, and the quality flag tables for the IR photometry, which are aimed to help diagnose potentially problematic sources.

D.1. Mid-to-far-IR Catalogs and Matching to F160W Sources

We build merged, mid-to-far-IR photometric catalogs using *Spitzer*/IRAC and MIPS, and *Herschel*/PACS and SPIRE data sets presented in Pérez-González et al. (2005, 2008, 2010), PEP + GOODS-*Herschel* (Lutz et al. 2011; Magnelli et al. 2013), and HerMES (Oliver et al. 2012). Table 13 summarizes the 5σ limiting fluxes in each band and field. The method to extract IR sources from the MIPS, PACS, and SPIRE mosaics and to measure their photometry is described in detail in Pérez-González et al. (2010 see also Rawle et al. 2016 and Rodríguez-Muñoz et al. 2019). Briefly, the method consists of three steps: (1) source identification in each of the individual IR bands by using a combination of priors and direct detections, (2) photometric measurements based on PSF fitting, and (3) merging of the individual photometric catalogs to produce multiband MIPS, PACS, and SPIRE catalogs.

D.1.1. Mid-to-far-IR Photometric Measurements

Given the overall higher sensitivity and spatial resolution of MIPS24, the source identification in this band is based on direct detections (i.e., without IRAC priors). For the lower resolution and lower sensitivity PACS and SPIRE bands, we use a combination of IRAC and MIPS priors to reduce the effects of confusion. For these priors, we use IRAC-selected catalogs drawn from *Spitzer*/IRAC mosaics (see Pérez-González et al. 2008), i.e., not the TFIT-deblended sources based on F160W described in Section 3.2. Before extracting sources in PACS and SPIRE, we remove from the prior catalog those sources that are too close to be spatially resolved in each of those bands. Then, the prior-based idenfications are complemented with direct detections identified by running the source detection iteratively at different detection levels, starting from bright to faint sources. This approach improves the detection of faint sources located close to very bright sources (Pérez-González et al. 2005).

The source detection catalog in each of the IR bands is used to measure the photometry by fitting PSFs at the given positions using the daophot package in `IRAF`, and allowing for one pixel centering offsets. The PSF models for each band are created using bright, well-detected sources. The tailored PSFs allow us to account for data reduction effects such as drizzling and a repixelization of the original images. The total fluxes are estimated from the flux densities measured in optimum circular apertures and applying aperture corrections (see Section 2 of Pérez-González et al. 2010 for more details). To ensure the robustness of the photometric measurement, all sources

Table 13
Limiting Fluxes (5σ) of the *Spitzer* and *Herschel* Photometry Used in This Work

	$\mathcal{F}_{\rm lim}$ (μJy)		$\mathcal{F}_{\rm lim}$ (mJy)				
	Spitzer/MIPS		*Herschel*/PACS		*Herschel*/SPIRE		
Field	24 μm	70 μm	100 μm	160 μm	250 μm	350 μm	500 μm
(1)	(2)	(3)	(4)	(5)	(6)	(7)	(8)
GOODS-N	30	2500	1.6	3.6	9.0	12.9	12.6
GOODS-S	30	2500	1.1	3.4	8.3	11.5	11.3
EGS	45	3500	8.7	13.1	14.7	17.3	17.9
COSMOS	70	⋯	2.9	6.6	11.0	9.6	11.2
UDS	70	⋯	14.4	26.7	19.4	19.2	20.0

detected below the 3σ detection limit of each band (see Table 13) are removed from the single-band catalogs.

Lastly, all of the single-band catalogs are unified into three merged catalogs for MIPS (24 and 70), PACS (100-to-160), and SPIRE (250-to-500), respectively, which will then be used to assign IR fluxes to the sources in the CANDELS/F160W catalog. We note that there is little ambiguity in assigning MIPS24 counterparts to the PACS100 detections. In fact, 95% of the PACS100 sources have a single possible MIPS24 counterpart, and the remaining 5% have only two. Similarly, PACS160 has a lower spatial resolution, but also a lower sensitivity (i.e., fewer detections). This means we can assign reliable PACS100 counterparts for all PACS160 sources and from there tie them to MIPS. For the SPIRE bands, we find that each SPIRE350 and SPIRE500 source can be identified with a single counterpart in the deeper and higher resolution SPIRE250 band. Nonetheless, the multiplicity of the SPIRE250 sources in bluer bands (down to IRAC) is equal to or larger than 2 for 85% of the sources.

D.1.2. Matching IR Fluxes to F160W Sources

Based on the IR-only catalogs described above, we assign mid-to-far-IR fluxes to the CANDELS sources following the method described in Rodríguez-Muñoz et al. (2019) to identify the most likely F160W counterpart for each mid- and far-IR source. Briefly, we use a cross-matching procedure based on the celestial coordinates, which runs in three steps: first identifying F160W counterparts to MIPS sources within $2\farcs5$, then MIPS counterparts to PACS sources within $3\farcs0$, and finally PACS counterparts to SPIRE sources within $9\farcs0$. Before the cross-match, we set $S/N > 3$ lower limits for the IR fluxes below which the sources are excluded from the rest of the analysis.

If the multiplicity of the F160W to MIPS match is larger than 1, the primary counterpart is determined by assigning the highest priority to the F160W source with the highest flux in the reddest IRAC band, typically 8.0 μm, but sometimes 3.6/4.5 μm for faint IRAC sources. If multiple counterparts have similar IRAC fluxes within 1σ, the primary is the one closest in distance to the MIPS source. For the MIPS to PACS, and PACS to SPIRE identifications, the primary counterpart is determined again by prioritizing the brightness in the reddest available band, e.g., the primary counterparts to a PACS160 (SPIRE250) source is the brightest MIPS24 (PACS160) neighbor. In the few cases where a PACS source has no MIPS counterparts, we cross-match directly to F160W, and we assign the primary counterpart based on the IRAC fluxes determined with `TFIT`.

After this sequential process, only the primary counterpart in each cross-match is used in the following step. As a result, each mid-to-far-IR detection has a unique F160W counterpart in the final catalog. Only those F160W sources with IR detections are used in the next section to compute IR-based SFR estimates. Nonetheless, this paper provides supplementary IR catalogs (see Appendix D.4), which indicate all of the secondary short-wavelength counterparts in all bands involved in the cross-matching procedure. These catalogs also indicate the multiplicity, i.e., the total number of counterparts to each long-wavelength source, which can be used for further diagnostics.

D.2. SFRs and Dust Attenuations from the SFR Ladder Method

In the following, we describe our method to obtain SFRs for all galaxies in the CANDELS catalogs. Our empirical approach is based on an auto-consistent combination of three tracers: the ultraviolet, the mid-, and the far-infrared emission. With them, we analyze the extinction properties of the CANDELS *H*-band-selected galaxies in order to provide a robust estimation of the SFR on a galaxy-by-galaxy basis, taking into account both the evolving intrinsic properties of galaxies as well as the limitations of the data currently available in the CANDELS fields (in the relevant wavelengths). Several tests have been carried out to check the consistency of the different estimations. We describe the method and tests in detail in the following paragraphs.

For each galaxy in our sample, we aim to estimating its SFR taking into account both the direct emission from young stars as well as from stars obscured by interstellar dust. With this in mind, the total SFR of a galaxy, $\mathrm{SFR_{TOT}}$, can be calculated in two different ways:

adding $\mathrm{SFR_{UV}^{obs}}$, the SFR linked to unobscured stars (provided by the observed total UV emission), to $\mathrm{SFR_{IR}}$, the SFR associated with the emission from young stars which is absorbed by dust and reradiated in the IR:

$$\mathrm{SFR_{TOT}} = \mathrm{SFR_{UV}^{obs}} + \mathrm{SFR_{IR}}; \quad (2)$$

using the observed total UV emission, $\mathrm{SFR_{UV}^{obs}}$, and applying an attenuation correction to obtain the total SFR:

$$\mathrm{SFR_{TOT}} = \mathrm{SFR_{UV}^{corr}} = 10^{0.4A_{\rm UV}}\,\mathrm{SFR_{UV}^{obs}}. \quad (3)$$

We note that joining the previous two equations, we can obtain an expression of the attenuation in terms of the SFRs:

$$A_{\rm UV} = 2.5\log(\mathrm{SFR_{IR}}/\mathrm{SFR_{UV}^{obs}} + 1). \quad (4)$$

Concerning the first method, the observed UV-based SFR is typically estimated from monochromatic luminosities after

applying a bolometric correction to obtain the emission at all UV wavelengths. In this work, we consider SFR_{UV}^{obs} estimations based on the luminosity at 160 and 280 nm rest frame, transformed into a bolometric UV emission and an SFR following the calibrations found in Kennicutt (1998) and Bell et al. (2005), respectively. For the first transformation, we correct the original factor calculated for a Salpeter (1955) IMF to a Chabrier (2003) IMF, dividing by a 1.6 factor. The UV-to-SFR calibrations are

$$SFR_{UV}^{obs} = 8.8 \times 10^{-29}\, L_{\nu}(160) \quad (5)$$

$$SFR_{UV}^{obs} = 1.0 \times 10^{-28}\, L_{\nu}(280). \quad (6)$$

In both equations, the SFRs are given in $M_{\odot}\,yr^{-1}$ and the luminosity densities in $erg\,s^{-1}\,Hz^{-1}$.

Concerning the IR-based SFR, SFR_{IR}, we estimate it in two different ways. For galaxies that are detected (at least at a 5σ level) by the *Spitzer* MIPS instrument at 24 μm and by one or several *Herschel* bands with the PACS and/or SPIRE instruments, we fit the flux points to dust emission models. We use the libraries published by Chary & Elbaz (2001), Dale & Helou (2002), Rieke et al. (2009), and Draine & Li (2007), and calculate the total IR luminosity, integrating the best-fitting model for each library from 8 to 1000 μm to obtain $L(8-1000)$. The typical scatter in $L(8-1000)$ for the different template sets is 0.05 dex. This bolometric IR luminosity is transformed into an SFR using the calibration in Kennicutt (1998), assuming a Chabrier (2003) IMF,

$$SFR_{IR}^{fit} = 2.8 \times 10^{-44}\, L(8 - 1000), \quad (7)$$

where $L(8-1000)$ is given in $erg\,s^{-1}$ and the SFR in $M_{\odot}\,yr^{-1}$.

For galaxies that are only detected by MIPS at 24 μm, the calculation of $L(8-1000)$ involves an extrapolation that is larger, more uncertain, and affected by significant systematic errors as we move to higher redshifts (see, e.g., Papovich et al. 2007). Consequently, for these galaxies, we used the transformations between the 24 μm emission and SFR presented in Wuyts et al. (2011a, W11), SFR_{IR}^{W11}, who tested them against *Herschel*-based SFRs (see also the discussion in the next paragraph). We also considered the transformations from MIPS 24 μm to SFR proposed in Rujopakarn et al. (2013, R13), but decided to use Wuyts et al.'s recipe based on its better performance (see below).

In order to test the reliability of the SFRs obtained from the 24 μm flux point alone, we compared them with the SFRs obtained from the fits to dust emission models for the galaxies with *Herschel* detections. The results for GOODS-N are presented in Figure 22 in the main text. In Figure 24, we plot the comparison for the five CANDELS fields. The typical systematic offset between the two SFR estimations is always below 0.05 dex, except at $z > 3$, and the scatter is 0.2–0.3 dex. For comparison, the results obtained when comparing the R13 figures with the SFRs obtained from fits to the MIPS+*Herschel* data are similar at $z \lesssim 2$, 0.04 dex offset, and 0.2–0.3 dex scatter, but considerably worse at $z \gtrsim 2$, where the systematic offset is larger than 0.2 dex, reaching 0.5 dex at $z > 5$ (in all cases, the SFRs obtained from the fits are larger than those obtained with the R13 recipe), and the scatter is 0.4 dex.

For the galaxies with no IR detection, we used a UV-based SFR obtained by applying an attenuation correction, $A(UV)$, to the observed UV luminosity. Typically, this correction is estimated by measuring the UV spectral index, β_{UV}, and transforming it to an attenuation using a recipe such as the one presented in Meurer et al. (1999). This procedure is based on the fact that young ($\lesssim$100 Myr) starbursts with no dust present a slope of ~ -2.2 (for metallicities as low as 1/20 solar; see, e.g., Leitherer et al. 2014) when using f_{λ} (our fiducial definition; note that this is the same as a flat slope spectrum when plotting the flux density in terms of f_{ν}). In the presence of dust (and also for older stellar populations), and assuming typical dust properties, the UV slope typically becomes flatter (but not always; see Witt & Gordon 2000), offering an opportunity to estimate the attenuation. However, transforming β_{UV} into a UV attenuation depends on the properties of the dust and its relative location with respect to the stars (Witt & Gordon 2000; Popping et al. 2017; Narayanan et al. 2018). In addition, as mentioned above, the UV slope is also mildly dependent on age for young starbursts ($t < 100$ Myr), but the effect of age dominates for more evolved stellar populations. Consequently, different types of galaxies present different relationships between β_{UV} and $A(UV)$. For local starbursts, Meurer et al. (1999) compared UV and far-IR luminosities, using their ratio (IRX) and its relationship with β_{UV} to provide an easy-to-use attenuation recipe. However, many papers in the literature have shown that the IRX–β_{UV} relation presented in Meurer et al. (1999) is not universal (among many, Pettini et al. 1998; Kong et al. 2004; Buat et al. 2005, 2012; Dale et al. 2009; Reddy et al. 2010, 2018; Overzier et al. 2011; Casey et al. 2014; Popping et al. 2017; McLure et al. 2018; Narayanan et al. 2018). In general, using the Meurer et al. IRX–β_{UV} relationship for all galaxies, which is common in the literature, will provide acceptable UV attenuations for active SFGs similar to those studied by Meurer and collaborators. However, this procedure will overestimate the effect of dust for more relaxed systems, which dominate the galaxy population at low redshifts (see Dale et al. 2009; Casey et al. 2014), and subestimate the attenuation for heavily obscured galaxies, such as (U)LIRGs and SMGs at high redshifts (see, e.g., Overzier et al. 2010; Nordon et al. 2013; Salmon et al. 2015; Bouwens et al. 2016).

Based on the results from the literature discussed in the previous paragraph, in this paper we present an elaborate method to account for the differences in IRX–β_{UV} relationships from galaxy to galaxy. Our empirical recipe is based on the fact that galaxies present a variety of attenuation laws (which translate to different IRX–β_{UV} relationships; see, e.g., Witt & Gordon 2000), but it is also dependent on data depth (in the mid- and far-IR, as well as in the UV and near-infrared) for the CANDELS fields. Our method relies on two pillars: the construction of IRX–β_{UV} relationships for different types of galaxies and the actual detection limits of the *Spitzer*/MIPS and *Herschel* surveys, which impose upper limits on the SFR calculations for IR-undetected galaxies.

Figure 25 shows the SFR_{IR} limits of the MIPS and *Herschel* surveys in the CANDELS fields. The gray line marks the boundary of the IR detections (90% of galaxies lie above that line). We remark that any galaxy presenting a large enough amount of dust should be detected in the IR and lie above the gray line. Analogously, for galaxies with no IR detection, the amount of dust must be limited so the absorbed part of the SFR can stay below the observational limits. We note that the IR surveys in each CANDELS field count with different depths. In this plot, we show the SFR_{IR} limits based on the deepest data sets (in the two GOODS fields), but our method to estimate

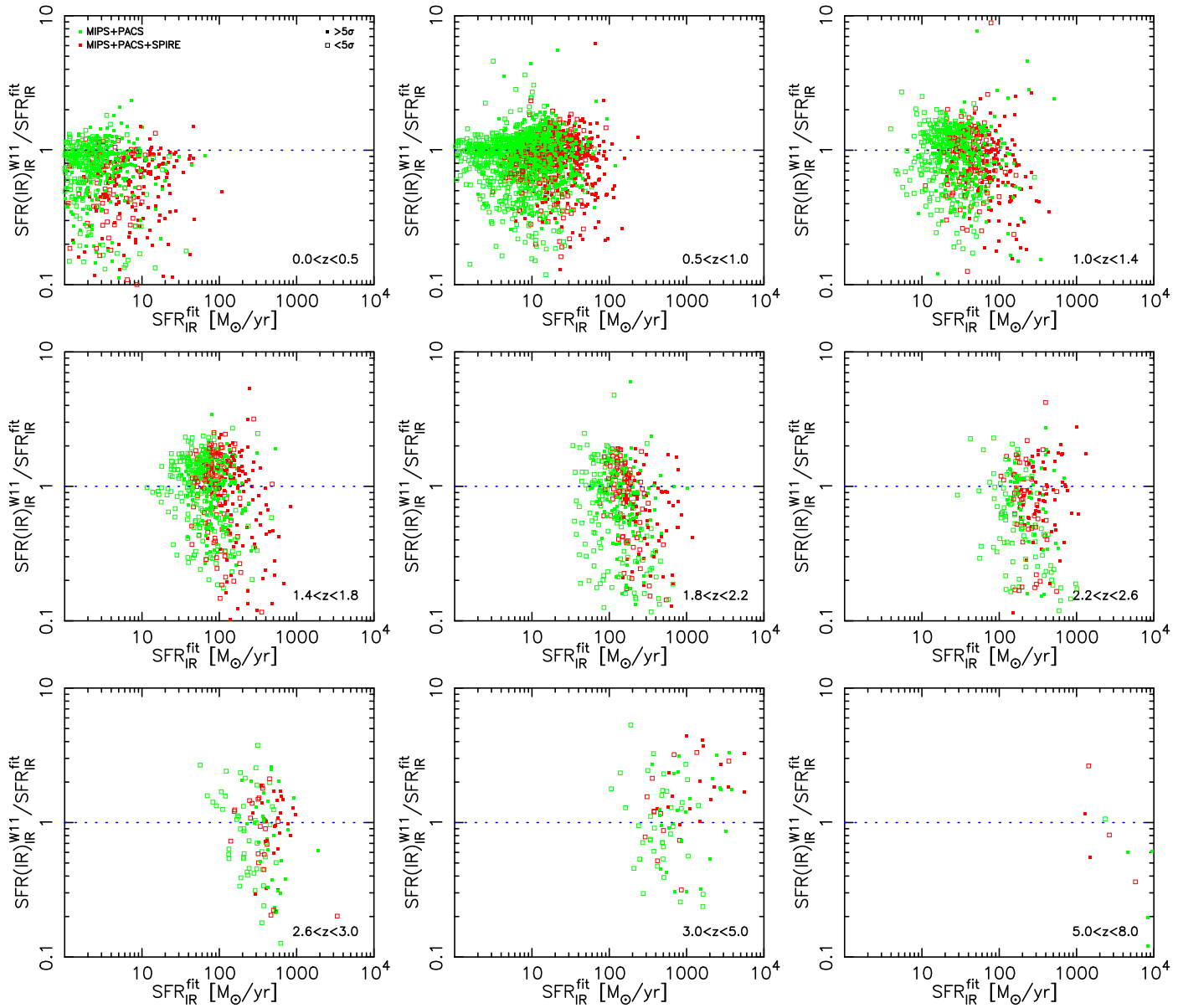

Figure 24. Comparison of the SFR estimations based on the MIPS 24 μm fluxes alone (using the Wuyts et al. 2011a recipe; SFR_{IR}^{W11}) with the SFRs calculated by fitting the MIPS and *Herschel* flux data points to dust emission models (see text for details; SFR_{IR}^{fit}) for all IR detections in the five CANDELS fields. We divide the sample in galaxies detected, apart from MIPS, by both PACS and SPIRE (red points) or only by PACS (green points). Filled points refer to galaxies with at least 5σ detections; open points represent less significant detections.

SFRs from UV data alone properly scales up the limits for the other CANDELS fields.

Different IRX–β_{UV} relationships were built for galaxies as a function of their IR-based SFRs. We divided the total sample of IR emitters into 11 bins (roughly equal in linear space, except at the extremes, where the bins are larger to count with enough galaxies) of L(8–1000): one bin for HyLIRGs [L(8–1000) > $10^{13}\,L_{\odot}$], three bins for ULIRGs [L(8–1000) = $10^{12-13}\,L_{\odot}$], three for LIRGs [L(8–1000) = $10^{11-12}\,L_{\odot}$], three for starbursts [L(8–1000) = $10^{10-11}\,L_{\odot}$], and one bin for the galaxies with the lowest luminosities [L(8–1000) < $10^{10}\,L_{\odot}$]. For each subsample, we built an IRX–β_{UV} relationship fitting the data points to a Chebyshev polynomial of order 5 (given in Table 14). Figure 26 shows the results when considering UV-based SFRs using the 160 and 280 nm estimators. It is readily clear that the galaxies with brighter IR luminosities present higher IRX values for the same UV slope. We find that the Meurer et al. (1999) relationship is a good approximation for galaxies with $SFR_{IR} \sim$ 1–100 $M_{\odot}\,yr^{-1}$, consistent with the SFRs of the local starbursts used in that work (Heckman et al. 1998). Galaxies with smaller levels of star formation (in our sample, this implies $z \lesssim 1$, because the IR surveys are not deep enough to detect such galaxies at high redshift) lie below the Meurer et al. relationship. The brightest LIRGs, ULIRGs, and HyLIRGs present higher attenuations for the same UV slope value compared to the Meurer et al. curve. Note that the differences in IRX–β_{UV} curves imply different attenuation laws (Charlot & Fall 2000; Witt & Gordon 2000).

Using the results presented in Figures 25 and 26, we can now estimate attenuation-corrected UV-based SFRs for sources with no IR detection. For a given galaxy, we have its redshift and a β_{UV} estimation obtained by either fitting directly the UV flux

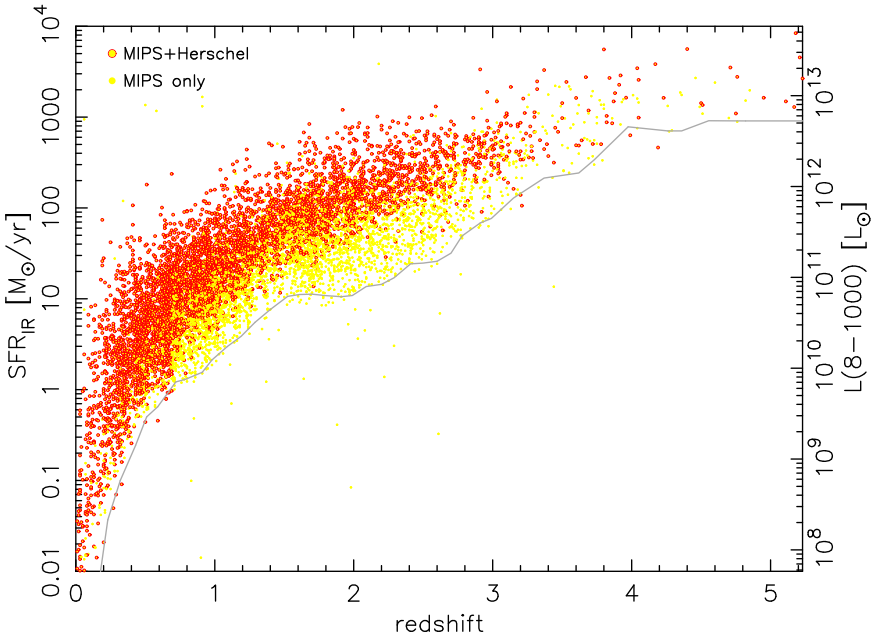

Figure 25. Observational limits of the mid- and far-IR surveys carried out by *Spitzer* with MIPS and *Herschel* with PACS and SPIRE in the five CANDELS fields. The IR-based SFR, SFR_{IR} (i.e., the unabsorbed part of the total SFR has not been taken into account), is plotted as a function of redshift. Galaxies with *Herschel* detections are marked in red (and $SFR_{IR} = SFR_{IR}^{fit}$; see the text for details), galaxies with just a MIPS detection are plotted in yellow (and $SFR_{IR} = SFR_{IR}^{W11}$). The gray line marks the fluxes above which we can find 90% of the IR sources for GOODS-N and GOODS-S, the two CANDELS fields with the deepest MIPS/PACS/SPIRE data.

Table 14
IRX–β_{UV} Relationships as a Function of SFR_{IR}

SFR_{IR} range (1)	T_0 (2)	T_1 (2)	T_2 (2)	T_3 (2)	T_4 (2)
			160 nm		
$SFR_{IR} > 1050$	+2.920720	$+2.86435 \times 10^{-01}$	-6.78813×10^{-03}	$+1.88041 \times 10^{-01}$	-5.50707×10^{-02}
$500 < SFR_{IR} < 1050$	+2.741810	$+6.99146 \times 10^{-01}$	$+1.11188 \times 10^{-01}$	-8.58467×10^{-02}	-1.58543×10^{-01}
$300 < SFR_{IR} < 500$	+2.527450	$+4.06804 \times 10^{-01}$	-9.03771×10^{-03}	$+1.60448 \times 10^{-01}$	-3.49370×10^{-02}
$105 < SFR_{IR} < 300$	+2.333380	$+8.51482 \times 10^{-01}$	$+8.76543 \times 10^{-02}$	-1.91654×10^{-01}	-1.66376×10^{-01}
$75 < SFR_{IR} < 105$	+2.084330	$+8.26576 \times 10^{-01}$	$+9.61815 \times 10^{-02}$	-1.43602×10^{-01}	-1.35397×10^{-01}
$45 < SFR_{IR} < 75$	+1.963200	$+7.20402 \times 10^{-01}$	$+1.69449 \times 10^{-01}$	-5.59624×10^{-02}	-1.15281×10^{-01}
$11 < SFR_{IR} < 45$	+1.609040	$+6.55166 \times 10^{-01}$	$+1.14031 \times 10^{-01}$	-1.15595×10^{-01}	-1.19841×10^{-01}
$7.5 < SFR_{IR} < 11$	+1.361420	$+7.30849 \times 10^{-01}$	$+1.04347 \times 10^{-01}$	-2.15491×10^{-01}	-1.43217×10^{-01}
$4.5 < SFR_{IR} < 7.5$	+1.288050	$+7.16792 \times 10^{-01}$	$+7.21248 \times 10^{-02}$	-2.07808×10^{-01}	-1.30655×10^{-01}
$1.1 < SFR_{IR} < 4.5$	+1.129310	$+7.96516 \times 10^{-01}$	$+8.45170 \times 10^{-02}$	-2.11392×10^{-01}	-1.18125×10^{-01}
$SFR_{IR} < 1.1$	+0.849941	$+4.50507 \times 10^{-01}$	$+8.16457 \times 10^{-02}$	-2.36188×10^{-02}	-5.08052×10^{-02}
			280 nm		
$SFR_{IR} > 1050$	2.52088	$+3.49898 \times 10^{-01}$	-8.05563×10^{-02}	$+1.04188 \times 10^{-01}$	-5.78644×10^{-02}
$500 < SFR_{IR} < 1050$	2.22664	$+4.85975 \times 10^{-01}$	$+8.61690 \times 10^{-02}$	-1.04035×10^{-01}	-1.64763×10^{-01}
$300 < SFR_{IR} < 500$	2.00424	$+1.30284 \times 10^{-01}$	-1.97642×10^{-02}	$+1.57070 \times 10^{-01}$	-4.37325×10^{-02}
$105 < SFR_{IR} < 300$	1.78244	$+5.72340 \times 10^{-01}$	$+1.02271 \times 10^{-01}$	-1.56439×10^{-01}	-1.61426×10^{-01}
$75 < SFR_{IR} < 105$	1.52895	$+5.97391 \times 10^{-01}$	$+1.80602 \times 10^{-01}$	-1.29600×10^{-01}	-1.50702×10^{-01}
$45 < SFR_{IR} < 75$	1.46421	$+5.65381 \times 10^{-01}$	$+1.34942 \times 10^{-01}$	-1.98317×10^{-01}	-1.73069×10^{-01}
$11 < SFR_{IR} < 45$	1.04869	$+3.38949 \times 10^{-01}$	$+1.47252 \times 10^{-01}$	-4.06656×10^{-02}	-1.03828×10^{-01}
$7.5 < SFR_{IR} < 11$	0.80222	$+4.40004 \times 10^{-01}$	$+1.42895 \times 10^{-01}$	-1.66367×10^{-01}	-1.38347×10^{-01}
$4.5 < SFR_{IR} < 7.5$	0.72929	$+4.08079 \times 10^{-01}$	$+1.45188 \times 10^{-01}$	-1.01459×10^{-01}	-1.07982×10^{-01}
$1.1 < SFR_{IR} < 4.5$	0.58280	$+4.91613 \times 10^{-01}$	$+1.05090 \times 10^{-01}$	-1.42693×10^{-01}	-1.01624×10^{-01}
$SFR_{IR} < 1.1$	0.31596	$+2.53008 \times 10^{-01}$	$+6.50686 \times 10^{-02}$	-1.30536×10^{-01}	-9.86393×10^{-02}

Note. (1) SFR_{IR} range (in $M_{\odot}$ yr^{-1}). (2) Chebyshev polynomial coefficients.

points at wavelengths between 120 and 260 nm, or by measuring slopes in the models used to estimate stellar masses (see Section 4). We note that both types of estimations provide very similar results, with an average systematic offset $\Delta\beta < 0.01$. With the redshift, we can obtain from Figure 25 an upper limit for the SFR based on the detection limit of the

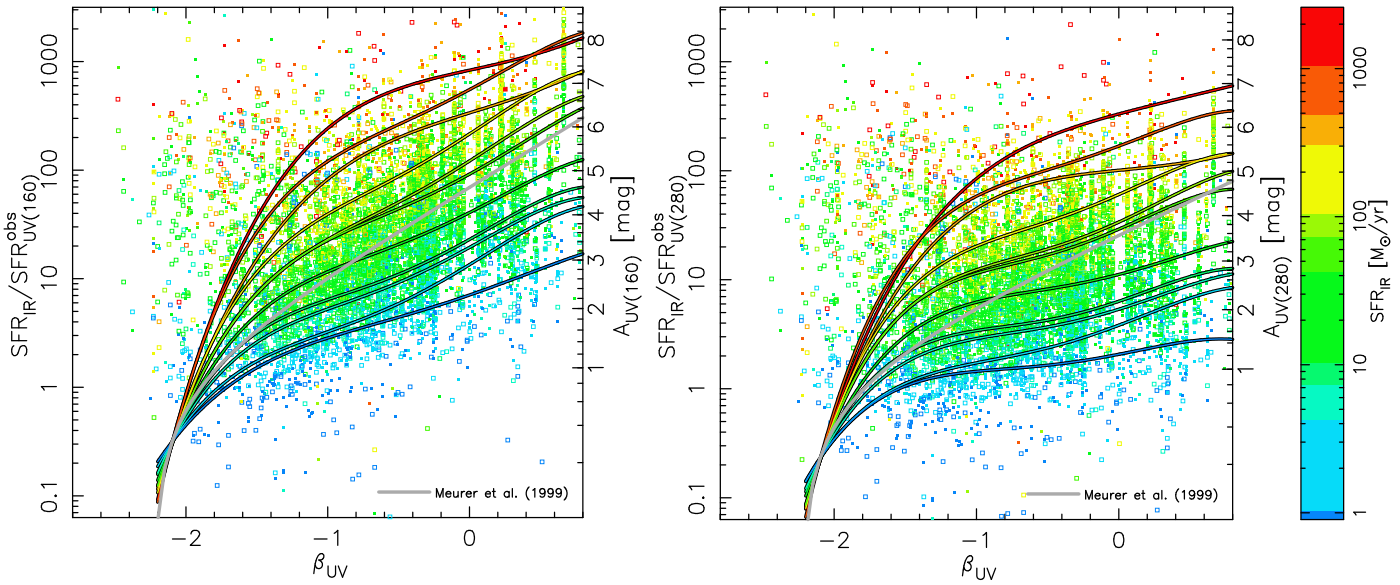

Figure 26. IRX–β_{UV} plots for the galaxies detected by MIPS/PACS/SPIRE in the five CANDELS fields. On the left, we show the results for UV-based SFR estimations based on the emission at 160 nm rest frame (Equation (D.4), Kennicutt 1998), and on the right for 280 nm (Equation (D.5), Bell et al. 2003). Galaxies with *Herschel* detections are plotted with filled symbols (and $SFR_{IR} = SFR_{IR}^{fit}$, see text for details); galaxies with just a MIPS detection are plotted with open symbols (and $SFR_{IR} = SFR_{IR}^{W11}$). Colors represent different bins of IR-based SFR [or $L(8-1000)$] as shown in the scale plotted on the right. The data for each bin has been fitted to a Chebyshev polynomial of order 5, shown with lines of the same color. The Meurer et al. (1999) relationship is plotted in gray (using the Calzetti et al. 2000 attenuation law to transform from far-UV to near-UV A_{UV} values). The IRX scale (on the left of each panel) is transformed into an attenuation scale (on the right of each panel) using Equation (4).

MIPS/*Herschel* surveys in the CANDELS fields. The upper-limit SFR is used to select an IRX–β_{UV} relationship from Figure 26, which allows us to translate from β_{UV} to attenuation in the UV (in one of the two considered wavelengths). With this attenuation, we correct the observed $SFR_{UV-\lambda}^{obs}$ to get the dust-corrected SFR_{UV}^{corr}, which is equal to SFR_{TOT}. The obtained value of SFR_{UV}^{corr} might be higher than the detection limit of the IR surveys. In this case, we recalculate the attenuation using a lower IRX–β_{UV} relationship until the estimation is consistent with the nondetection at mid- and far-IR wavelengths. Two further refinements are included in our method. First, for each galaxy we calculate a UV-based dust-corrected SFR using both the 160 and the 280 nm estimator, and we average them to provide a final value. Typically, the two estimations are consistent within less than 0.05 dex. Second, we iteratively calculate a main sequence for different redshift bins (see Figure 27) and avoid outliers at the bright end that deviate more than 5σ.

Summarizing, we have developed a method to calculate SFRs on a galaxy-by-galaxy basis following a ladder approach. For the most extreme galaxies at the highest part of the ladder, which are detected by both MIPS and *Herschel*, total SFRs are calculated with dust emission models fitting the IR data points and adding the unobscured star formation. For less extreme cases in the middle of the ladder, we have measured the obscured star formation directly from MIPS data, which are highly sensitive to the amount of dust. For sources at the bottom of the ladder that have not been detected by the mid- and far-IR surveys, we calculate the SFRs taking into account differences in the attenuation law, linked to different IR-to-UV ratios.

Using this methodology, we obtained a total SFR, SFR_{TOT}, for each galaxy. Figure 27 shows an SFR versus stellar-mass plot for the more than 186,000 galaxies in the CANDELS catalogs, divided into nine redshift bins and taking into account star formation activity as inferred from the *UVJ* diagrams. A running median has been run through the data (with a minimum of 200 points) to obtain the position of the main sequence (relation between SFR and mass for those galaxies identified as star-forming based on the *UVJ* diagram, i.e., after excluding quiescent galaxies). Medians and rms values for these main sequences built with the entire CANDELS data set are given in Table 15. Several interesting results can be extracted from this plot. First, our methodology produces a main sequence of galaxies where the non-IR detections nicely join the trend followed by the IR emitters. Second, the main sequences inferred from our results are, overall, consistent with the results in the literature (in particular, we compare with Speagle et al. 2014, Whitaker et al. 2014, and Schreiber et al. 2015b). However, we note that, if we consider the SFR versus mass relation for all galaxies, including quiescent systems, the SFR–*M* trend becomes flat at higher masses, and even reverses the sign of the slope at low redshifts ($z < 1$), where the red sequence is populated by large numbers of dead galaxies. Table 16 gives the Chebyshev coefficients of our fits to the main-sequence (just considering SFGs above the mass-completeness limit) and general SFR–*M* (including all galaxies) relationships shown in Figure 27.

D.3. Comparison to Other IR-based SFR Catalogs

In order to further verify the quality of the far-IR photometric catalogs and the SFRs based on them, we compare our values to those from two independent works using similar data sets. These are the MIPS24 photometric and SFR catalog of the 3D-HST survey, presented in Momcheva et al. (2016) and Whitaker et al. (2014), and the *Spitzer*+*Herschel*+VLA photometric and SFR catalog of GOODS-N galaxies, presented in Liu et al. (2018, hereafter L18).

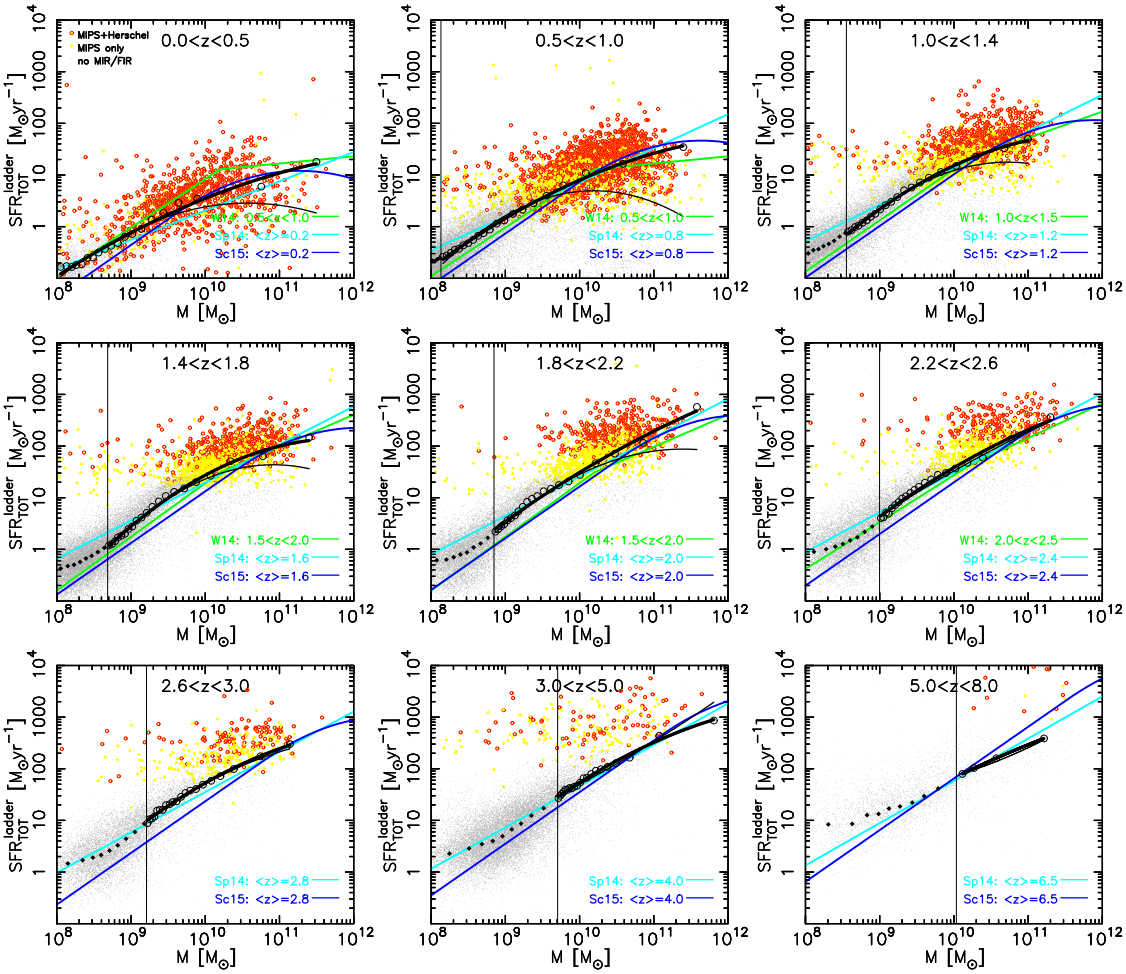

Figure 27. Total SFRs vs. stellar masses for all cataloged galaxies in the five CANDELS fields, divided into nine redshift bins. The SFRs have been estimated with the ladder approach described in this appendix, and the three layers are marked with different colors: MIPS/*Herschel* sources in red, MIPS-only sources in yellow, and UV-only sources in gray. Stellar masses are taken from Santini et al. (2015) for CANDELS fields except GOODS-N, whose masses are presented in this paper. For each bin, we plot the main-sequence curves according to Whitaker et al. (2014, green lines), Speagle et al. (2014, cyan), and Schreiber et al. (2015b, blue), for the redshifts or universe ages shown in the legend of each panel. We also depict the trends of the SFR as a function of mass based on the calculations presented in this paper for the sample of SFGs built after removing quiescent systems with *UVJ* diagrams. Points plotted in black depict running medians for the SFGs: open circles correspond to galaxies with stellar masses larger than the stellar-mass limits given in Grazian et al. (2015, vertical gray lines), diamonds to galaxies below those limits. The previous data points are fitted with Chebyshev polynomials (thick black lines). The relationship between the SFR and stellar mass for all galaxies (SFGs jointly with quiescent galaxies) is also shown with thin black lines.

Table 15
Main-sequence Data Points and Scatter

log(M) (1)	log(SFR) (2)	log(M) (1)	log(SFR) (2)	log(M) (1)	log(SFR) (2)	log(M) (1)	log(SFR) (2)	log(M) (1)	log(SFR) (2)
$0.0 < z < 0.5$		$0.5 < z < 1.0$		$1.0 < z < 1.4$		$1.4 < z < 1.8$		$1.8 < z < 2.2$	
8.050	-0.78 ± 0.21	8.019	-0.66 ± 0.21	8.036	-0.52 ± 0.30	8.051	-0.37 ± 0.29	8.077	-0.21 ± 0.30
8.131	-0.77 ± 0.23	8.053	-0.67 ± 0.25	8.106	-0.46 ± 0.28	8.148	-0.33 ± 0.30	8.205	-0.20 ± 0.33
8.200	-0.78 ± 0.22	8.087	-0.63 ± 0.25	8.175	-0.44 ± 0.29	8.232	-0.30 ± 0.30	8.304	-0.15 ± 0.34
8.262	-0.74 ± 0.23	8.119	-0.61 ± 0.26	8.244	-0.38 ± 0.29	8.314	-0.24 ± 0.30	8.395	-0.10 ± 0.33
8.336	-0.73 ± 0.22	8.159	-0.58 ± 0.27	8.314	-0.33 ± 0.27	8.392	-0.18 ± 0.30	8.484	-0.06 ± 0.34
8.412	-0.61 ± 0.24	8.211	-0.56 ± 0.27	8.386	-0.28 ± 0.29	8.469	-0.13 ± 0.28	8.573	$+0.04 \pm 0.35$
8.487	-0.60 ± 0.26	8.264	-0.51 ± 0.28	8.461	-0.20 ± 0.28	8.552	-0.05 ± 0.31	8.666	$+0.11 \pm 0.34$
8.561	-0.50 ± 0.25	8.319	-0.45 ± 0.27	8.540	-0.12 ± 0.29	8.640	$+0.03 \pm 0.31$	8.764	$+0.22 \pm 0.33$
8.648	-0.43 ± 0.29	8.375	-0.43 ± 0.29	8.574	-0.10 ± 0.31	8.705	$+0.08 \pm 0.29$	8.866	$+0.34 \pm 0.31$
8.731	-0.37 ± 0.28	8.435	-0.36 ± 0.30	8.621	-0.07 ± 0.28	8.745	$+0.11 \pm 0.30$	8.904	$+0.39 \pm 0.31$
8.823	-0.32 ± 0.29	8.499	-0.32 ± 0.30	8.667	-0.01 ± 0.28	8.786	$+0.16 \pm 0.30$	8.944	$+0.44 \pm 0.35$
8.915	-0.20 ± 0.32	8.566	-0.26 ± 0.31	8.715	$+0.02 \pm 0.30$	8.825	$+0.23 \pm 0.31$	8.983	$+0.48 \pm 0.31$
9.018	-0.14 ± 0.35	8.634	-0.18 ± 0.31	8.768	$+0.08 \pm 0.27$	8.870	$+0.26 \pm 0.31$	9.028	$+0.56 \pm 0.31$
9.140	-0.05 ± 0.34	8.705	-0.12 ± 0.29	8.824	$+0.12 \pm 0.29$	8.917	$+0.30 \pm 0.32$	9.075	$+0.60 \pm 0.30$
9.279	$+0.14 \pm 0.35$	8.789	-0.06 ± 0.31	8.880	$+0.19 \pm 0.30$	8.965	$+0.40 \pm 0.31$	9.127	$+0.65 \pm 0.31$

Table 15
(Continued)

log(M) (1)	log(SFR) (2)	log(M) (1)	log(SFR) (2)	log(M) (1)	log(SFR) (2)	log(M) (1)	log(SFR) (2)	log(M) (1)	log(SFR) (2)
9.437	+0.27 ± 0.38	8.884	+0.06 ± 0.31	8.939	+0.25 ± 0.31	9.015	+0.44 ± 0.34	9.177	+0.74 ± 0.28
9.641	+0.46 ± 0.35	8.987	+0.12 ± 0.28	9.006	+0.33 ± 0.26	9.075	+0.55 ± 0.29	9.234	+0.82 ± 0.28
9.893	+0.54 ± 0.37	9.100	+0.24 ± 0.30	9.080	+0.42 ± 0.29	9.140	+0.62 ± 0.31	9.294	+0.92 ± 0.27
10.228	+0.70 ± 0.48	9.231	+0.33 ± 0.28	9.154	+0.48 ± 0.29	9.211	+0.71 ± 0.30	9.358	+0.98 ± 0.24
10.754	+0.77 ± 0.70	9.379	+0.45 ± 0.30	9.236	+0.57 ± 0.30	9.287	+0.82 ± 0.28	9.430	+1.03 ± 0.22
		9.557	+0.60 ± 0.32	9.329	+0.70 ± 0.25	9.374	+0.93 ± 0.27	9.516	+1.12 ± 0.21
		9.781	+0.80 ± 0.35	9.429	+0.76 ± 0.26	9.468	+1.03 ± 0.24	9.614	+1.17 ± 0.19
		10.083	+1.04 ± 0.45	9.542	+0.85 ± 0.28	9.581	+1.11 ± 0.23	9.723	+1.25 ± 0.24
		10.584	+1.21 ± 0.55	9.663	+0.95 ± 0.25	9.716	+1.18 ± 0.23	9.852	+1.31 ± 0.28
		11.397	+1.54 ± 0.28	9.825	+1.06 ± 0.28	9.876	+1.30 ± 0.30	10.006	+1.44 ± 0.37
				10.029	+1.18 ± 0.37	10.072	+1.42 ± 0.43	10.215	+1.67 ± 0.47
				10.296	+1.36 ± 0.54	10.341	+1.71 ± 0.52	10.476	+1.85 ± 0.54
				10.680	+1.51 ± 0.56	10.776	+1.80 ± 0.62	10.855	+2.07 ± 0.55
				10.997	+1.70 ± 0.60	11.400	+2.17 ± 0.32	11.581	+2.76 ± 0.66
$2.2 < z < 2.6$		$2.6 < z < 3.0$		$3.0 < z < 5.0$		$5.0 < z < 8.0$			
8.115	−0.05 ± 0.31	8.148	+0.16 ± 0.30	8.246	+0.36 ± 0.33	8.308	+0.92 ± 0.43		
8.278	+0.00 ± 0.34	8.348	+0.23 ± 0.32	8.512	+0.46 ± 0.34	8.630	+0.93 ± 0.34		
8.402	+0.05 ± 0.33	8.486	+0.28 ± 0.34	8.684	+0.54 ± 0.35	8.830	+1.10 ± 0.36		
8.503	+0.10 ± 0.33	8.597	+0.33 ± 0.37	8.831	+0.60 ± 0.36	8.985	+1.13 ± 0.33		
8.601	+0.17 ± 0.37	8.710	+0.42 ± 0.37	8.961	+0.69 ± 0.37	9.124	+1.23 ± 0.29		
8.699	+0.23 ± 0.36	8.821	+0.52 ± 0.35	9.087	+0.83 ± 0.36	9.274	+1.27 ± 0.34		
8.799	+0.34 ± 0.35	8.934	+0.64 ± 0.37	9.213	+0.94 ± 0.36	9.439	+1.34 ± 0.32		
8.899	+0.44 ± 0.36	9.052	+0.78 ± 0.34	9.351	+1.09 ± 0.34	9.598	+1.47 ± 0.30		
9.016	+0.61 ± 0.41	9.177	+0.94 ± 0.33	9.516	+1.24 ± 0.34	9.790	+1.62 ± 0.34		
9.050	+0.62 ± 0.33	9.223	+0.94 ± 0.33	9.715	+1.43 ± 0.34	10.115	+1.90 ± 0.33		
9.085	+0.71 ± 0.33	9.252	+1.02 ± 0.35	9.738	+1.48 ± 0.28	10.270	+2.01 ± 0.44		
9.122	+0.69 ± 0.35	9.283	+1.04 ± 0.29	9.761	+1.51 ± 0.24	10.570	+2.20 ± 0.39		
9.164	+0.79 ± 0.31	9.315	+1.08 ± 0.31	9.784	+1.55 ± 0.30	11.213	+2.59 ± 0.47		
9.209	+0.86 ± 0.34	9.351	+1.19 ± 0.28	9.808	+1.59 ± 0.24				
9.256	+0.91 ± 0.29	9.389	+1.21 ± 0.29	9.837	+1.59 ± 0.31				
9.303	+0.98 ± 0.25	9.427	+1.20 ± 0.28	9.864	+1.63 ± 0.33				
9.356	+1.03 ± 0.33	9.471	+1.29 ± 0.26	9.894	+1.62 ± 0.32				
9.411	+1.09 ± 0.30	9.520	+1.31 ± 0.30	9.928	+1.65 ± 0.29				
9.470	+1.15 ± 0.26	9.562	+1.36 ± 0.26	9.966	+1.67 ± 0.35				
9.529	+1.21 ± 0.28	9.613	+1.37 ± 0.32	10.007	+1.73 ± 0.26				
9.609	+1.29 ± 0.21	9.674	+1.46 ± 0.27	10.052	+1.82 ± 0.37				
9.693	+1.36 ± 0.25	9.732	+1.53 ± 0.21	10.099	+1.83 ± 0.32				
9.783	+1.44 ± 0.23	9.799	+1.58 ± 0.29	10.157	+1.90 ± 0.31				
9.890	+1.48 ± 0.20	9.875	+1.61 ± 0.29	10.219	+1.96 ± 0.32				
10.022	+1.57 ± 0.29	9.969	+1.69 ± 0.23	10.289	+1.99 ± 0.38				
10.180	+1.67 ± 0.37	10.080	+1.77 ± 0.25	10.374	+2.03 ± 0.34				
10.390	+1.77 ± 0.50	10.204	+1.86 ± 0.39	10.490	+2.11 ± 0.40				
10.773	+2.14 ± 0.49	10.384	+2.00 ± 0.43	10.675	+2.21 ± 0.49				
11.301	+2.56 ± 0.36	10.742	+2.24 ± 0.53	11.077	+2.64 ± 0.49				
		11.142	+2.48 ± 0.44	11.809	+2.94 ± 0.25				

Note. (1) Stellar mass in units of $M_{\odot}$. (2) Median SFR and rms (in $M_{\odot}$ yr^{-1}) defining the main sequence.

The 3D-HST catalog is similar to ours in the sense that it provides far-IR photometry to WFC3-selected sources in the five CANDELS fields. Therefore, it is straightforward to identify common sources by cross-matching celestial coordinates within a 0.″3 search radius, as we have done in Section 4.2. The MIPS 24 μm photometry in the 3D-HST and CANDELS catalogs is computed following slightly different procedures. The CANDELS photometry, as described in Appendix D.1, is based on direct detections of point-like sources whose fluxes are measured using circular apertures and applying aperture corrections. Then, each MIPS source is associated to its most likely F160W counterpart using brightness and proximity criteria. The 3D-HST catalog measures the MIPS 24 μm fluxes following the same method as with all other optical-to-NIR bands, i.e., they used the convolution software MOPHONGO (Labbé et al. 2013) on the WFC3 high-resolution images to model and subtract the contributions from neighboring blended sources in the lower resolution MIPS24 image. Then, they use circular aperture photometry on the "clean" cutout of each source to measure the flux, and they apply an aperture correction of 20% to determine the total magnitude.

In addition to the MIPS24 fluxes, the 3D-HST catalog provides the IR and total SFRs computed following a similar

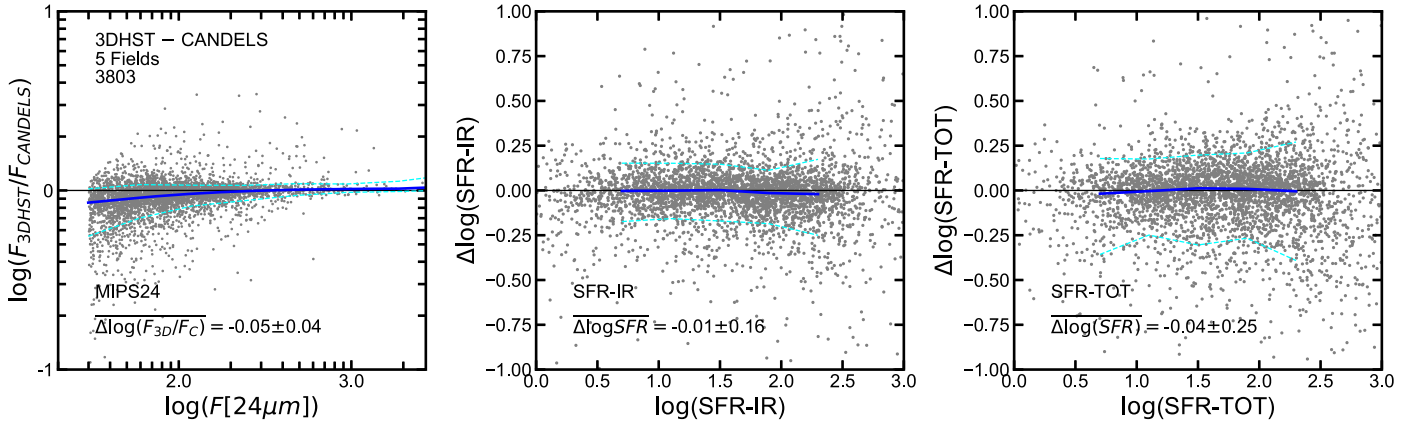

Figure 28. Comparison of MIPS 24 μm fluxes and SFRs between the CANDELS (this work) and 3D-HST catalogs (Momcheva et al. 2016) in the five fields of the CANDELS survey. From left to right, comparison of the MIPS24 fluxes, IR-based SFRs, and total (UV+IR) SFRs. The y axis shows the differences in 3D-HST minus CANDELS values. The comparison is restricted to galaxies detected above S/N = 5 in MIPS24 in both catalogs. The blue lines show the running median and $\pm 1\sigma$ scatter of the distribution whose average values are indicated in the bottom-left corner. The values in each panel have been corrected by a constant offset derived from the average running median. Overall, we find a good agreement in the fluxes and SFRs between the two catalogs. The CANDELS MIPS24 fluxes are only marginally brighter than the 3D-HST ones by 0.05 dex. Such difference has little impact on the two SFRs which exhibit offsets of 0.01 and 0.04 dex, respectively.

Table 16
SFR versus Stellar Mass and Main-sequence Fits to Chebyshev Polynomials

Redshift Interval (1)	$M_{\rm min}$ (2)	Sample (3)	T_0 (4)	T_1 (4)	T_2 (4)
$0.0 < z < 0.5$	6.9	SFG	$-1.39684 \times 10^{+01}$	$+2.32388$	-8.72415×10^{-02}
		ALL	$-2.45250 \times 10^{+01}$	$+4.72555$	-2.23490×10^{-01}
$0.5 < z < 1.0$	8.1	SFG	$-1.64662 \times 10^{+01}$	$+2.84365$	-1.10703×10^{-01}
		ALL	$-3.47832 \times 10^{+01}$	$+6.96338$	-3.41690×10^{-01}
$1.0 < z < 1.4$	8.6	SFG	$-2.30977 \times 10^{+01}$	$+4.18836$	-1.76068×10^{-01}
		ALL	$-3.36487 \times 10^{+01}$	$+6.50548$	-3.03193×10^{-01}
$1.4 < z < 1.8$	8.7	SFG	$-2.75708 \times 10^{+01}$	$+5.02435$	-2.12376×10^{-01}
		ALL	$-3.75337 \times 10^{+01}$	$+7.17562$	-3.28619×10^{-01}
$1.8 < z < 2.2$	8.9	SFG	$-1.48351 \times 10^{+01}$	$+2.39121$	-7.58761×10^{-02}
		ALL	$-3.08932 \times 10^{+01}$	$+5.76395$	-2.52960×10^{-01}
$2.2 < z < 2.6$	9.0	SFG	$-1.75258 \times 10^{+01}$	$+2.97979$	-1.06905×10^{-01}
		ALL	$-1.23610 \times 10^{+01}$	$+1.96159$	-5.73675×10^{-02}
$2.6 < z < 3.0$	9.2	SFG	$-2.11659 \times 10^{+01}$	$+3.76568$	-1.47664×10^{-01}
		ALL	$-2.30500 \times 10^{+01}$	$+4.16377$	-1.68796×10^{-01}
$3.0 < z < 5.0$	9.7	SFG	-2.01471×10^{-01}	$+3.47129$	-1.28317×10^{-01}
		ALL	$+4.48905 \times 10^{-01}$	-5.13682×10^{-01}	$+6.38656 \times 10^{-02}$
$5.0 < z < 8.0$	10.0	SFG	$-1.16582 \times 10^{+01}$	$+1.98906$	-6.40982×10^{-02}
		ALL	$+1.05884 \times 10^{+01}$	-2.16663	$+1.29366 \times 10^{-01}$

Note. (1) Redshift interval (same as in Figure 27). (2) Stellar-mass-completeness level of the CANDELS catalogs from Grazian et al. (2015). (3) Sample of galaxies: star-forming galaxies (SFGs) identified with the *UVJ* diagrams, and the entire sample (ALL) adding quiescent galaxies to the previous sample. (4) Chebyshev polynomial coefficients (order 3).

methodology to the one described in Appendix D.2, i.e., they use the MIPS 24 μm fluxes and the redshifts of the galaxies to estimate bolometric IR luminosities using the IR emission templates of Wuyts et al. (2011a). These luminosities are transformed to SFRs using the Kennicutt (1998) calibration, assuming a Chabrier (2003) IMF. Lastly, they estimate total SFRs by adding the IR SFR to the UV SFR estimated from the observed UV luminosity computed from the fitting of the optical-to-NIR SED of each galaxy.

Figure 28 shows the comparison of the MIPS 24 μm fluxes and SFRs (IR and total) between the CANDELS and 3D-HST catalogs. The blue and cyan lines indicate the running median and 1σ percentiles. The values in each panel have been normalized by applying a constant offset (indicated in the bottom-left corner) determined from the average value of the running median. Overall, the comparison suggests that the values in the CANDELS and 3D-HST catalogs are quite consistent. The CANDELS MIPS24 fluxes are slightly brighter than the 3D-HST by 0.05 dex. This small difference is the same in the five cosmological fields, which suggest that the origin could be a small systematic difference in the photometric zero points or perhaps in the value of the aperture correction. Interestingly, despite the small offset in the MIPS24 photometry, the IR-based SFRs are in excellent agreement with a median difference of just ΔSFR $= -0.01$ dex. The $\sim$0.12 dex scatter in the comparison of IR SFRs is also quite small compared, for example, to the 0.3 dex scatter in the comparison of stellar masses shown in Section 5.3. Such small scatter is probably caused by small differences in the MIPS flux, redshift, or the dust emission templates. Likewise, the comparison of

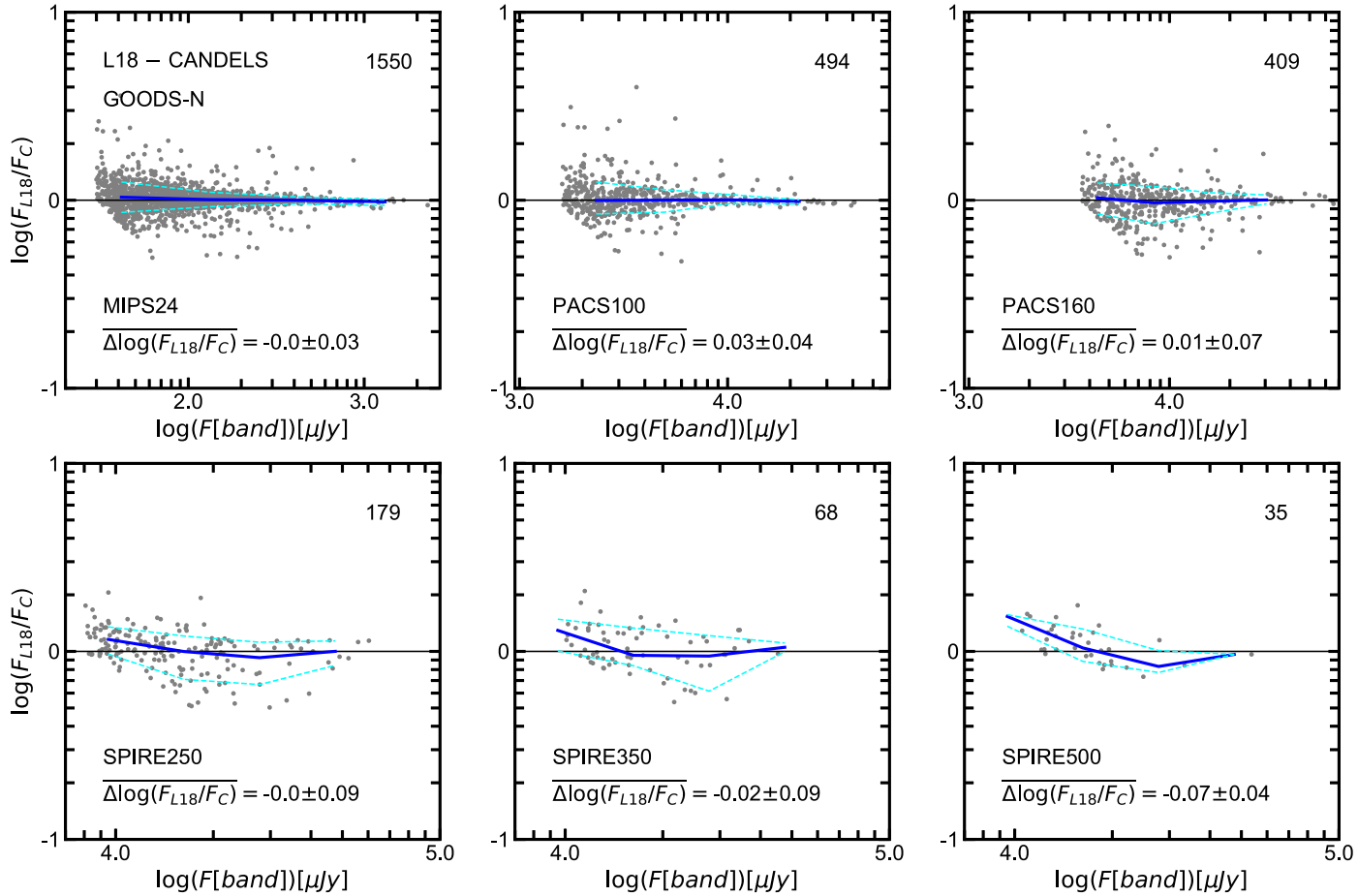

Figure 29. Comparison of mid-to-far-IR fluxes between the CANDELS (this work) and the Liu et al. (2018) catalogs in the GOODS-N field. From left to right and top to bottom, the panels show the comparison of the MIPS24, PACS100, PACS160, SPIRE250, SPIRE350, and SPIRE500 fluxes. The y axis shows the differences in L18 minus CANDELS values. The comparison is restricted to galaxies detected above S/N = 5 in each band in both catalogs (see Table 13). The blue lines show the running median and $\pm 1\sigma$ scatter of the distribution whose average values are indicated in the bottom-left corner. The values in each panel have been corrected by a constant offset derived from the average running median. The declining sensitivity and spatial resolution with increasing wavelength of the bands lead to fewer detections, larger scatter, and some outliers likely caused by differences in the deblending of particularly crowded sources. Nonetheless, we find an overall good agreement in all bands with systematic offsets smaller than ∼0.1 dex and a scatter that is roughly consistent with photometric uncertainties.

total (UV+IR) SFRs shows an excellent agreement with an average offset of $\Delta\mathrm{SFR} = -0.03$ dex and a slightly larger scatter of 0.21 dex. The increased scatter relative to the IR SFR comparison is likely caused by additional random differences in the UV SFRs, which are based on the different optical-to-NIR SED fitting of each work.

The L18 catalog aims to provide self-consistent far-IR to submillimeter photometry for galaxies in the GOODS-N region. As such, it is primarily selected in the far-IR, with the majority of the sources detected in a merged MIPS 24 + VLA 20 cm catalog. Most of these sources have NIR counterparts, primarily in the IRAC and K band, which are used to cross-match to other optical/NIR catalogs, such as the 3D-HST, for the purpose of obtaining optical-to-NIR photometry and photometric redshifts for each far-IR source. To first order, the L18 IR photometric measurements are similar to ours. They are both based on PSF fitting point-like sources using positional priors from other bands with higher spatial resolution. As Appendix D.1, these priors help reduce the confusion effects due to crowding. The primary difference between the L18 and CANDELS methods is the choice of the detection priors. For any given band, we chose priors from the previous, shorter wavelength band with better resolution (e.g., MIPS24 priors for PACS100), while L18 used the full SEDs at shorter wavelengths to predict the fluxes of all the possible counterparts and, based on those, chose only the priors that are likely to be detected.

This "informed" choice of priors can ease the confusion around particularly crowded sources or can help find sources with peculiar SEDs (e.g., those detected in SPIRE but not in PACS). Nonetheless, as discussed in Appendix D.1, the multiplicity in our sequential cross-matching method is very small (1:1 for MIPS and PACS and 3:1 or 2:1 for SPIRE) compared to that of a direct match from F160W or IRAC to SPIRE, where the multiplicity can be as high as 20 or 30. Thus, we expect the bulk of the detections and IR fluxes in both catalogs to be in good agreement. The L18 catalog contains ∼3300 sources over a slightly larger area of GOODS-N than that covered in the CANDELS survey. We cross-match both catalogs within a $0\farcs5$ radius, and we successfully identify all L18 sources that already had 3D-HST priors.

Figure 29 shows the photometric comparison between the six mid-to-far-IR bands in common between the two catalogs. Each panel shows only galaxies detected at S/N > 5 in both catalogs (see Table 13). As in Figure 28, the values have been corrected by a constant average offset determined from the

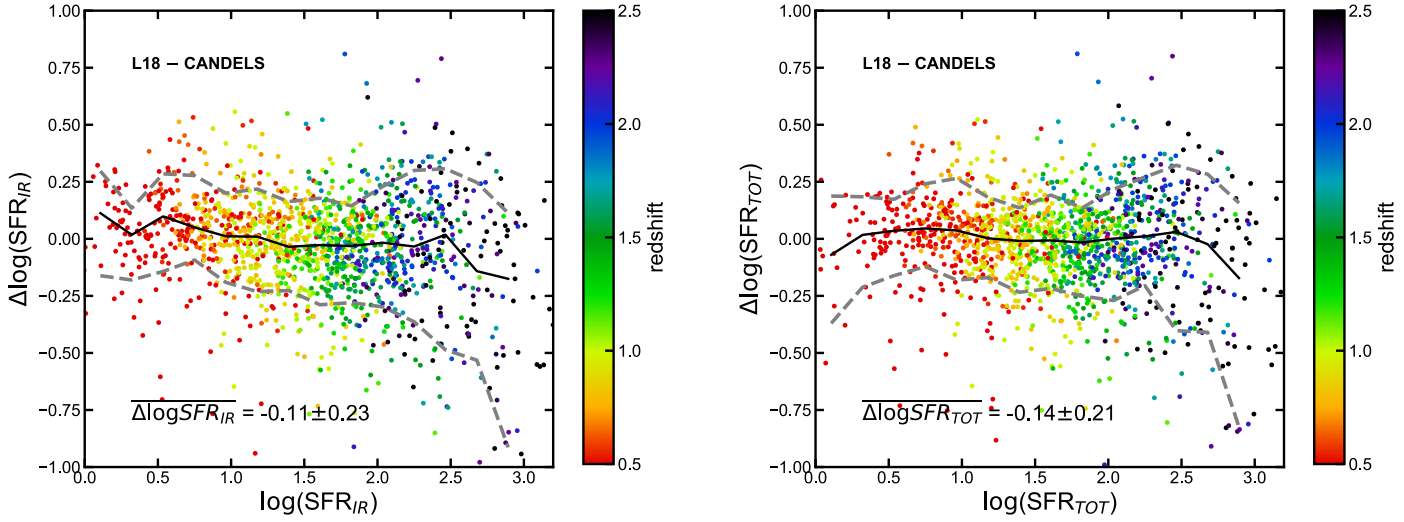

Figure 30. Comparison of the IR-based SFRs (left) and total UV+IR SFRs (right) in the CANDELS (this work) and the Liu et al. (2018) catalogs in the GOODS-N field, color-coded by redshift. The *y* axis shows the differences in the L18 minus CANDELS values. The comparison is restricted to galaxies detected above S/N = 5 in MIPS24 (the deepest band) in both catalogs. The black and gray lines show the running median and $\pm1\sigma$ scatter of the distribution whose average values are indicated in the bottom-left corner. The values in each panel have been corrected by a constant offset derived from the average running median. The CANDELS IR and total SFRs are only marginally larger than those in L18 by approximately constant values of 0.1 and 0.14 dex. There is no evidence for significant trends with SFR or redshift which sometimes appear due to strong features in the dust emission template used in the IR SED modeling. The scatter in the comparisons, $\lesssim$0.25 dex, is consistent with or even better than the typical 0.3 dex. Thus, we conclude that, overall, there is a good agreement between the CANDELS and L18 SFRs.

running median (blue line). Overall, the photometry in the two catalogs exhibits a good agreement with only small systematic offsets ($\lesssim$0.03 dex in all bands but SPIRE500) and a typical scatter roughly consistent with the expected photometric uncertainties. Owing to its higher sensitivity and spatial resolution, the comparisons in the MIPS and PACS bands span a broader dynamical range ($\sim$1–1.5 dex) and include more galaxies, which leads to a more homogeneous and smoother distribution. In SPIRE, however, both the dynamical range and the number of detections are smaller. Nonetheless, the bulk of the galaxies exhibit a good agreement with a scatter smaller than 0.1 dex.

In addition to the far-IR photometry, we also compare the IR-based SFRs derived from the fitting of the full IR SEDs. This comparison depends on additional factors such as the number of photometric fluxes in the IR SED or the set of dust emission templates used for the fitting. The IR SEDs in L18 include a few more bands in the submillimeter and radio. However, those detections are restricted to only a few IR-bright objects. Thus, the bulk of the sample has similar SEDs in both catalogs. As for the fitting templates, L18 uses the Magdis et al. (2012) library plus two additional AGN models, while we use a combination of three libraries (see Appendix D.2). Despite these differences, Figure 30 shows an excellent agreement in the SFRs with only a small average offset of −0.1 dex and a scatter of 0.21 dex, which is consistent with the typical uncertainties in these modeling-dependent comparisons. Furthermore, there is no evidence for any strong systematic offset with redshift. This is relevant because some dust emission templates exhibit strong spectral features, such as the PAH emission, that could bias the fit of some bands at specific redshifts. Lastly, the right panel of Figure 30 shows the comparison of the total (UV+IR) SFRs. We find again a good agreement with a similar average offset and scatter. This suggests that the impact of the UV SFRs on the total SFRs of these IR-bright galaxies is only minor and therefore small fluctuations in their values have a negligible impact in the comparison.

D.4. SFR Catalogs and Far-IR Photometric Flags

This section describes the content of the FIR photometry and SFR catalogs for all sources in the five CANDELS fields. Table 17 contains the FIR fluxes, dust attenuations, and different SFR tracers computed following the methods described in Section 5.4 and Appendix D.1. In addition, Table 18 provides FIR photometric and proximity flags that can be used to clean the catalog or to apply more restrictive conditions on the sources with FIR detections.

Note that, while in Table 17 there is only one possible F160W counterpart to each detection in an FIR band, the catalog described in Table 18 lists all the possible F160W counterparts to a given FIR source (MIPS, PACS, and SPIRE), indicating their likelihood (from 1 to *N*) of being the primary counterpart to the IR detection. Only the F160W sources with the maximum likelihood (e.g., MIPS_order = 1) have IR fluxes in Table 17. The total number of F160W counterparts to a given IR source as well as their distances to such source and their respective IRAC fluxes are also indicated.

In addition to the F160W multiplicity for a given FIR source, the catalog lists the multiplicity of that source in all other mid-to-far-IR bands up to itself. These multiplicities are computed for several cross-match radius relative to the typical spatial resolution of the FIR band (e.g., radius of 0.5, 1, 2, or 3 × the FWHM of the PSF). For the example, the MIPS flag catalog includes the multiplicities of F160W, IRAC, and MIPS sources within different radii. The PACS flag catalog includes multiplicities of F160W, IRAC, MIPS, and PACS sources, etc. The values in the flag catalogs provide a quick and simple way to find relative isolated FIR sources, or to identify FIR sources in crowded environments, which might lead to some contamination in the photometry.

Table 17
Description of the SFR Catalog

Column No.	Column Title	Description
1	id	Object identifier
2	z	Photometric redshift used in the IR SED fitting, corresponds to `zbest` in the redshift catalog
3 − 16	Flux, Flux_Err	Flux and flux error in each filter. Filters are included in order: MIPS 24 and 70 μm, PACS 100 and 160 μm and SPIRE 250, 350 and 500 μm [μJy]. Galaxies without IR detections have upper limits in MIPS24 with Flux = 20–70 [μJy] (see Table 13) and Flux_Err = 0. Upper limits in MIPS24 are used to estimate upper limits in SFR-IR, indicated with negative values.
17	SFR_{total}^{ladder}	Use as default SFR. Best estimate of the total SFR: either SFR_{IR}+SFR_{UV}^{obs} for IR detected sources or SFR_{UV}^{corr} for the rest.
18	SFR_ladder_type	Type of SFR indicators used in SFR_{total}^{ladder}: 1 for $SFR_{total}^{ladder} = SFR_{IR}^{fit} + SFR_{UV}^{obs}$ 2 for $SFR_{total}^{ladder} = SFR_{IR}^{W11} + SFR_{UV}^{obs}$ 3 for $SFR_{total}^{ladder} = SFR_{UV}^{corr}$
19	SFR_{UV}^{corr}	UV-based star formation rate corrected for extinction using the IRX-β_{UV} relations. This value is a weighted average of SFR_{UV}^{corr} (160) and SFR_{UV}^{corr}(280)
20	SFR_{UV}^{corr}_Err	Uncertainty in the UV-based star formation rate corrected for extinction.
21	SFR_{IR}	IR-based star formation rate. This value is equal to: $SFR_{IR} = SFR_{IR}^{fit}$ when SFR_ladder_type = 1. $SFR_{IR} = SFR_{IR}^{W11}$ when SFR_ladder_type = 2. $SFR_{IR} = -SFR_{IR}^{W11}$ when SFR_ladder_type = 3 (based on upper limits in MIPS24).
22	SFR_{UV}^{obs}(160)	UV-based star formation rate not corrected for extinction determined from the UV luminosity at 160 nm.
23	SFR_{UV}^{obs}(280)	UV-based star formation rate not corrected for extinction determined from the UV luminosity at 280 nm.
24	β_{UV}	UV slope
25	A_{UV}(160)	UV attenuation derived from the IRX-β_{UV} calibration for SFR_{UV}^{obs}(160)
26	A_{UV}(280)	UV attenuation derived from the IRX-β_{UV} calibration for SFR_{UV}^{obs}(280)
27	A(V)	Optical attenuation in the V-band derived from A_{UV} by assuming a Calzetti et al. (2000) attenuation law.
28	SFR_{IR}^{W11}	IR-based star formation rate derived from the MIPS 24 μm flux following Calzetti et al. (2000).
29	SFR_{UV}^{corr}(160)	UV-based star formation rate corrected for extinction using the IRX-β_{UV} relations determined from the UV luminosity at 160 nm.
30	SFR_{UV}^{corr}(280)	UV-based star formation rate corrected for extinction using the IRX-β_{UV} relations determined from the UV luminosity at 280 nm.

Table 18
Description of the SFR Flag Catalogs

Column No.	Column Title	Description
1	id	Object identifier in the F160W catalog
2	MIPS_ID_order	ID of the MIPS24 counterpart in the catalog from Pérez-González et al. (2008) Multiple F160W counterparts can be associated with this source; the order of likelihood is indicated by _1, _2, etc.
3	MIPS_discriminator	Criteria used to determine the likelihood order of the F160W counterparts to a MIPS source: mips24, irac3.6, irac8.0, dist There is only one counterpart within 2.″5 (mips24), or the primary counterpart is the brightest in this IRAC band or it is the closest in coordinates (dist)
4–9	Flux, Flux_Err	Flux and flux error in the MIPS24, IRAC80, and IRAC36 filters in units of μJy.
10	MIPS_distance	Distance between the F160W source and the closest MIPS source in arcseconds.
11	MIPS_order	Likelihood of the F160W source being the true counterpart of the MIPS source. From 1 to *N*, with 1 being the highest.
12	MIPS_n_counterparts	Number of F160W counterparts candidates for the closest MIPS source within 2.″5.
13	MIPS24_snr_cuts	Flag regarding the S/N cuts applied in MIPS24: 0—no flux, 1 flux > S/N limit, −1 flux < S/N limit. Only sources with flag > 0 are included in Table 17.
14–18	N_F160W_MIPS24_PSF	Number of F160W counterparts within 1, 0.5, 0.25, 2, and 3 times the size of the MIPS24 PSF (2.″0) around the MIPS24 primary.
19–23	N_F160W_MIPS24_WCS	Number of F160W counterparts within 1, 0.5, 0.25, 2, and 3 times the size of the WCS accuracy of the MIPS24 mosaic (2.″0) around the MIPS24 primary.
24–28	N_MIPS24_MIPS24_PSF	Number of MIPS24 counterparts within 1, 0.5, 0.25, 2, and 3 times the size of the MIPS24 PSF (2.″0) around the MIPS24 primary.
29–33	N_MIPS24_MIPS24_WCS	Number of MIPS24 counterparts within 1, 0.5, 0.25, 2, and 3 times the size of the WCS accuracy of the MIPS24 mosaic (2.″0) around the MIPS24 primary.
34–38	N_IRAC36_MIPS24_PSF	Number of IRAC36 counterparts within 1, 0.5, 0.25, 2, and 3 times the size of the MIPS24 PSF (2.″0) around the MIPS24 primary.

Table 18
(Continued)

Column No.	Column Title	Description
39–43	N_IRAC36_MIPS24_WCS	Number of IRAC36 counterparts within 1, 0.5, 0.25, 2, and 3 times the size of the WCS accuracy of the MIPS24 mosaic (2.″0) around the MIPS24 primary.
1	id	Object identifier in the F160W catalog
2	PACS_ID_order	ID of the PACS counterpart in the catalog from Pérez-González et al. (2008, 2010) Multiple F160W counterparts can be associated with this source; the order of likelihood is indicated by _1, _2, etc.
3	PACS_discriminator	Criteria used to determine the likelihood order of the F160W counterparts to a PACS source: pacs160, pacs100, mips24, irac3.6, irac8.0, dist There is only one counterpart within 3.″0 (pacs160/pac100), or the primary counterpart is the brightest in this MIPS/IRAC band or it is the closest in coordinates (dist)
4–13	Flux, Flux_Err	Flux and flux error in the PACS160, PACS100, MIPS24, IRAC80, IRAC36 filters. In units of μJy.
14	PACS_distance	Distance between the F160W source and the closest PACS source within 3.″0.
15	PACS_order	Likelihood of the F160W source being the true counterpart of the PACS source. From 1 to *N*, with 1 being the highest.
16	PACS_n_counterparts	Number of F160W counterparts candidates for the closest PACS source (IN WHICH RADIUS).
17	PACS100_snr_cuts	Flag regarding the S/N cuts applied in PACS100: 0—no flux, 1 flux > S/N limit, −1 flux < S/N limit. Only sources with flag > 0 are included in Table 17.
18	PACS160_snr_cuts	Flag regarding the S/N cuts applied in PACS160: 0—no flux, 1 flux > S/N limit, −1 flux < S/N limit. Only sources with flag > 0 are included in Table 17.
19–28	N_F160W_PACS_PSF	Number of F160W counterparts within 1, 0.5, 0.25, 2, and 3 times the size of the PACS100 and PACS160 PSF (4.″5/7.″0) around the PACS primary.
29–38	N_F160W_PACS_WCS	Number of F160W counterparts within 1, 0.5, 0.25, 2, and 3 times the size of the WCS accuracy of the PACS100 and PACS160 mosaics (2.″0/2.″5) around the PACS primary.
39–48	N_PACS_PACS_PSF	Number of PACS counterparts within 1, 0.5, 0.25, 2, and 3 times the size of the PACS100 and PACS160 PSF (4.″5/7.″0) around the PACS primary.
49–58	N_PACS_PACS_WCS	Number of PACS counterparts within 1, 0.5, 0.25, 2, and 3 times the size of the WCS accuracy of the PACS100 and PACS160 mosaics (2.″0/2.″5) around the PACS primary.
59–68	N_MIPS24_PACS_PSF	Number of MIPS24 counterparts within 1, 0.5, 0.25, 2, and 3 times the size of the PACS100 and PACS160 PSF (4.″5/7.″0) around the PACS primary.
69–78	N_MIPS24_PACS_WCS	Number of MIPS24 counterparts within 1, 0.5, 0.25, 2, and 3 times the size of the WCS accuracy of the PACS100 and PACS160 mosaics (2.″0/2.″5) around the PACS primary.
79–88	N_IRAC36_PACS_PSF	Number of IRAC36 counterparts within 1, 0.5, 0.25, 2, and 3 times the size of the PACS100 and PACS160 PSF (4.″5/7.″0) around the PACS primary.
89–98	N_IRAC36_PACS_WCS	Number of IRAC36 counterparts within 1, 0.5, 0.25, 2, and 3 times the size of the WCS accuracy of the PACS100 and PACS160 mosaics (2.″0/2.″5) around the PACS primary.
1	id	Object identifier in the F160W catalog
2	SPIRE_ID_order	ID of the SPIRE counterpart in the catalog from Pérez-González et al. (2008, 2010) Multiple F160W counterparts can be associated with this source the order of likelihood is indicated with _1, _2, etc.
3	SPIRE_discriminator	Criteria used to determine the likelihood order of the F160W counterparts to a SPIRE source: spire500, spire350, spire250, pacs160, pacs100, mips24, irac3.6, irac8.0, dist There is only one counterpart within 9.″0 (spire500, 350, 250), or the primary counterpart is the brightest in this PACS/MIPS/IRAC band, or it is the closest in coordinates (dist)
4–19	Flux, Flux_Err	Flux and flux error in the PACS160, PACS100, MIPS24, IRAC80, IRAC36 filters. In units of μJy.
20	SPIRE_distance	Distance between the F160W source and the closest SPIRE source in arcseconds.
21	SPIRE_order	Likelihood of the F160W source being the true counterpart of the SPIRE source. From 1 to *N*, with 1 being the highest.
22	SPIRE_n_counterparts	Number of F160W counterparts candidates for the closest SPIRE source within 9.″0.
23	SPIRE250_snr_cuts	Flag regarding the S/N cuts applied in SPIRE250: 0—no flux, 1 flux > S/N limit, −1 flux < S/N limit. Only sources with flag > 0 are included in Table 17.
24	SPIRE350_snr_cuts	Flag regarding the S/N cuts applied in SPIRE350: 0—no flux, 1 flux > S/N limit, −1 flux < S/N limit. Only sources with flag > 0 are included in Table 17.
25	SPIRE500_snr_cuts	Flag regarding the S/N cuts applied in SPIRE500: 0—no flux, 1 flux > S/N limit, −1 flux < S/N limit. Only sources with flag > 0 are included in Table 17.
26–30	N_F160W_SPIRE_PSF	Number of F160W counterparts within 1, 0.5, 0.25, 2, and 3 times the size of the SPIRE250, SPIRE 350, and SPIRE500 PSF (11.″0/11.″0/17.″0) around the SPIRE primary.
41–55	N_F160W_SPIRE_WCS	Number of F160W counterparts within 1, 0.5, 0.25, 2, and 3 times the size of the WCS accuracy of the SPIRE250, SPIRE 350, and SPIRE500 mosaics (9.″0/9.″0/15.″0) around the SPIRE primary.
56–70	N_SPIRE_SPIRE_PSF	Number of SPIRE counterparts within 1, 0.5, 0.25, 2, and 3 times the size of the SPIRE250, SPIRE 350, and SPIRE500 PSF (11.″0/11.″0/17.″0) around the SPIRE primary.
71–85	N_SPIRE_SPIRE_WCS	Number of SPIRE counterparts within 1, 0.5, 0.25, 2, and 3 times the size of the WCS accuracy of the SPIRE250, SPIRE 350, and SPIRE500 mosaics (9.″0/9.″0/15.″0) around the SPIRE primary.
86–100	N_PACS_SPIRE_PSF	Number of PACS counterparts within 1, 0.5, 0.25, 2, and 3 times the size of the SPIRE250, SPIRE 350, and SPIRE500 PSF (11.″0/11.″0/17.″0) around the SPIRE primary.

Table 18
(Continued)

Column No.	Column Title	Description
101–115	N_PACS_SPIRE_WCS	Number of PACS counterparts within 1, 0.5, 0.25, 2, and 3 times the size of the WCS accuracy of the SPIRE250, SPIRE 350, and SPIRE500 mosaics (9.″0/9.″0/15.″0) around the SPIRE primary.
116–130	N_MIPS_SPIRE_PSF	Number of MIPS counterparts within 1, 0.5, 0.25, 2, and 3 times the size of the SPIRE250, SPIRE 350, and SPIRE500 PSF (11.″0/11.″0/17.″0) around the SPIRE primary.
131–145	N_MIPS_SPIRE_WCS	Number of MIPS counterparts within 1, 0.5, 0.25, 2, and 3 times the size of the WCS accuracy of the SPIRE250, SPIRE 350, and SPIRE500 mosaics (9.″0/9.″0/15.″0) around the SPIRE primary.
146–160	N_IRAC36_SPIRE_PSF	Number of IRAC36 counterparts within 1, 0.5, 0.25, 2, and 3 times the size of the SPIRE250, SPIRE 350, and SPIRE500 PSF (11.″0/11.″0/17.″0) around the SPIRE primary.
161–175	N_IRAC36_SPIRE_WCS	Number of IRAC36 counterparts within 1, 0.5, 0.25, 2, and 3 times the size of the WCS accuracy of the SPIRE250, SPIRE 350, and SPIRE500 mosaics (9.″0/9.″0/15.″0) around the SPIRE primary.

ORCID iDs

Guillermo Barro https://orcid.org/0000-0001-6813-875X
Antonio Cava https://orcid.org/0000-0002-4821-1275
Gabriel Brammer https://orcid.org/0000-0003-2680-005X
Viraj Pandya https://orcid.org/0000-0002-2499-9205
Jonathan R. Trump https://orcid.org/0000-0002-1410-0470
Matthew L. N. Ashby https://orcid.org/0000-0002-3993-0745
Nicolas Cardiel https://orcid.org/0000-0002-9334-2979
Marco Castellano https://orcid.org/0000-0001-9875-8263
Christopher J. Conselice https://orcid.org/0000-0003-1949-7638
Timothy Dolch https://orcid.org/0000-0001-8885-6388
Jennifer L. Donley https://orcid.org/0000-0002-6589-2017
Giovanni G. Fazio https://orcid.org/0000-0002-0670-0708
Henry Ferguson https://orcid.org/0000-0001-7113-2738
Steve Finkelstein https://orcid.org/0000-0001-8519-1130
Adriano Fontana https://orcid.org/0000-0003-3820-2823
Eric Gawiser https://orcid.org/0000-0003-1530-8713
Mauro Giavalisco https://orcid.org/0000-0002-7831-8751
Andrea Grazian https://orcid.org/0000-0002-5688-0663
Norman A. Grogin https://orcid.org/0000-0001-9440-8872
Nimish P. Hathi https://orcid.org/0000-0001-6145-5090
Shoubaneh Hemmati https://orcid.org/0000-0003-2226-5395
David C. Koo https://orcid.org/0000-0003-3385-6799
Kyoung-Soo Lee https://orcid.org/0000-0003-3004-9596
Lihwai Lin https://orcid.org/0000-0001-7218-7407
Ray A. Lucas https://orcid.org/0000-0003-1581-7825
Kirpal Nandra https://orcid.org/0000-0002-7150-9192
Hooshang Nayyeri https://orcid.org/0000-0001-8242-9983
Jeffrey A. Newman https://orcid.org/0000-0001-8684-2222
Marc Rafelski https://orcid.org/0000-0002-9946-4731
Lucia Rodríguez-Munoz https://orcid.org/0000-0002-0192-5131
Mara Salvato https://orcid.org/0000-0001-7116-9303
Mauro Stefanon https://orcid.org/0000-0001-7768-5309
Steven P. Willner https://orcid.org/0000-0002-9895-5758
Tommy Wiklind https://orcid.org/0000-0001-8054-8049
Stijn Wuyts https://orcid.org/0000-0003-3735-1931

References

Acquaviva, V., Gawiser, E., & Guaita, L. 2011, ApJ, 737, 47
Alexander, D. M., Bauer, F. E., Brandt, W. N., et al. 2003, AJ, 126, 539
Arnouts, S., & Ilbert, O. 2011, LePHARE: Photometric Analysis for Redshift Estimate, Astrophysics Source Code Library, ascl:1108.009
Ashby, M. L. N., Willner, S. P., Fazio, G. G., et al. 2013, ApJ, 769, 80
Ashby, M. L. N., Willner, S. P., Fazio, G. G., et al. 2015, ApJS, 218, 33
Atek, H., Malkan, M., McCarthy, P., et al. 2010, ApJ, 723, 104
Barden, M., Häußler, B., Peng, C. Y., et al. 2012, MNRAS, 422, 449
Barger, A. J., Cowie, L. L., & Wang, W.-H. 2008, ApJ, 689, 687
Barro, G., Faber, S. M., Pérez-González, P. G., et al. 2014, ApJ, 791, 52
Barro, G., Pérez-González, P. G., Gallego, J., et al. 2011, ApJS, 193, 30
Bell, E. F., McIntosh, D. H., Katz, N., et al. 2003, ApJS, 149, 289
Bell, E. F., Papovich, C., Wolf, C., et al. 2005, ApJ, 625, 23
Bell, E. F., van der Wel, A., Papovich, C., et al. 2012, ApJ, 753, 167
Berta, S., Magnelli, B., Nordon, R., et al. 2011, A&A, 532, A49
Bertin, E. 2010, SWarp: Resampling and Co-adding FITS Images Together, Astrophysics Source Code Library, ascl:1010.068
Bertin, E., & Arnouts, S. 1996, A&AS, 117, 393
Bezanson, R., Wake, D. A., Brammer, G. B., et al. 2016, ApJ, 822, 30
Bolzonella, M., Miralles, J.-M., & Pelló, R. 2000, A&A, 363, 476
Bouwens, R. J., Oesch, P. A., Labbé, I., et al. 2016, ApJ, 830, 67
Brammer, G., Kelly, P., Rodney, S., et al. 2014, ATel, 5728
Brammer, G., Ryan, R., & Pirzkal, N. 2015, Source-dependent Master Sky Images for the WFC3/IR Grisms, Instrument Science Rep. WFC3 2015-17 (Baltimore, MD: STSci)
Brammer, G. B., van Dokkum, P. G., & Coppi, P. 2008, ApJ, 686, 1503
Brammer, G. B., van Dokkum, P. G., Franx, M., et al. 2012, ApJS, 200, 13
Brammer, G. B., Whitaker, K. E., van Dokkum, P. G., et al. 2011, ApJ, 739, 24
Bruzual, G., & Charlot, S. 2003, MNRAS, 344, 1000
Buat, V., Iglesias-Páramo, J., Seibert, M., et al. 2005, ApJL, 619, L51
Buat, V., Noll, S., Burgarella, D., et al. 2012, A&A, 545, A141
Buat, V., Takeuchi, T. T., Iglesias-Páramo, J., et al. 2007, ApJS, 173, 404
Calzetti, D., Armus, L., Bohlin, R. C., et al. 2000, ApJ, 533, 682
Capak, P., Cowie, L. L., Hu, E. M., et al. 2004, AJ, 127, 180
Casey, C. M., Scoville, N. Z., Sanders, D. B., et al. 2014, ApJ, 796, 95
Cava, A., Pérez-González, P. G., Eliche-Moral, M. C., et al. 2015, ApJ, 812, 155
Chabrier, G. 2003, PASP, 115, 763
Chapman, S. C., Blain, A. W., Smail, I., et al. 2005, ApJ, 622, 772
Charlot, S., & Fall, S. M. 2000, ApJ, 539, 718
Chary, R., & Elbaz, D. 2001, ApJ, 556, 562
Cooper, M. C., Aird, J. A., Coil, A. L., et al. 2011, ApJS, 193, 14
Cowie, L. L., Barger, A. J., Hu, E. M., et al. 2004, AJ, 127, 3137
Daddi, E., Cimatti, A., Renzini, A., et al. 2004, ApJ, 617, 746
Daddi, E., Dickinson, M., Morrison, G., et al. 2007, ApJ, 670, 156
Daddi, E., Renzini, A., Pirzkal, N., et al. 2005, ApJ, 626, 680
Dahlen, T., Mobasher, B., Faber, S. M., et al. 2013, ApJ, 775, 93
Dale, D. A., Cohen, S. A., Johnson, L. C., et al. 2009, ApJ, 703, 517
Dale, D. A., & Helou, G. 2002, ApJ, 576, 159
Dickinson, M., Bergeron, J., & Casertano, S. 2003, Great Observatories Origins Deep Survey (GOODS) Validation Observations, Spitzer Proposal ID 196 (Pasadena, CA: CalTech)
Draine, B. T., & Li, A. 2007, ApJ, 657, 810
Duncan, K., Conselice, C. J., Mortlock, A., et al. 2014, MNRAS, 444, 2960
Elbaz, D., Dickinson, M., Hwang, H. S., et al. 2011, A&A, 533, A119
Erb, D. K., Pettini, M., Shapley, A. E., et al. 2010, ApJ, 719, 1168

Faber, S. 2011, The Cosmic Assembly Near-IR Deep Extragalactic Legacy Survey ("CANDELS"), MAST, doi:10.17909/T94S3X
Fazio, G. G., Ashby, M. L. N., Barmby, P., et al. 2004, ApJS, 154, 39
Ferreras, I., Pasquali, A., Malhotra, S., et al. 2009, ApJ, 706, 158
Finkelstein, S. L., Ryan, R. E., Jr., Papovich, C., et al. 2015, ApJ, 810, 71
Fontana, A., D'Odorico, S., Poli, F., et al. 2000, AJ, 120, 2206
Foreman-Mackey, D., Hogg, D. W., Lang, D., et al. 2013, PASP, 125, 306
Franx, M., van Dokkum, P. G., Schreiber, N. M. F., et al. 2008, ApJ, 688, 770
Frayer, D. T., Huynh, M. T., Chary, R., et al. 2006, ApJL, 647, L9
Galametz, A., Grazian, A., Fontana, A., et al. 2013, ApJS, 206, 10
Giallongo, E., Ragazzoni, R., Grazian, A., et al. 2008, A&A, 482, 349
Giavalisco, M., Ferguson, H. C., Koekemoer, A. M., et al. 2004, ApJL, 600, L93
Gonzaga, S. 2012, The DrizzlePac Handbook (Baltimore, MD: STSci)
Grazian, A., Fontana, A., Santini, P., et al. 2015, A&A, 575, A96
Grazian, A., Giallongo, E., Paris, D., et al. 2017, A&A, 602, A18
Griffin, M. J., Abergel, A., Abreu, A., et al. 2010, A&A, 518, L3
Grogin, N. A., Kocevski, D. D., Faber, S. M., et al. 2011, ApJS, 197, 35
Gunn, J. E., & Stryker, L. L. 1983, ApJS, 52, 121
Guo, Y., Ferguson, H. C., Bell, E. F., et al. 2015, ApJ, 800, 39
Guo, Y., Ferguson, H. C., Giavalisco, M., et al. 2013, ApJS, 207, 24
Heckman, T. M., Robert, C., Leitherer, C., et al. 1998, ApJ, 503, 646
Hsu, L.-T., Lin, L., Dickinson, M., et al. 2019, ApJ, 871, 233
Huertas-Company, M., Gravet, R., Cabrera-Vives, G., et al. 2015, ApJS, 221, 8
Ilbert, O., Capak, P., Salvato, M., et al. 2009, ApJ, 690, 1236
Ilbert, O., Salvato, M., Le Floc'h, E., et al. 2010, ApJ, 709, 644
Kajisawa, M., Ichikawa, T., Tanaka, I., et al. 2009, ApJ, 702, 1393
Kajisawa, M., Ichikawa, T., Tanaka, I., et al. 2011, PASJ, 63, 379
Kartaltepe, J. S., Sanders, D. B., Le Floc'h, E., et al. 2010, ApJ, 709, 572
Kennicutt, R. C., Jr. 1998, ARA&A, 36, 189
Koekemoer, A. M., Faber, S. M., Ferguson, H. C., et al. 2011, ApJS, 197, 36
Kong, X., Charlot, S., Brinchmann, J., et al. 2004, MNRAS, 349, 769
Kriek, M., Shapley, A. E., Reddy, N. A., et al. 2015, ApJS, 218, 15
Kriek, M., van Dokkum, P. G., Franx, M., et al. 2009, ApJL, 705, L71
Krist, J. 1995, in ASP Conf. Ser. 77, Astronomical Data Analysis Software and Systems IV, ed. R. A. Shaw, H. E. Payne, & J. J. E. Hayes (San Francisco, CA: ASP), 349
Kron, R. G. 1980, ApJS, 43, 305
Labbé, I., Bouwens, R., Illingworth, G. D., et al. 2006, ApJL, 649, L67
Labbé, I., Huang, J., Franx, M., et al. 2005, ApJL, 624, L81
Labbé, I., Oesch, P. A., Bouwens, R. J., et al. 2013, ApJL, 777, L19
Laidler, V. G., Papovich, C., Grogin, N. A., et al. 2007, PASP, 119, 1325
Lee, K.-S., Ferguson, H. C., Wiklind, T., et al. 2012, ApJ, 752, 66
Leitherer, C., Ekström, S., Meynet, G., et al. 2014, ApJS, 212, 14
Liu, D., Daddi, E., Dickinson, M., et al. 2018, ApJ, 853, 172
Lutz, D., Poglitsch, A., Altieri, B., et al. 2011, A&A, 532, A90
Magdis, G. E., Daddi, E., Béthermin, M., et al. 2012, ApJ, 760, 6
Magnelli, B., Elbaz, D., Chary, R. R., et al. 2009, A&A, 496, 57
Magnelli, B., Popesso, P., Berta, S., et al. 2013, A&A, 553, A132
Marchesini, D., van Dokkum, P. G., Förster Schreiber, N. M., et al. 2009, ApJ, 701, 1765
McLure, R. J., Dunlop, J. S., Cullen, F., et al. 2018, MNRAS, 476, 3991
Merlin, E., Bourne, N., Castellano, M., et al. 2016, A&A, 595, A97
Merlin, E., Fontana, A., Ferguson, H. C., et al. 2015, A&A, 582, A15
Meurer, G. R., Heckman, T. M., & Calzetti, D. 1999, ApJ, 521, 64
Meurer, G. R., Heckman, T. M., Lehnert, M. D., et al. 1997, AJ, 114, 54
Mobasher, B., Dahlen, T., Ferguson, H. C., et al. 2015, ApJ, 808, 101
Momcheva, I. G., Brammer, G. B., van Dokkum, P. G., et al. 2016, ApJS, 225, 27
Mortlock, A., Conselice, C. J., Hartley, W. G., et al. 2015, MNRAS, 447, 2
Muzzin, A., Marchesini, D., Stefanon, M., et al. 2013, ApJ, 777, 18
Narayanan, D., Conroy, C., Davé, R., et al. 2018, ApJ, 869, 70
Nayyeri, H., Hemmati, S., Mobasher, B., et al. 2017, ApJS, 228, 7
Noeske, K. G., Weiner, B. J., Faber, S. M., et al. 2007, ApJL, 660, L43
Nordon, R., Lutz, D., Saintonge, A., et al. 2013, ApJ, 762, 125
Oke, J. B. 1974, ApJS, 27, 21
Oliver, S. J., Bock, J., Altieri, B., et al. 2012, MNRAS, 424, 1614
Overzier, R. A., Heckman, T. M., Schiminovich, D., et al. 2010, ApJ, 710, 979
Overzier, R. A., Heckman, T. M., Wang, J., et al. 2011, ApJL, 726, L7
Papovich, C., Dickinson, M., & Ferguson, H. C. 2001, ApJ, 559, 620
Papovich, C., Labbé, I., Quadri, R., et al. 2015, ApJ, 803, 26
Papovich, C., Moustakas, L. A., Dickinson, M., et al. 2006, ApJ, 640, 92
Papovich, C., Rudnick, G., Le Floc'h, E., et al. 2007, ApJ, 668, 45
Pérez-González, P. G., Cava, A., Barro, G., et al. 2013, ApJ, 762, 46
Pérez-González, P. G., Egami, E., Rex, M., et al. 2010, A&A, 518, L15
Pérez-González, P. G., Rieke, G. H., Egami, E., et al. 2005, ApJ, 630, 82
Pérez-González, P. G., Rieke, G. H., Villar, V., et al. 2008, ApJ, 675, 234
Pettini, M., Kellogg, M., Steidel, C. C., et al. 1998, ApJ, 508, 539
Poglitsch, A., Waelkens, C., Geis, N., et al. 2010, A&A, 518, L2
Pope, A., Bussmann, R. S., Dey, A., et al. 2008, ApJ, 689, 127
Popping, G., Decarli, R., Man, A. W. S., et al. 2017, A&A, 602, 11
Rawle, T. D., Altieri, B., Egami, E., et al. 2016, MNRAS, 459, 1626
Reddy, N. A., Erb, D. K., Pettini, M., et al. 2010, ApJ, 712, 1070
Reddy, N. A., Shapley, A. E., Sanders, R. L., et al. 2018, ApJ, 869, 92
Reddy, N. A., Steidel, C. C., Erb, D. K., et al. 2006, ApJ, 653, 1004
Reddy, N. A., Steidel, C. C., Pettini, M., et al. 2008, ApJS, 175, 48
Rieke, G. H., Alonso-Herrero, A., Weiner, B. J., et al. 2009, ApJ, 692, 556
Riess, A. G., Strolger, L.-G., Casertano, S., et al. 2007, ApJ, 659, 98
Rodríguez-Muñoz, L., Rodighiero, G., Mancini, C., et al. 2019, MNRAS, 485, 586
Rothberg, B., Kuhn, O., Edwards, M. L., et al. 2016, Proc. SPIE, 9906, 990622
Rujopakarn, W., Rieke, G. H., Weiner, B. J., et al. 2013, ApJ, 767, 73
Salmon, B., Papovich, C., Finkelstein, S. L., et al. 2015, ApJ, 799, 183
Salpeter, E. E. 1955, ApJ, 121, 161
Santini, P., Ferguson, H. C., Fontana, A., et al. 2015, ApJ, 801, 97
Schreiber, C., Pannella, M., Elbaz, D., et al. 2015a, A&A, 575, A74
Schreiber, C., Pannella, M., Elbaz, D., et al. 2015b, A&A, 575, A74
Scoville, N., Sheth, K., Aussel, H., et al. 2016, ApJ, 820, 83
Skelton, R. E., Whitaker, K. E., Momcheva, I. G., et al. 2014, ApJS, 214, 24
Skrutskie, M. F., Cutri, R. M., Stiening, R., et al. 2006, AJ, 131, 1163
Speagle, J. S., Steinhardt, C. L., Capak, P. L., et al. 2014, ApJS, 214, 15
Stefanon, M., Yan, H., Mobasher, B., et al. 2017, ApJS, 229, 32
Straatman, C. M. S., Labbé, I., Spitler, L. R., et al. 2014, ApJL, 783, L14
Straatman, C. M. S., Spitler, L. R., Quadri, R. F., et al. 2016, ApJ, 830, 51
Symeonidis, M., Willner, S. P., Rigopoulou, D., et al. 2008, MNRAS, 385, 1015
Tal, T., Dekel, A., Oesch, P., et al. 2014, ApJ, 789, 164
Treu, T., Schmidt, K. B., Brammer, G. B., et al. 2015, ApJ, 812, 114
Trump, J. R., Konidaris, N. P., Barro, G., et al. 2013, ApJL, 763, L6
van der Wel, A., Bell, E. F., Häussler, B., et al. 2012, ApJS, 203, 24
van der Wel, A., Franx, M., van Dokkum, P. G., et al. 2014, ApJ, 788, 28
Wang, T., Elbaz, D., Schreiber, C., et al. 2016, ApJ, 816, 84
Whitaker, K. E., Franx, M., Leja, J., et al. 2014, ApJ, 795, 104
Whitaker, K. E., Kriek, M., van Dokkum, P. G., et al. 2012, ApJ, 745, 179
Whitaker, K. E., Labbé, I., van Dokkum, P. G., et al. 2011, ApJ, 735, 86
Wiklind, T., Dickinson, M., Ferguson, H. C., et al. 2008, ApJ, 676, 781
Williams, R. E., Blacker, B., Dickinson, M., et al. 1996, AJ, 112, 1335
Williams, R. J., Quadri, R. F., Franx, M., et al. 2009, ApJ, 691, 1879
Wirth, G. D., Trump, J. R., Barro, G., et al. 2015, AJ, 150, 153
Wirth, G. D., Willmer, C. N. A., Amico, P., et al. 2004, AJ, 127, 3121
Witt, A. N., & Gordon, K. D. 2000, ApJ, 528, 799
Wolf, C., Dye, S., Kleinheinrich, M., et al. 2001, A&A, 377, 442
Wolf, C., Meisenheimer, K., Rix, H.-W., et al. 2003, A&A, 401, 73
Wuyts, S., Förster Schreiber, N. M., Genzel, R., et al. 2012, ApJ, 753, 114
Wuyts, S., Förster Schreiber, N. M., Lutz, D., et al. 2011a, ApJ, 738, 106
Wuyts, S., Förster Schreiber, N. M., Nelson, E. J., et al. 2013, ApJ, 779, 135
Wuyts, S., Förster Schreiber, N. M., van der Wel, A., et al. 2011b, ApJ, 742, 96
Wuyts, S., Labbé, I., Schreiber, N. M. F., et al. 2008, ApJ, 682, 985